Numerical Investigation of Heat Transfer Enhancement in Solar Receiver Tubes

by

Ziyauddin Panchbhaya

Thesis presented in partial fulfilment of the requirements for the degree of Master of Engineering (Mechanical) in the Faculty of Engineering at Stellenbosch University

Supervisor: Dr. J.E. Hoffmann

March 2020

Declaration

By submitting this thesis electronically, I declare that the entirety of the work contained therein is my own, original work, that I am the sole author thereof (save to the extent explicitly otherwise stated), that reproduction and publication thereof by Stellenbosch University will not infringe any third party rights and that I have not previously in its entirety or in part submitted it for obtaining any qualification.

Date: March 2020 .....

Abstract

Numerical Investigation of Heat Transfer Enhancement in Solar Receiver Tubes

Z. Panchbhaya

Department of Mechanical and Mechatronic Engineering,
University of Stellenbosch,
Private Bag X1, Matieland 7602, South Africa.

Thesis: MEng (Mech)

March 2020

Concentrated solar power (CSP) could serve as a viable means of meeting the demands of an increasing rise in electricity requirements, as well as, being a means to produce clean and renewable energy. In many CSP plants, steam, molten salts, and thermal oils have been used as the primary heat transfer fluids. Although air has gained traction in recent years as a contender for the heat transfer fluid in solar Brayton cycles, it has not been a viable option due to its poor heat transfer characteristics.

This research focused primarily on finding a passive means of enhancing heat transfer inside solar receiver tubes, while minimizing pressure drop. The performance of the heat transfer enhancement was evaluated by performing numerical simulations to determine thermohydraulic behaviour. An appropriate turbulence model was selected and compared to existing literature. The use of multiple twisted tapes was initially investigated followed by the use of helically twisted tapes. A novel enhancer called the *half-pitch helically twisted tape* is proposed to be used in solar receiver tubes. Optimization was performed on the half-pitch helically twisted tape and a full simulation was then conducted at elevated temperatures and pressures with an applied non uniform one sided heat flux. The results showed that the half-pitch helically twisted tape performs satisfactorily with an acceptable pressure loss, obtaining a thermal enhancement factor of approximately $\eta \simeq 0.95$.

Uittreksel

Numeriese Ondersoek van Warmte Oordrag Verbetering in Son Ontvanger Buise

("Numerical Investigation of Heat Transfer Enhancement in Solar Receiver Tubes")

Z. Panchbhaya

Departement Meganiese en Megatroniese Ingenieurswese,
Universiteit van Stellenbosch,
Privaatsak X1, Matieland 7602, Suid Afrika.

Tesis: MIng (Meg)

Maart 2020

Gekonsentreerde sonkrag (CSP) kan gebruik word om aan die vereistes van toenemende elektrisiteitsbehoeftes te voldoen, en is ook 'n manier om skoon en hernubare energie te produseer. In baie CSP aanlegte word stoom, gesmelte soute, of termiese olies as die primêre hitte-oordragvloeistowwe gebruik. Howel lug in die afgelope paar jaar as 'n aanspraakmaker vir hitte-oordragvloeistof in sonkrag-Brayton-siklusse traksie opgedoen het, is dit as gevolg van die swak hitte-oordragseienskappe, nie 'n lewensvatbare opsie nie.

Hierdie navorsing fokus hoofsaaklik daar op om 'n passiewe manier te vind om hitte oordrag binne sonkragontvangerbuise te verhoog, terwyl die drukval tot 'n minimum beperk word. Die werkverrigting van die hitte-oordragverbetering is geëvalueer deur numeriese simulasies uit te voer om termohidrouliese gedrag te bepaal. 'n Gepasteturbulensie-model was gekies en vergelyk met die bestaande literatuur. Die gebruik van veelvuldige gedraaide linte was aanvanklik ondersoek, en gevolg deur die gebruik van spiraalvormige gedraaide linte. Daar word voorgestel dat 'n nuwe versterker genaamd die half-draai heliese draailint in die sonbuise gebruik word. Optimering van die half-draaide heliese lint was uitgevoer en 'n volledige simulasie met 'n toepaslike nie-eenvormige hittevloed was daarna gedoen met verhoogde temperature en druk. Die resultate het aangetoon dat die half-draai heliese lint bevredigend presteer met 'n aanvaarbare drukverlies, verkry 'n termiese verbeteringsfaktor van ongeveer $\eta \simeq 0.95$.

Acknowledgements

I would like to express my sincere gratitude to the following people and organisations, without whom this would not be possible :

- First and foremost, my heartfelt and sincere thanks goes to my supervisor Dr Hoffmann for providing me with this incredible opportunity. The unwavering support, help and suggestions were invaluable. His door was always open, and help was always provided. It was an honour to work alongside him, and I will always be grateful for everything he has done for me.
- To the students and staff of STERG who helped me along the way. Your help does not go unnoticed. Thank you for everything.
- To STERG for the providing me with the project funding over the period of my masters degree.
- To Dr Hoffmann, STERG and CRSES for the funding to attend the SolarPACES 2019 conference in Daegu, South Korea. Thank you for this incredible opportunity.
- To the Centre for High Performance Computing (CHPC) facility for the use of the Lengau cluster when running multiple processors.
- And finally a great deal of thanks to my parents, specifically to my mother Sara, who has always supported me.

Dedications

This thesis is dedicated to every engineer, mathematician and scientist, that has helped pave the way in helping create a better world that is more comfortable and enjoyable.
"If I have seen further it is by standing on the shoulders of giants" - Sir Isaac Newton

Contents

List of Figures

List of Tables

Nomenclature

Constants

$M_w = \quad 28.97\,\mathrm{g/mol}$

$R_u = \quad 8.314\,\mathrm{J/mol \cdot K}$

Variables - Roman

A	Area	$[\mathrm{m}^2]$
C_p	Specific heat at constant pressure	$[\mathrm{J/kg{\cdot}K}]$
c	Quadratic function	$[-]$
D	Diameter	$[\mathrm{m}, \mathrm{mm}]$
e	Mesh error	$[-]$
F	Blending function	$[-]$
F_s	Safety factor	$[-]$
f	Friction factor	$[-]$
H	Helical height	$[\mathrm{m}]$
h	Enthalpy	$[\mathrm{J/kg}]$
h	Heat transfer coefficient	$[\mathrm{W/m^2{\cdot}K}]$
k	Thermal conductivity	$[\mathrm{W/m{\cdot}K}]$
k	Turbulent kinetic energy	$[\mathrm{m^2/s^2}]$
L	Length	$[\mathrm{m}]$
m	Number of design variables	$[-]$
N	Grid size	$[-]$
Nu	Nusselt number	$[-]$
$\mathcal{O}$	Order (of)	$[-]$
P	Helical pitch	$[\mathrm{m}]$
p	Order of convergence	$[-]$
p	Pressure field	$[\mathrm{Pa}]$
$\dot{Q}$	Heat transfer rate	$[\mathrm{W}]$
q	Heat flux	$[\mathrm{W/m^2}]$
r	Refinement ratio	$[-]$

R^2	Coefficient of determination	[−]
Re	Reynolds number	[−]
T	Temperature	[K, °C]
t	Tape clearance	[m, mm]
T^+	Dimensionless temperature	[−]
u	Velocity	[m/s]
u^+	Dimensionless velocity	[−]
V	Velocity	[m/s]
$\dot{V}$	Volumetric flow rate	[m^3/s]
W	Tape pitch	[m, mm]
y	Tape height	[m, mm]
y^+	Dimensionless distance	[−]
Z	Compressibility factor	[−]

Variables - Greek

ΔP	Pressure drop	[Pa]
δ	Hydrodynamic boundary layer thickness	[m]
δ	Tape thickness	[m, mm]
δ_{ij}	Kronecker delta	[−]
δ_T	Thermal boundary layer thickness	[m]
ϵ	Convergence criteria	[−]
ϵ	Rate of dissipation of turbulent kinetic energy	[m^2/s^3]
η	Compressor efficiency	[−]
η	Thermal enhancement factor	[−]
μ	Dynamic viscosity	[kg/m·s]
ν	Kinematic viscosity	[m^2/s]
ρ	Density	[kg/m^3]
σ	Prandtl number	[−]
Φ	Mean property	[−]
ϕ	Flow property	[−]
ϕ	Mesh solution	[−]
ω	Specific rate of dissipation	[s^{-1}]

Vectors and Tensors

$\boldsymbol{\nabla}$	Del operator
$\mathbf{x}$	Design vector
Θ	Dissipation function

$\boldsymbol{\rho}$	Penalty parameter vector
$\boldsymbol{\beta}$	Penalty parameter vector
$\boldsymbol{V}$	Velocity vector
$\boldsymbol{\tau}$	Viscous stress tensor

Subscripts

b	Bulk
comp	Compressor
x	Coordinate (in the x direction)
y	Coordinate (in the y direction)
e	Enhanced design
f	Fluid
i, j	Index notation
0	Initial
p	Plain tube
T	Thermal
t	Turbulent
w	Wall

Abbreviations

CFD	Computational Fluid Dynamics
CSP	Concentrated Solar Power
DNS	Direct Numerical Simulation
FEA	Finite Element Analysis
FVM	Finite Volume Method
FMG	Full Multigrid
GCI	Grid Convergence Index
HPHTT	Half-pitch Helically Twisted Tape
HTF	Heat Transfer Fluid
HTT	Helically Twisted Tape
LES	Large Eddy Simulation
MTT	Multiple Twisted Tapes
PV	Photovoltaic
PCD	Pitch Circle Diameter
PML	Profiled Multilayer Tubes
PP	Pumping power
RNG	Renormalized Group
RANS	Reynolds Average Navier Stokes
RSM	Reynolds Stress Model
SST	Shear Stress Transport

SOLHYCO	Solar-hybrid Power and Cogeneration
SA	Spalart-Allmaras
SQSD	Spherical Quadratic Steepest Descent
TEF	Thermal Enhancement Factor
UDF	User Defined Function
w.r.t	With regards to

Chapter 1

Introductory Chapter

1.1 Background

With the rapid increase in the population of the world, electricity requirements will also tend to increase. It is projected that by 2050, the global energy usage will increase by nearly 50% (Kahan, 2013). Due to the goal of rapid decarbonization, renewable energy will play a major part as a means of providing clean and sustainable energy. A major source of renewable energy is concentrated solar power (CSP) technology, which is quite a remarkable means of producing renewable energy. With advancements in thermal energy storage, round-the-clock electricity production can be achieved with CSP.
Commonly either steam, molten salt or thermal oils have been used as the primary heat transfer fluid in CSP applications. Recent developments have been made in the use of air as a potential heat transfer fluid. There are numerous advantages of using air as a heat transfer fluid. It is free, readily available, environmentally friendly and offers an extensive temperature range for operation. Furthermore, high-temperature exhaust gases can be used for a bottoming cycle on a dual Brayton-Ranking cycle, thereby increasing the efficiency of the plant. However, the major factor for it not being used as a heat transfer fluid is its poor heat transfer characteristics such as low thermal conductivity and density. These necessitate large heat exchanging devices, thereby increasing costs to the plant. To reduce costs, save energy and space, the heat transfer process inside these exchanging devices must be enhanced.

1.2 Introduction

Heat transfer enhancement is one of the most common methods to optimize heat transfer in modern-day heat exchangers. From low cost to compactness, passive inserts are the front runners as a means of achieving this. Passive inserts affect the flow behaviour of the fluid, thereby altering the heat transfer from the wall to the surface of the fluid. A common type of insert called a

twisted tape enhances the heat transfer by inducing swirl to the flow field and altering the hydrodynamic and thermal boundary layers. Twisted tapes can be used in either tubular receivers (used in solar towers) or parabolic trough plants. Since there is a large temperature difference between the tube wall and the fluid, along with a non-uniform heating condition, the tubes risk warping. Furthermore, thermal stresses caused by large temperature gradients could cause tube leakage, decreasing reliability, increasing overhead costs and decreasing the longevity of the plant.
The goal of this research was to design an appropriate heat transfer enhancement device for the use in solar receiver applications. The trade-off between heat transfer and pressure was considered since the pressure drop affects the efficiency of the Brayton cycle. The performance characteristics of the heat enhancement device was computationally investigated to understand the complex flow phenomena that are exhibited by twisted tapes.

1.3 Motivation

The role of efficient heat transfer is not a new concept and has been actively pursued not only in the power generation industry, but also in industries such as refrigeration, chemical plants and food processing amongst others. Having efficient heat transfer in CSP power plants are important for a variety of reasons. If heat transfer is enhanced, receiver tubes can be made smaller and more compact, thereby saving costs and space. The pumping power is also reduced, thereby increasing the efficiency of the power cycle. If heat transfer enhancement can reduce warping and leaks in tubes, the reliability and longevity of the plant is increased, thereby reducing costs. Offering low cost electricity is particularly important in CSP applications since it needs to compete with other forms of electricity production such as solar photovoltaic (PV), wind and hydropower.
It is to the best knowledge of the author that the research carried out is novel for the following reasons:

- Twisted tapes are commonly used in applications where the fluid is mainly in the laminar regime. The literature is not extensive in the use of twisted tapes in the turbulent regime.
- Many if not almost all applications involving twisted tapes investigate the enhancement when the tube is subjected to a uniform flux/temperature all around the tube. This research focuses on one-sided non-uniform heat flux experienced in solar receiver tubes.
- There is currently very little research conducted at elevated heat fluxes, higher pressures ($\gg$ 1atm) and high temperatures ($\gg$ 600K). This re-

search investigates the behaviour of the enhancement at elevated temperatures and pressures subjected to elevated fluxes.

- Many researchers do not investigate the performance of a twisted tape that has been formally optimized for a specific flow application, rather design parameters are varied over a range e.g. pitch ratio, diameter, tape thickness etc. This research focuses on optimizing the geometry of the twisted tape.

1.4 Objectives

The research has the following primary objectives

- Choosing an appropriate passive heat transfer enhancer that is simple, cost-effective and reliable.
- Building computational models and numerically investigating the performance of the enhancer. The computational model must incorporate elevated temperatures, pressures and non-uniform one-sided heat fluxes.
- Performing an appropriate optimization to obtain the best available geometric design.
- Determining if the heat transfer enhancement process is beneficial considering pressure loss and heat transfer.

The author's work focuses on the use of multiple twisted tapes, helically twisted tapes and a modified form of the helically twisted tapes to investigate the thermohydraulic performance inside solar receiver tubes. Additionally, optimization is conducted on the modified form of the helically twisted tape. The research focused on understanding local flow mechanisms that contribute to enhancing the heat transfer which can be used to highlight future work into heat transfer enhancement using twisted tapes.

Chapter 2

Literature Review

This chapter covers the literature review on the basics of heat transfer enhancement. Hydrodynamic and thermal boundary layers are described as they are key fluid mechanics and heat transfer concepts that help describe heat transfer enhancement. Common heat transfer enhancement devices such as twisted tapes, fins, vortex generators are also briefly visited.

2.1 Fundamentals of receivers and Brayton cycles

Concentrated solar power plants use mirrors to concentrate solar radiation onto receivers that are located atop large towers. Receivers are essentially heat exchanging devices that convert the solar radiation to thermal energy via a heat transfer fluid (HTF). Various receiver technologies exist, of which volumetric and tubular receivers are the most common (Kretzschmar and Gauché, 2012). Tubular receivers use either steam or molten salts as a HTF, with recent developments where air is used as a HTF. A major downside of using tubular receivers is its low thermal efficiency and outlet temperatures, which is often coupled with non-uniform heat flux that cause high thermal stresses in tubes. There have been studies and research conducted on air receivers such as Solar-Hybrid Power and Cogeneration (SOLHYCO) receiver that made use of pressurised air operating on a Brayton cycle (Amsbeck *et al.*, 2009). The SOLHYCO receiver was designed to produce an output temperature of 800°C and a tube temperature of 950°C and made use of profiled multilayer tubes (PML). Volumetric receivers are much more efficient and obtain higher outlet temperatures than tubular receivers, however, the major disadvantage of open volumetric receivers is that they are applicable to Rankine cycles (they can be used in Brayton cycle with an additional heat exchanger, but it is not practical) (Ávila Marín, 2011).
Open Brayton cycles compress a gas (usually air) which gains thermal energy (in this case through a tubular receiver) which is then expanded through a tur-

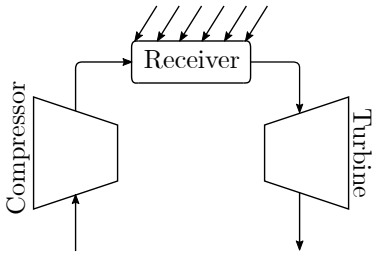

Figure 2.1: Schematic of an open Brayton cycle

bine as seen in Fig 2.1. An increase in the outlet temperatures of the receiver will increase the work output and hence increase the efficiency. Generally, any attempt to increase the heat transfer over the receiver comes at the expense of a pressure drop. In an ideal Brayton cycle, the assumption is that there is no pressure drop over the receiver, whereas in reality, this is far from the truth. The pressure drop over the receiver needs to be carefully looked at, as the efficiency is a strong function of the pressure ratio (Çengel and Boles, 2015*a*).

2.2 Fundamentals of heat transfer

In tubular receivers, heat exchange takes place between a surface of high temperature and a fluid at a lower temperature. Convection is the primary mode of heat transfer, and the heat transfer rate can be represented using Newton's law of cooling Çengel and Ghajar (2015*a*):

$$\dot{Q} = hA(T_w - T_f) \tag{2.1}$$

Where h is the heat transfer coefficient, A is the area through which heat transfer occurs, T_w is the temperature of the wall and T_f is the temperature of the fluid. Generally the heat transfer coefficient h is a function of a number of variables such as geometry, thermodynamic properties and the speed of the fluid. To maximize the outlet temperature of receivers, $\dot{Q}$ needs to be maximized i.e. the amount of heat per unit time imparted into the fluid from the receiver wall. The obvious way is to increase the surface area A, however, this will increase the size of receivers and is costly. The heat transfer can also be increased by increasing the heat transfer coefficient h which usually involves altering the behaviour of the fluid. Various modifiers exist such as mixers, interrupters and inserts that change the flow in heat exchangers.

2.3 Basics of the hydrodynamic and thermal boundary layers

Whenever a fluid flows over a solid surface, due to the 'no-slip' condition the fluid is at rest at the wall i.e. it has a velocity of zero. The velocity increases gradually to equal the velocity in the free stream. The region from zero velocity to 99% of the free stream velocity is termed the boundary layer as shown in Fig 2.2 for a flat plate (Schobeiri, 2010).

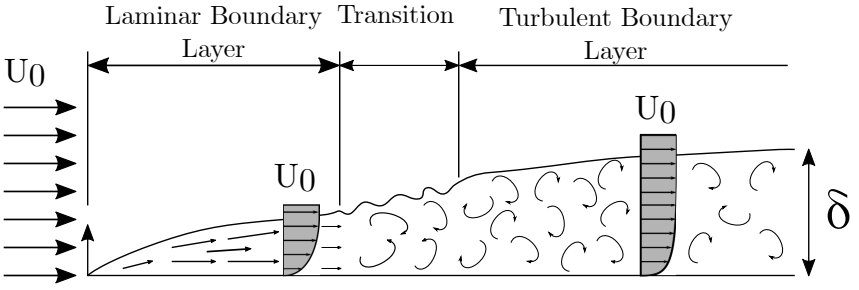

Figure 2.2: Boundary layer on a flat plate

A laminar boundary layer is characterized by smooth orderly flow, which then becomes unstable to transition, followed by turbulent which is chaotic. Analogous to hydrodynamic boundary layer is the thermal boundary layer as seen in Fig 2.3. If a flat plate has a wall temperature T_w, a thermal boundary layer will develop until it reaches the free stream temperature as seen in Fig 2.3. In the boundary layer, viscous effects dominate the inertia effects and heat transfer occurs primarily through conduction, whereas outside the boundary layer the heat transfer is primarily through convection. The hydrodynamic and thermal boundary layer thickness δ and δ_{T} is usually not the same and is characterized by the Prandtl number which is the ratio of momentum diffusivity to thermal diffusivity. If the Prandtl number is close to 1 then the heights of both the hydrodynamic and thermal boundary layers are comparable.

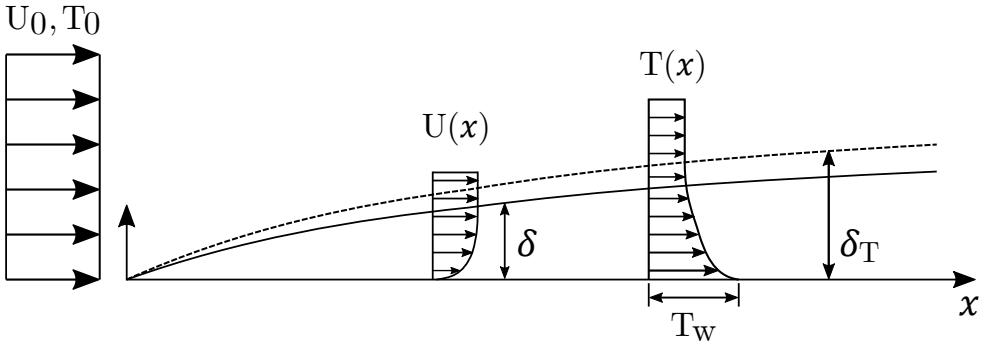

Figure 2.3: Hydrodynamic and thermal boundary layers

Hydrodynamic and thermal boundary layers are important in heat exchanging devices as boundary layer thickness affects the thermal performance. A thicker boundary layer will resist heat transfer and increase the thermal resistance. At higher Reynolds number the boundary layer thickness starts to decrease thereby increasing the heat transfer mechanism and reducing thermal resistance. In general, a laminar boundary layer is thicker than a turbulent boundary layer. Laminar flow does not have the chaotic motion of turbulent flow thus heat exchange between particles is not prominent. When pipe flow is involved, the boundary layer forming around the circumference of the tube will merge from all directions from where onwards the fluid is deemed to be fully developed (commonly taken to be 10 diameters from the entrance). Heat transfer in developed flow is much less than in developing flow due to the gradient of the temperature between the core and mean flow being greater than in developed flow. To improve heat transfer, occasionally the flow is purposefully created to have a boundary layer and entrance effects to exploit higher heat transfer coefficients.
In the presence of an adverse pressure gradient, boundary layer separation is a common occurrence, whereby the boundary layer detaches from the surface forming vortices. Boundary layer separation is advantageous in heat transfer as momentum and thermal diffusion is high i.e. the separated boundary layer removes heat from the wall quite effectively (Smyth, 1974). Disrupting the boundary layer ensures rigorous mixing of the core flow with the boundary layer, hence reducing the thermal resistance. Furthermore, one should not only aim for separation but reattachment as well as seen in Figure 2.4. Separation and reattachment act as tabulators enhancing the heat transfer (Arman and Rabas, 1992). In chaotic turbulent flow, vortices can be seen as pockets that transport heat to the core of the flow. Swirling flow has similar characteristics that improve heat transfer by improving the thermal diffusivity which is done by mixing of the flow.

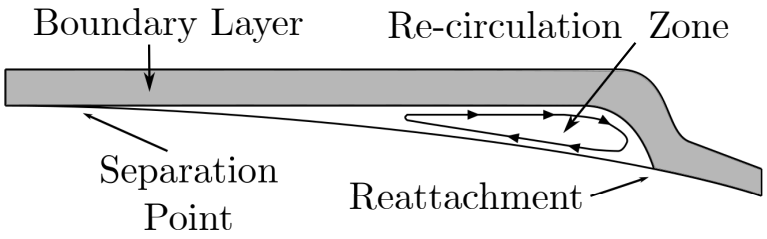

Figure 2.4: Boundary layer separation

2.4 Heat transfer enhancement

Heat transfer enhancement refers to the improvement of heat transfer in a heat exchanger. Usually, heat transfer is enhanced through active or passive

methods. Active methods involve the use of an external power input to enhance heat transfer. Examples of active methods include pulsating cams and plungers, magnetic fields, mechanics aids or mixers, vibration etc (Liu and Sakr, 2013). Passive methods do not make use of external power sources and involve enhancers such as inserts, swirl devices, coils and fins. Compound methods involve any combination of the above two methods. Passive heat transfer enhancement has major advantages over active heat transfer. Passive methods offer reliability and are cost-effective therefore making it the choice of enhancement.
Liu and Sakr (2013) have identified the nine most popular passive heat transfer enhancement methods that are briefly described below:

- Treated surfaces: Surfaces that have some sort of surface finish or coating, commonly used boiling and condensation.
- Rough surfaces: Involve surface modifications like sand-grains, and are commonly used in single-phase flows.
- Extended surfaces: Involves increasing the surface area and modifying flows by enhancers like fins.
- Displaced enhancement devices: Are devices used in confined forced convection. These devices involve displacing the fluid from the heated/cooled surface so as to mix with the core flow.
- Swirl flow devices: These devices mix secondary flow with the axial flow and involve devices such as twisted tapes, helical strips, and screw types.
- Coiled tubes: Commonly used in compact heat exchangers and are responsible for producing secondary flows.
- Surface tension devices: Involves wicking or grooved devices.
- Additives for liquids: Use of solid particles to increase thermal conductivity.
- Additives for gases: Use of liquid droplets or fine solid particles.

2.5 Description of common heat transfer enhancement devices

Over various passive heat transfer enhancers available, there are few common ones that have been extensively researched. Furthermore, these passive enhancers work satisfactorily in most cases. There are two review papers that explain heat transfer enhancements (and previous research) in detail. The first one is by Bergles (1997) and the second one is by Siddique *et al.* (2010), and readers are strongly referred to these for more information.

2.5.1 Twisted tapes

Twisted tapes are common turbulators used in heat exchangers. Heat transfer enhancement is achieved by swirling flow at the periphery of a tube that mixes with the core fluid (Lim *et al.*, 2017). Various modifications also exist and will be described at a later stage.

2.5.2 Fins

Fins come in various designs and provide various heat transfer duties such as cooling in computers, radiators, turbine blades etc. This principle works by increasing the surface area and thus increasing the heat transfer rate. Various and extensive literature is available on fins in both heating and cooling applications.

2.5.3 Ribs

A modified form of a fin, ribs are smaller versions of fins used in complex geometry where fins are not possible to use. Ribs offer a small increase in the heat transfer area as well as the introduction of secondary flow which aids heat transfer (Taslim, 2005).

2.5.4 Vortex generators

These are protrusions extending from the surface. They produce swirl which leads to vortices from the interrupted surface (Awais and Bhuiyan, 2018). Vortex generators reduce boundary layers and cause turbulence thus increasing the heat transfer.

2.5.5 Wire coils

These are circular wires that are wound in spiral form. Wire coils produce swirl close to the wall of the tube as well as turbulence that enhances heat transfer (Garcia *et al.*, 2005). Garcia *et al.* (2005) states that wire coils act as artificial roughness when it is in contact with the tube wall.

2.5.6 Corrugated tubes

These are tubes with grooves on the wall to enhance the heat transfer. The grooves on the wall promote secondary recirculating flow, as well as radial and tangential velocity components (Kareem *et al.*, 2015).

2.5.7 Nanofluids

Nanofluids are fluid with nanoparticles suspended in them. These particles increase the heat transfer area and thermal conductivity of the fluid. The mixing effect is intensified due to the collisions of the particles and fluid (Xuan and Li, 2000).

2.6 Twisted tapes

Though there are plenty of heat transfer enhancers available, perhaps the use twisted tapes stands out more than others, specifically more than the enhancers described before. Twisted tapes can be fabricated with ease, are cost-effective, are very reliable, easy to install and easy to maintain. This makes them particularly attractive in the use of solar thermal plants.
Even though an enhancer may be selected, one still has to evaluate the enhancer. The following parameter can be used to evaluate the effectiveness of the heat transfer enhancer (Eiamsa-ard and Promvonge, 2010).
For constant pumping power:

$$(\dot{V}\Delta P)_e = (\dot{V}\Delta P)_p$$

where $\dot{V}$ is the volumetric flow rate, ΔP is the pressure loss and the subscripts e and p, denote the enhanced design and plain design respectively.
The relationship between Reynolds number and friction factor is as follows:

$$\frac{\mathrm{Re}_e}{\mathrm{Re}_p} = \left(\frac{f_e}{f_p}\right)^{1/3}$$

where Re and f are the Reynolds number and friction factor respectively.

The *thermal enhancement factor*(η), abbreviated as TEF, is defined as the ratio of the heat transfer coefficient of the enhanced design to that of the plain design at same pumping power (PP):

$$\eta = \left.\frac{h_e}{h_p}\right|_{PP} = \frac{\left(\frac{\mathrm{Nu}_e}{\mathrm{Nu}_p}\right)}{\left(\frac{f_e}{f_p}\right)^{1/3}}$$

A value of $\eta > 1$ indicates that the heat transfer enhancement is greater than the pressure drop penalty, and is greatly desired. If $\eta = 1$ then the heat transfer enhancement is equal to that of the pressure drop penalty while $\eta < 1$ indicates that the pressure drop penalty is higher than the heat transfer enhancement achieved.

2.6.1 Flow behaviour for twisted tapes

In ordinary pipe flows, the flow has primarily an axial velocity component with no radial and tangential component. This means that the heat transfer is poor due to a small amount of turbulence at the wall. Twisted tapes offer a considerable amount of swirl which is the primary method of heat transfer enhancement. The heat transfer enhancement can be explained by the following mechanisms (Hasanpour *et al.*, 2014):

- With the addition of twisted tapes, the streamlines and velocity is increased. This increases the turbulence in convection and tangential velocity near the walls.
- The twisted tape induces secondary flows due to swirling, which induces centrifugal force. At low Re, simple swirl is generated i.e. single vortex structure. At higher Re, double vortices with opposite directions are induced which aide heat transfer.

Twisted tapes that induce swirl, usually come with high velocities close to the wall. High tangential velocities are superimposed upon the axial velocities creating turbulence and thus efficient mixing. Tangential velocities continuously break up the boundary layers leading to a much thinner boundary layer than the boundary layer in the plain tube (Eiamsa-ard *et al.*, 2009). Boundary layer separation and reattachment, as mentioned before, is highly advantageous for the effective mixing of the thermal boundary layer into the core flow. Furthermore twisted tapes generate longer pathlines thereby increasing the heat transfer capabilities (Li *et al.*, 2015). A consequence of all of these methods to increase heat transfer results in an increase in pressure drop.

2.6.2 Existing designs and literature on twisted tapes

2.6.2.1 Ordinary twisted tapes

There is extensive literature on the use of single twisted tapes in heat exchangers. Naphon (2006) experimentally investigated the use of single twisted tapes on a counter-flow heat exchanger and proposed correlations for friction factor and Nusselt number. Bas and Ozceyhan (2012) experimentally investigated twisted tapes placed separately from tube walls as seen in Figure 2.5, to obtain an increase in heat transfer that is purely dependent on the laminar sublayer destruction near the tube wall.

Figure 2.5: Single twisted tape investigated by Bas and Ozceyhan (2012)

2.6.2.2 Multiple twisted tapes

Multiple twisted tapes are a number of smaller twisted tapes. Eiamsa-ard *et al.* (2010) investigated two twisted tapes in tandem for different twist and space ratios. Promvonge *et al.* (2012) investigated a helical ribbed tube with double twisted tapes and a ribbed tube. Their results showed that the ribbed tube with double twisted tape had a higher thermal enhancement factor than just a ribbed tube. Samruaisin *et al.* (2018) investigated quadruple twisted tape with varying space ratio and arrangement (co, counter and cross arrangement) as seen in Figure 2.6. The counter arrangement with the smallest spacing performed the best. Piriyarungrod *et al.* (2018) investigated 2,3,4,5 and 6 twisted tapes, and the configuration of 6 twisted tapes performed best of all the designs.

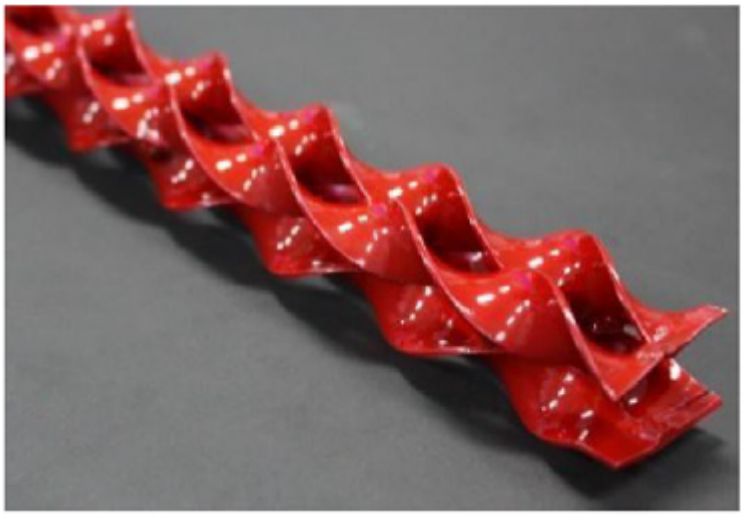

Figure 2.6: Quadruple twisted tapes investigated by Samruaisin *et al.* (2018)

2.6.2.3 Modified twisted tapes

There are various modifications that exist to twisted tapes in an attempt to enhance the heat transfer. Perforated, notched and jagged twisted tapes were investigated by Rahimi *et al.* (2009) and showed that the jagged twisted tapes performed the best. Serrated twisted tapes by Chang *et al.* (2007), staggered twisted tapes with holes by Lei *et al.* (2012) as seen in Figure 2.7, twisted tapes with rectangular holes by Boonloi and Jedsadaratanachai (2016), square-cut twisted tapes by Saysroy and Eiamsa-ard (2017) and louvred twisted tapes by Ghadirijafarbeigloo *et al.* (2014) were also investigated which all showed very promising results. There are many more modifications that exist however due to the extensive literature, they are not discussed here.

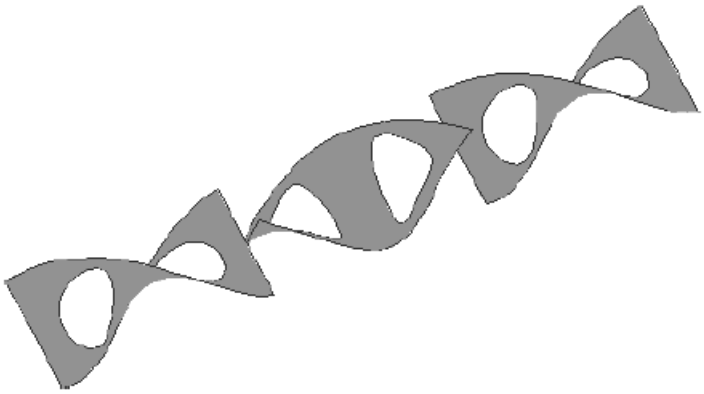

Figure 2.7: Staggered twisted tape with holes investigated by Lei *et al.* (2012)

2.6.2.4 Helically twisted tapes

Helically twisted tapes (HTT) are very small twisted tapes wound in a helical coil form in an attempt to increase turbulence (Eiamsa-ard *et al.*, 2012) as seen in Figure 2.8. Eiamsa-ard *et al.* (2012) investigated co- and counter-swirl flow with HTT's and determined that HTT with co-swirl performed better. Nanan *et al.* (2013) investigated HTT's with perforations to decrease friction and determined that a perforated HTT performs better than an ordinary HTT. In an attempt to bring swirl in the primary flow, Yongsiri *et al.* (2016) investigated HTT with alternate axis inserts which performed better than an ordinary HTT.

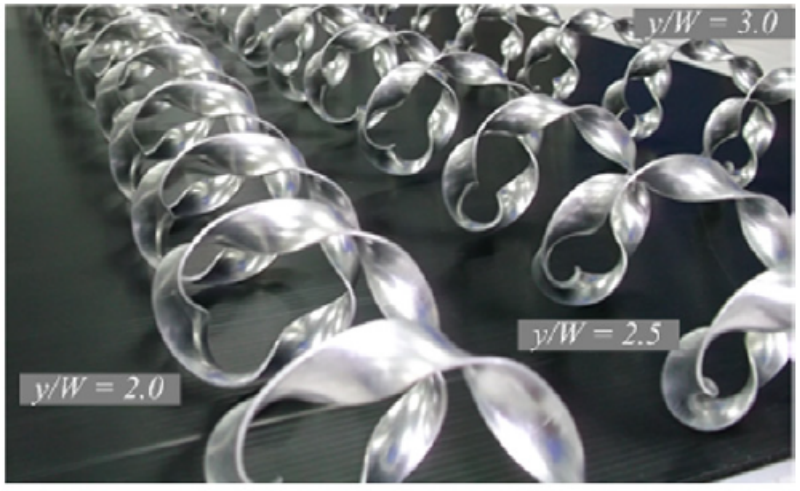

Figure 2.8: Helically twisted tapes investigated by Eiamsa-ard *et al.* (2012)

Chapter 3

Numerical Methods and Optimization

It is understood now that the thermohydraulic behaviour of twisted tapes needs to be simulated using numerical methods. The numerical simulations were performed using ANSYS Fluent to model fluid behaviour and heat transfer. Optimization is used to obtain the 'best' possible design of twisted tape. This section describes the numerical and optimization procedure used.

3.1 Governing equations

The fluid used will be air which is a Newtonian fluid, while the flow field can be described using the Navier-Stokes equations. The flow is assumed to be steady while the influence of gravity is negligible in forced convection problems and is hence ignored. The governing equations for conservation of continuity, momentum and energy are given below (Versteeg and Malalasekera, 2007*a*).

Continuity:
$$\nabla \cdot (\rho \boldsymbol{V}) = 0 \tag{3.1}$$

Momentum:
$$\rho (\boldsymbol{V} \cdot \nabla) \boldsymbol{V} = -\nabla p + \nabla \cdot \boldsymbol{\tau} \tag{3.2}$$

Energy:
$$\rho \nabla \cdot (h \boldsymbol{V}) = -\nabla p + \nabla \cdot (k \nabla T) + \boldsymbol{\Theta} \tag{3.3}$$

where ∇ is the del operator, $\boldsymbol{V}$ is the velocity vector, p is the pressure field, $\boldsymbol{\tau}$ is the viscous stress tensor, T is the temperature, $\boldsymbol{\Theta}$ is the dissipation function,

ρ is the density, h is the enthalpy and k is the thermal conductivity.
The stress tensor component can be represented as follows:

$$\tau_{ij} = \mu \left(\frac{\partial V_i}{\partial x_j} + \frac{\partial V_j}{\partial x_i} - \frac{2}{3} \left(\nabla \cdot \boldsymbol{V} \right) \delta_{ij} \right)$$

where μ is the dynamic viscosity and δ_{ij} is the Kronecker delta.
The dissipating function can be represented as:

$$\boldsymbol{\Theta} = \tau_{ij} \frac{\partial V_i}{\partial x_j}$$

3.2 Turbulence modelling

The governing equations can be easily solved if the flow is laminar, however, should the flow be turbulent the equations are rather difficult to solve. Currently, there exist no closed-form solution of the Navier Stokes equations, thus the equations above need to be solved using a model that replicates the fluid behaviour. Currently, there are three methods to solve turbulence problems, Reynolds Average Navier-Stokes (RANS), Large Eddy Simulation (LES) and Direct Numerical Simulation (DNS). LES and DNS, which require extensive computational power, are not used and will not be discussed.
RANS modelling is the modelling method of choice and will thus be discussed here (Versteeg and Malalasekera, 2007*b*). RANS equations are time-averaged equations that describe the fluid based on Reynolds decomposition (Versteeg and Malalasekera, 2007*b*). The Reynolds decomposition describes flow properties such as density, velocity, pressure and temperature as fluctuations (ϕ') superimposed on the mean property (Φ):

$$\phi = \phi' + \Phi \tag{3.4}$$

Obtaining RANS equations involves taking the time average of the governing equations and readers are directed to Versteeg and Malalasekera (2007*b*) for the full explanation. Once the full set of RANS equations are obtained, six addition stresses are retrieved named Reynolds stresses shown below.

$$\tau'_{ij} = \rho \overline{u'_i u'_j} \tag{3.5}$$

where u'_i and u'_j indicates a velocity fluctuation, and the overbar indicates a time average. It is often difficult to obtain the Reynolds stresses directly, and thus the Boussinesq approach is used that links the Reynolds stresses to the mean rates of deformation.

$$\tau'_{ij} = \rho \nu_t \left(\frac{\partial V_i}{\partial x_j} + \frac{\partial V_j}{\partial x_i} \right) - \frac{2}{3} \rho k \delta_{ij} \tag{3.6}$$

where $\nu_t = \mu_t/\rho$ is the turbulent kinematic viscosity and μ_t is the turbulent dynamic viscosity.
Similar to the time averaged momentum equation, the extra terms in the time averaged energy equation can be written as:

$$\overline{u_i' T'} = -\frac{\nu_t}{\sigma_t}\frac{\partial T}{\partial x_j}$$

where σ_t is the turbulent Prandtl number. Similar to a turbulent viscosity is the turbulent thermal conductivity k_t.
The turbulent viscosity and thermal conductivity cannot be calculated easily, and there are many unknowns. Therefore, turbulence models were created to model these properties.

3.3 Turbulence models

There are many turbulence models available, and they are commonly categorized by the number of extra transport equations. Transport equations are equations that describe how a certain quantity is transported through space e.g. concentration. A zero equation turbulence model, as the name says, has zero extra transport equations, with the most common being the Prandtl mixing length model (Versteeg and Malalasekera, 2007*b*). The Spalart-Allmaras (SA) is a common one equation model used widely in the aerodynamic industry (Versteeg and Malalasekera, 2007*b*). By far the most common turbulence models are two equation turbulence models from which the $k-\epsilon$ and $k-\omega$ (and variations such as the RNG $k-\epsilon$ and SST $k-\omega$) are widely used in industry (Versteeg and Malalasekera, 2007*b*). A rather expensive model compared to the $k-\epsilon$ and the $k-\omega$ models is the seven equation Reynolds stress model. All of these models are further described below.
The mixing length model is formulated by the product of a velocity and length scale along a constant of proportionality, with the length scale dependent on the size of the eddies. The mixing length model is relatively cheap and easy to implement. It works well for thin shear layers, boundary layers, jets, wakes etc, however, its major downfall is that it cannot describe complicated flow or flow with separation and recirculation (Versteeg and Malalasekera, 2007*b*). Therefore it is not a good model to use for twisted tapes. The Spalart-Allmaras model is a one equation model which has a transport equation for the kinematic turbulent viscosity and a corresponding length scale utilizing an algebraic formula. It works well for boundary layers subjected to adverse pressure gradients and mildly complex flows, however, it performs poorly for complex geometries (Versteeg and Malalasekera, 2007*b*).
Two equation turbulence models are used over zero or one equation models as they define the velocity and length scales much better, can handle separation and recirculation as well as complicated geometry, are better for swirling and

rotating flows and vast improvements in the near-wall regions (Versteeg and Malalasekera, 2007*b*). By far the most common turbulence models are two equation models, namely the $k-\epsilon$ and $k-\omega$ models. The $k-\epsilon$ model has two transport equations, one for the turbulent kinetic energy k and another for the rate of dissipation of turbulent kinetic energy ϵ. These two variables are used to define appropriate velocity and length scale. The $k-\epsilon$ model is pretty simple and works well for many industrial applications, and is the most validated of all the turbulence models (Versteeg and Malalasekera, 2007*b*). However, it is an extremely poor model for many applications such as unconfined flows, curved boundary layers, swirling and rotating flows (Versteeg and Malalasekera, 2007*b*).
Another widely used model is the $k-\omega$ model which has two transport equations, one for turbulent kinetic energy k and another for the specific rate of dissipation ω. It works well for boundary layer problems and wall-bounded flows, but is sensitive to inlet free stream conditions (Versteeg and Malalasekera, 2007*b*). Nonetheless, it is a good turbulence model that is suitable for twisted tapes. The Reynolds Stress Model (RSM) has a total of seven transport equations. It calculates mean flow properties and all the Reynolds stresses for many flows such as curved flows and jets. It is also good for severe strain gradients, however, the RSM is computationally expensive, and performs poorly just like the $k-\epsilon$ model in recirculating and separating flow, and is hence not worth the extra effort (Versteeg and Malalasekera, 2007*b*).
There are variations that improve the $k-\epsilon$ and $k-\omega$ models, namely the Renormalization Group (RNG) $k-\epsilon$ model and the Shear-Stress Transport (SST) $k-\omega$ model. The RNG $k-\epsilon$ improves the handling of strain and works well for separating flow and recirculating over a backward facing step (Versteeg and Malalasekera, 2007*b*). The SST $k-\omega$ model is an improvement of the $k-\omega$ model, and will be the turbulence model of use for the remainder of this study (which will be shown later on). The SST $k-\omega$ is good for predicting separation and recirculation (Versteeg and Malalasekera, 2007*b*). The SST $k-\omega$ model uses a blending function to use the $k-\omega$ model close to the wall and the $k-\epsilon$ model in the free stream, therefore removing the dependency of inlet conditions.

3.4 Wall treatment

It is important to model fluid close to the wall accurately, as walls are the main source of turbulence and vorticity in wall bounded flows that affect important quantities such as velocity, pressure and temperature. Furthermore, fluid behaviour such as separation and recirculation are strongly affected by walls. The region close to the wall consists of a viscous sublayer (inner layer), log-law layer (overlap layer) and an outer layer (Versteeg and Malalasekera, 2007*b*). The inner layer is primary dominated by viscous forces while the

outer is dominated by inertial forces. The log-law layer is the region where both viscous and inertial forces are important. The law of the wall states that there is a relationship between the velocity and the distance from the wall, which are represented in dimensionless variables u^+ and y^+, where u^+ is the dimensionless velocity and y^+ is the dimensionless distance. Similar to the fluid mechanics problem, in heat transfer problem there exists a dimensionless temperature T^+ (Mills and Ganesan, 2009).
In the viscous sublayer, the shear stress is approximately constant and it can be shown that the velocity profile behaves linearly in relation to the distance from the wall (Versteeg and Malalasekera, 2007*b*).

$$u^+ = y^+ \tag{3.7}$$

In the log-law layer, there exists a logarithmic relation between the velocity and the dimensionless distance.

$$u^+ = \frac{1}{\kappa}\ln(y^+) + B \tag{3.8}$$

Where κ is von Karman's constant $\kappa \approx 0.4$, and B is a constant that is dependent on the wall roughness, commonly taken to be $B \approx 5.5$ for smooth walls (Versteeg and Malalasekera, 2007*b*). The outer region is free from viscous effects and can be described using the 'law of the wake' which is dependent on the boundary layer thickness amongst other things.
There are two methods for predicting fluid behaviour close to the wall. The first method is integrating through the boundary layer directly i.e. the mesh is fine enough to be resolved through the entire boundary layer (Versteeg and Malalasekera, 2007*b*). This means that the mesh cells needs to be highly concentrated in regions close to the wall (ideally $y^+ \approx 1$, but $y^+ \leq 5$) which implies that it is computationally expensive. The second method involves using wall functions which model near wall effects to satisfy the physics and the first cell needs to be placed somewhere in the log-law layer ($30 \leq y^+ \leq 500$) (Versteeg and Malalasekera, 2007*b*). This ensures that the there is a reduction in cell count. The method of choice is dependent on the turbulence model of choice, where $k-\epsilon$ models prefer the log-law layer and $k-\omega$ models prefer resolving the boundary layer completely. The method for velocity can be extended to temperature treatment close to the wall using T^+. It cannot be stressed how important it is to ensure that the treatment of velocity and temperature close to the wall is correctly predicted and the results achieved are accurate. Hence care needs to be taken in ensuring the mesh is of acceptable quality.

3.5 Shear-Stress Transport (SST) $k-\omega$ model

With a brief introduction to the common turbulence models, the SST $k-\omega$ model is described in more detail. The standard $k-\epsilon$ model is not a near wall

model, furthermore it is not a low Reynolds number model. This is because it performs poorly in this region. A substitute for that is the $k-\omega$ model which is a low Reynolds number and essentially a near wall model. The behaviour of $k-\omega$ models in the logarithmic region is better than the $k-\epsilon$ model in adverse pressure gradients and compressible flows (Menter, 1994). However in the wake region (free stream) the $k-\omega$ model behaves rather poorly due to its sensitivities to free stream conditions (Menter, 1994). The $k-\epsilon$ model at low Reynolds number usually requires damping functions because the log-law is not valid (Versteeg and Malalasekera, 2007*b*). Due to its poor wall treatment the $k-\epsilon$ model does not perform well for internal flows, flows with strong curvature, rotating and swirling flows where the $k-\omega$ model can perform well. It is important that the near-wall region is predicted accurately in the flow, as this affects the heat transfer. A good prediction of the flow will ensure that the transport of heat is consequently well predicted.
Menter (1994) created a hybrid between the $k-\omega$ and $k-\epsilon$ model, where the $k-\epsilon$ model is transformed into a $k-\omega$ model (by substituting $\epsilon = k\omega$) close to the wall region and utilizing the $k-\epsilon$ model far from the wall (Versteeg and Malalasekera, 2007*b*). Blending functions are used to ensure smooth transition between the two models. The turbulent viscosity is also limited in adverse pressure gradients that could build up turbulence. The entire model is called the SST $k-\omega$ model that ensures good near wall behaviour of the $k-\omega$ model and the robustness of the $k-\epsilon$ model (Versteeg and Malalasekera, 2007*b*). The SST $k-\omega$ model is described below in brief detail, however readers are directed to Menter (1994) for a full explanation.
The turbulent viscosity is defined as:

$$\mu_t = \frac{\rho a_1 k}{\max(a_1\omega, \Omega F_2)} \tag{3.9}$$

The transport equation for turbulent kinetic energy (k) and specific dissipation rate (ω) are:

$$\frac{\partial(\rho k)}{\partial t} + \frac{\partial(\rho u_j k)}{\partial x_j} = P - \beta^*\rho\omega k + \frac{\partial}{\partial x_j}\left[(\mu + \sigma_k\mu_t)\frac{\partial k}{\partial x_j}\right] \tag{3.10}$$

$$\begin{aligned}\frac{\partial(\rho\omega)}{\partial t} + \frac{\partial(\rho u_j\omega)}{\partial x_j} =& \frac{\gamma}{\nu_t}P - \beta\rho\omega^2 + \frac{\partial}{\partial x_j}\left[(\mu + \sigma_\omega\mu_t)\frac{\partial\omega}{\partial x_j}\right] \\ &+ 2(1-F_1)\frac{\rho\sigma_{\omega 2}}{\omega}\frac{\partial k}{\partial x_j}\frac{\partial\omega}{\partial x_j}\end{aligned} \tag{3.11}$$

where the variables are defined as follows:

$$P = \tau_{ij}\frac{u_i}{x_j}$$

$$\tau_{ij} = \mu_t \left(2S_{ij} - \frac{2}{3}\frac{\partial u_k}{\partial x_k}\delta_{ij} \right) - \frac{2}{3}\rho k \delta_{ij}$$

$$S_{ij} = \frac{1}{2}\left(\frac{\partial u_i}{\partial x_j} + \frac{\partial u_j}{\partial x_i} \right)$$

$$\phi = F_1 \phi_1 + (1 - F_1)\phi_2$$

$$F_1 = \tanh(\arg_1^4)$$

$$\arg_1 = \min\left[\max\left(\frac{\sqrt{k}}{\beta^* \omega d}, \frac{500\nu}{d^2\omega} \right), \frac{4\rho\sigma_{\omega 2} k}{\mathrm{CD}_{k\omega} d^2} \right]$$

$$\mathrm{CD}_{k\omega} = \tanh(\arg_2^2)$$

$$\arg_2 = \max\left(2\frac{\sqrt{k}}{\beta^* \omega d}, \frac{500\nu}{d^2\omega} \right)$$

with the constants for closure being: $\sigma_{k1} = 0.85$, $\sigma_{\omega 1} = 0.65$, $\beta_1 = 0.075$, $\sigma_{k2} = 1$, $\sigma_{\omega 2} = 0.856$, $\beta_2 = 0.0828$, $\beta^* = 0.09$, $a_1 = 0.31$

3.6 Numerical techniques

The governing equations are discretized using the finite volume method (FVM). Since the flow is not highly compressible a pressure based solver was used. The coupling between pressure and velocity was achieved by using a coupled solver. A coupled solver offers robustness and stability especially for complex flow such that of the twisted tapes (Xiao *et al.*, 2017). The Green-Gauss Node Based method is used to discretize the gradient. It is slightly more expensive than the least squares method, however it does well in boundary layer flows, over curved surfaces and complex geometry, especially for unstructured grids (Syrakos *et al.*, 2017). The second order upwind scheme is used to discretize the remainder of the equations such as pressure (second order), momentum, turbulent kinetic energy, turbulent dissipation rate and energy. The second order scheme is slightly more computationally expensive than the first order however it ensures that flow properties are transported downstream, is more accurate than first order and counters numerical diffusion (Versteeg and Malalasekera, 2007*c*).

3.7 Grid convergence

As one changes the mesh size from a coarse mesh to a fine mesh, it is expected that the results of a variable will also change. In CFD it is important that grid convergence is reached i.e. results do not change with any subsequent increase in mesh size. This ensures correct reporting of results, decreases uncertainty

and error, and embodies confidence in the results. Not only should one perform a grid convergence study, but one should report it in the best manner. Two methods of reporting grid convergence are the brute force method and the grid convergence index.

The brute force method begins with a very coarse mesh and simply proceeds to build many finer meshes. Following this, one tracks the relative error to a satisfactory convergence criteria. There are various downsides to this method. Firstly there is no systematic order of refinement, so the final results can be deceiving. Secondly there is no formal method of reporting these results.

A more formal technique to quantify grid convergence is using the grid convergence index (GCI) formulated by Roach based on Richardson extrapolation (Roache, 1994). The GCI measures the percentage of the result that is away from its asymptotic range and also gives an error band e.g. 5% from the asymptotic solution. The method of GCI is originally meant for structured grids but can be used for unstructured grids with a much higher safety factor. There are two things one could do with a GCI, the first is to estimate the error between the different grids while the second is to use GCI to estimate a more accurate solution. Roy (2003) suggests the former as the latter will magnify any errors such as discretization, roundoff etc. Furthermore, Roy (2003) states that an extrapolated solution is not necessarily conservative i.e. locally conservativeness may be met, however on a global scale the solution may not be conservative. A brief explanation of the GCI is given here, however for a more detailed explanation the reader is directed to Roache (1994). For an unstructured/non uniform grid refinement the following method can be used to estimate GCI on a fine mesh which is not only used in CFD but FEA analysis as well (Schwer, 2008).

Consider three grid sizes N_1,N_2 and N_3 representing the number of cells in a fine,medium and coarse mesh respectively. The fine, medium and coarse meshes have solutions ϕ_1, ϕ_2 and ϕ_3 respectively. It then follows that the errors between the meshes are: $e_{32} = \phi_3 - \phi_2$ and $e_{21} = \phi_2 - \phi_1$. The refinement ratio between the grids are:

$$r_{21} = \sqrt[D]{\frac{N_2}{N_1}} \text{ and } r_{32} = \sqrt[D]{\frac{N_3}{N_2}} \tag{3.12}$$

where D represents the dimension, in the case of a 3D simulation $D = 3$.

The apparent order of convergence can therefore be calculated as:

$$p = \frac{\left| \ln \left| \frac{e_{32}}{e_{21}} \right| + q(p) \right|}{\ln r_{21}} \tag{3.13}$$

$$q(p) = \ln \left(\frac{r_{21}^p - s}{r_{32}^p - s} \right) \tag{3.14}$$

$$s = \operatorname{sgn} \left(\frac{e_{32}}{e_{21}} \right) \tag{3.15}$$

where 'sgn' is the signum function which is dependent on the sign of the argument as follows:

$$\text{sgn}(x) = \begin{cases} 1 & \text{if } x > 0 \\ 0 & \text{if } x = 0 \\ -1 & \text{if } x < 0 \end{cases} \tag{3.16}$$

Eq 3.13 has to be solved iteratively with $q(p) = 0$ being the initial solution. It then follows that the GCI can be calculated as:

$$\text{GCI}_{21} = F_s \frac{e_\phi}{r_{21}^p - 1} \tag{3.17}$$

where F_s is the safety factor and $e_\phi = \left| \frac{\phi_1 - \phi_2}{\phi_1} \right|$ is the relative error between the final two meshes.
Roache (1997) recommends a safety factor of 1.25 for three of more meshes and mentions that although he initially recommended a safety of 3, it might be overly conservative. If an unstructured grid is used, a safety factor of above 2 should be more than adequate. The safety factor can be thought of as representing a 95% confidence band (Roy, 2003). Furthermore, Roache (1994) uses a refinement ratio of 2, however in the case of 3D simulations a refinement ratio of 2 might be quite excessive in cell count. Hence one can aim for a refinement ratio of 1.2-1.3 with a much larger safety factor. A GCI of less than 5% can be seen as a good convergence level.

3.8 Optimization procedure

Optimization involves finding the best design or the optimum design which involves maximizing or minimizing a function. The steepest descent is a common iterative method in finding the maximum or minimum. This section briefly describes the optimization algorithm used to optimize a design.
Consider the following mathematical optimization problem (Snyman and Wilke, 2018):

$$\begin{aligned} \underset{\text{w.r.t}\,\mathbf{x}}{\text{minimize}} \quad & f(\mathbf{x}),\ \mathbf{x} \in \mathbb{R}^n && \text{(3.18a)} \\ \text{subject to} \quad & g_j(\mathbf{x}) \leq 0, \quad j = 1, 2, \ldots, m, && \text{(3.18b)} \\ & h_j(\mathbf{x}) = 0, \quad j = 1, 2, \ldots, r && \text{(3.18c)} \end{aligned}$$

where $f(\mathbf{x})$ is the objective function defined on $\mathbb{R}^n$ which is the n dimensional Euclidean space, $g_j(\mathbf{x})$ is inequality constraint function and $h_j(\mathbf{x})$ is the equality constraint function which are all functions of a vector $\mathbf{x}$ where $\mathbf{x} = [x_1, x_2, x_3, \ldots, x_m]^T$ with m being the number of design variables.
The Spherical Quadratic Steepest Descent (SQSD) method is used to optimize a solution that is *unconstrained* (Snyman and Hay, 2001). This method

is quite attractive for a few reasons, it is relatively quick to converge, does not involve the calculation of the Hessian matrix and has a self-determining step length.
At iteration $\mathbf{k}$ with $\mathbf{x^k}$ and $f(\mathbf{x^k})$ available, the vector $\mathbf{x}$ at the next iteration point $\mathbf{k+1}$ can be calculated as:

$$\mathbf{x^{k+1}} = \mathbf{x^k} - \frac{\nabla f(\mathbf{x^k})}{c^{\mathbf{k}}} \tag{3.19}$$

where ∇f is the gradient vector a function f and the quadratic function $c^{\mathbf{k}}$ is:

$$c^{\mathbf{k}} = \frac{2\left[f(\mathbf{x^{k-1}}) - f(\mathbf{x^k}) - \nabla^T f(\mathbf{x^k})(\mathbf{x^{k-1}} - \mathbf{x^k})\right]}{\|\mathbf{x^{k-1}} - \mathbf{x^k}\|^2} \tag{3.20}$$

with $\|\cdot\|$ being the Euclidean norm.

The iterative procedure to apply the SQSD method is as follows:
Select a convergence criteria $\in_g$ and $\in_x$ and a steplimit $d > 0$ along with an initial design vector $\mathbf{x}^0$. Set $c^0 = \frac{\|\nabla f(\mathbf{x}^0)\|}{d}$ and let $\mathbf{k} = 1$

1. If $\left\|\nabla f(\mathbf{x^{k-1}})\right\| < \in_g$, then $\mathbf{x}^* \simeq \mathbf{x^{k-1}}$ and stop, else:

$$\mathbf{x^k} = \mathbf{x^{k-1}} - \frac{\nabla f(\mathbf{x^{k-1}})}{c^{\mathbf{k-1}}}$$

2. If $\left\|\mathbf{x^k} - \mathbf{x^{k-1}}\right\| > 0$ then set:

$$\mathbf{x^k} = \mathbf{x^{k-1}} - \frac{\nabla f(\mathbf{x^{k-1}})}{\|\nabla f(\mathbf{x^{k-1}})\|}$$

   if $\left\|\mathbf{x^k} - \mathbf{x^{k-1}}\right\| < \in_x$ then $\mathbf{x}^* \simeq \mathbf{x^k} \simeq \mathbf{x^{k-1}}$.

3. Set:

$$c^{\mathbf{k}} = \frac{2\left[f(\mathbf{x^{k-1}}) - f(\mathbf{x^k}) - \nabla^T f(\mathbf{x^k})(\mathbf{x^{k-1}} - \mathbf{x^k})\right]}{\|\mathbf{x^{k-1}} - \mathbf{x^k}\|^2}$$

   If $c^{\mathbf{k}} < 0$ then set $c^{\mathbf{k}} = 10^{-60}$

4. $k = k + 1$ and return to 1.

Here $\mathbf{x}^*$ denotes the optimum solution.
The SQSD algorithm is for unconstrained minimization. When a constrained problem is at hand, one can convert the constrained problem to an unconstrained problem using the penalty method that imposes a penalty if a constraint is violated. The constrained problem is converted to an unconstrained

problem as follows (Snyman and Wilke, 2018).

$$\underset{\text{w.r.t}\,\mathbf{x}}{\text{minimize}} \quad P(\mathbf{x}),\ \mathbf{x} \in \mathbb{R}^n \tag{3.21}$$

where

$$P(\mathbf{x}) = f(\mathbf{x}) + \sum_{j=1}^{r} \rho_j h_j(\mathbf{x})^2 + \sum_{j=1}^{m} \beta_j g_j(\mathbf{x})^2 \tag{3.22}$$

with $\boldsymbol{\rho}$ and $\boldsymbol{\beta}$ simply being the penalty parameter vectors and $P(\mathbf{x}, \boldsymbol{\rho}, \boldsymbol{\beta})$ being the penalty function. Snyman and Wilke (2018) recommends $\rho_j = \beta_j = 10^4$ if the constraint functions are normalized in some sense (or all have the same dimensions in some cases).

It can be seen that if a constraint is not violated the second and third terms of Eq 3.22 are zero and the penalty function is simply the original function while the squares in the second and third terms of Eq 3.22 are simply there to impose a harsher penalty. Penalty functions are quite effective as they are quick and easy to implement and there is no need to find an initial feasible point (Bryan and Shibberu, 2015). The downside of the penalty function is the problem can quickly become ill-conditioned as the penalty parameters are increased with large gradients and various kinks and changes (Bryan and Shibberu, 2015). It was seen previously that the SQSD algorithm is for minimization problems, however, one could simply extend it to cover maximization problems as follows (Snyman and Wilke, 2018) :

$$\underset{\text{w.r.t}\,\mathbf{x}}{\text{maximize}} \quad f(\mathbf{x}) = \underset{\text{w.r.t}\,\mathbf{x}}{\text{minimize}} \quad \{-f(\mathbf{x})\} \tag{3.23}$$

with constraint change $\tilde{g}_j(\mathbf{x}) = -g_j(\mathbf{x})$

Chapter 4

Numerical Simulation and Optimization

This chapter constitutes the bulk of the research conducted for this thesis. It includes the validation of a classical twisted tape against available literature. This is followed by an investigation into multiple twisted tapes and helically twisted tapes. After an appropriate design is created, an optimization procedure is carried out to determine the best geometrical configuration. This is followed by a complete final simulation on the optimized design to determine the effectiveness of the optimized heat transfer enhancement device.

4.1 Validation of a plain tube and single twisted tape

Validation is a primary tool in assessing the reliability as well as the accuracy of a CFD model, and how well it represents the physics. This is commonly done by assessing the CFD model with an established benchmark, and if possible estimating the error. Furthermore, validation imbues confidence in the results obtained and gives the reader the view that the results are of acceptable quality. This section discusses the validation of a plain tube and a tube inserted with a single twisted tape.

Consider an ordinary tube that has diameter D and length L which is representative of a plain tube. A tube with the same dimensions has a single twisted tape insert, as seen in Fig 4.1a, which represents the enhanced design. The tape has a tape height y, a half twist pitch (or half pitch) W which consists of a 180° turn and a tape thickness δ as seen in Fig 4.1b. The twist ratio is defined as the ratio of the half pitch to the tape height (W/y). When the tape has a tight fit inside the tube, the tape height is equivalent to the tube diameter ($y = D$), otherwise, the tape height is smaller than the diameter ($y < D$).

The simulation is a fully turbulent 3D simulation, with the fluid being liquid water that is incompressible. Water is used as a heat transfer fluid since it was

one of the heat transfer fluids used in the experiments by Manglik and Bergles (1993) to create correlations for twisted tapes. The fluid has constant thermodynamic properties at a temperature of 300K. The thermodynamic properties at this temperature are as follows: density $\rho = 997$ kg/m^3, constant specific heat $C_p = 4180$ J/kgK, thermal conductivity $k = 0.6103$ W/mK and dynamic viscosity $\mu = 0.0008538$ Pa.s. Furthermore, to simulate fully developed flow, there a developing tube of length $L = 10D$ as well as a calming tube to prevent flow reversal at the outlet.

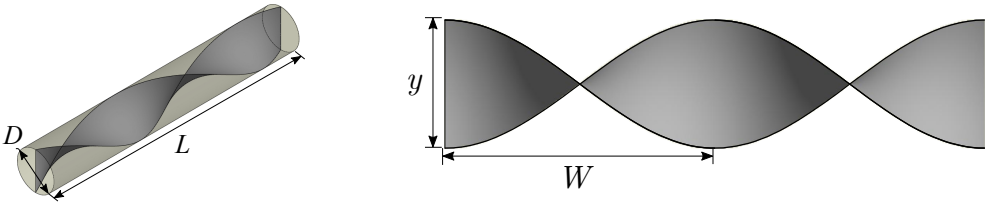

(a) Configuration

(b) Geometry of a twisted tape

Figure 4.1: Single twisted tape

4.1.1 Plain tube validation

The plain tube has a diameter of $D = 0.05$ m and length $L = 0.3$ m, which is heated. Water enters the tube at a temperature of $T_{\text{inlet}} = 300$ K and a uniform heat flux of $q = 5000$ W/m^2 is imposed uniformly around the entire tube. The Reynolds number at the inlet, based on the diameter, is varied from 15000 to 21000 and enters fully developed. The turbulence model of choice is the RNG $k-\epsilon$ with enhanced wall treatment. Later on, it will be shown that the SST $k-\omega$ is the model of choice for all subsequent simulations. Results for friction factor and Nusselt number are compared to Petukhov and Gnielinski correlations respectively (Çengel and Ghajar, 2015*b*):

$$f_{\text{Petukhov}} = \left[0.79\log(\text{Re}) - 1.64\right]^{-2} \tag{4.1}$$

$$\text{Nu}_{\text{Gnielinski}} = \frac{\frac{f}{8}(\text{Re} - 1000)\,\text{Pr}}{1 + 12.7\left(\frac{f}{8}\right)^{0.5}\left(\text{Pr}^{2/3} - 1\right)} \tag{4.2}$$

The definitions of the Darcy friction factor, Nusselt number and Reynolds number used are:

$$f = \frac{\Delta P}{\frac{L}{D}\rho^2\frac{v_b^2}{2}} \tag{4.3}$$

$$\text{Nu} = \frac{q}{T_{\text{wall}} - T_b}\left(\frac{D}{k}\right) \tag{4.4}$$

$$\mathrm{Re} = \frac{\rho v D}{\mu} \tag{4.5}$$

where ΔP is the pressure drop across the length of the tube, v_b is the bulk velocity which is defined as the average velocity of the inlet and outlet $\left(v_b = \frac{v_i + v_o}{2}\right)$, T_{wall} is the average wall temperature, T_b is the bulk temperature of the fluid defined as the average of the inlet and outlet temperatures $\left(T_b = \frac{T_i + T_o}{2}\right)$, k is the thermal conductivity and μ is the dynamic viscosity. The graphs for friction factor and Nusselt number are shown in Fig 4.2, and it can be seen that the results are satisfactory with the available correlations. The results are within ±4.1% for friction factor and ±9.8% for Nusselt number with reference to the correlations. The Petukhov correlation is within 5-6% while the Gnielinski correlation is within ±20% compared to experimental results (Coetzee, 2015).

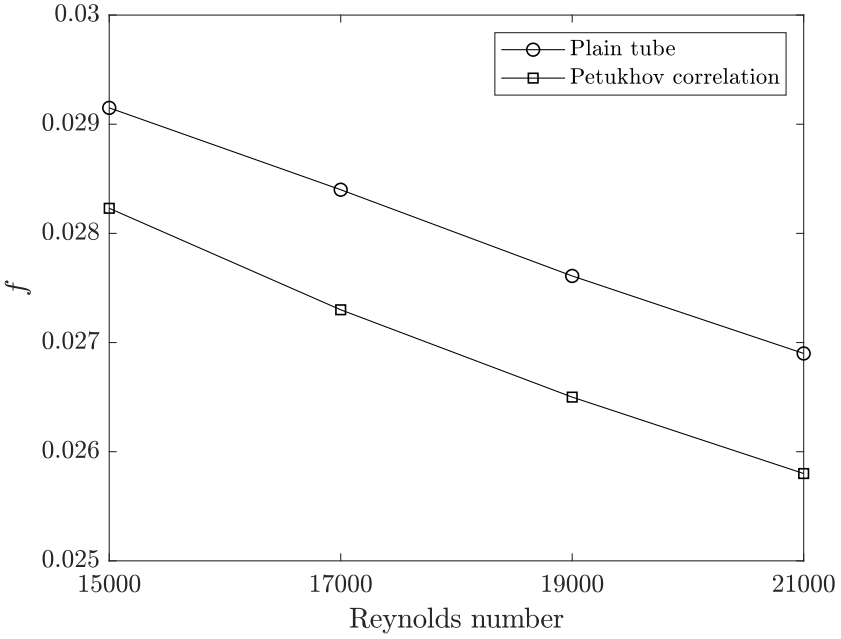

(a) Friction factor

Figure 4.2: Simulation results for plain tube

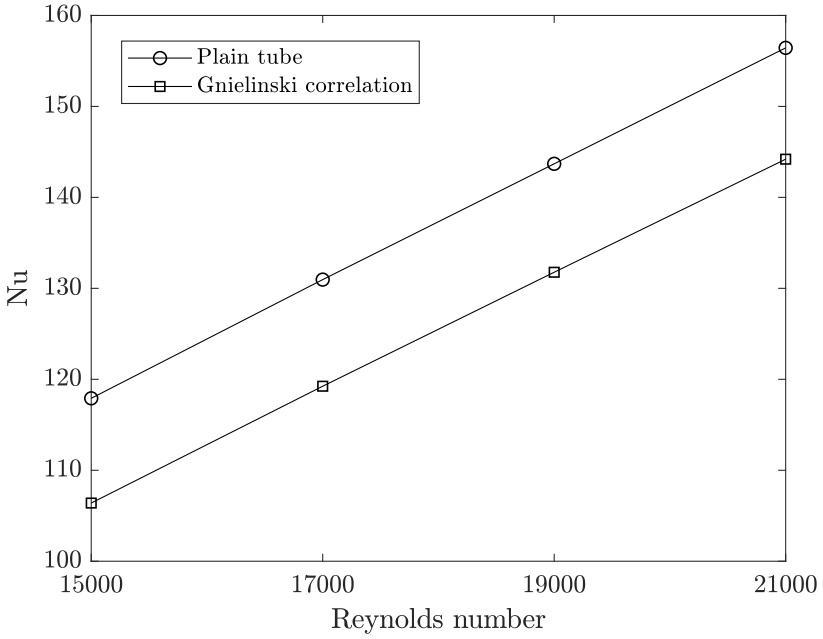

(b) Nusselt number

Figure 4.2: Simulation results for plain tube

4.1.2 Single twisted tape

A simulation of a single twisted tape snug fit in a tube was simulated. The dimensions of the tube are the same as before, while the twisted tape had the same height as the diameter of the tube $y = 0.05$ m and the half pitch is $W = 0.15$ m which corresponds to a twist ratio $W/y = 3$. The tape also had a thickness $\delta = 1$ mm. The fluid enters the tube at a temperature of $T_{\text{inlet}} = 300\text{K}$ while a uniform heat flux of $q = 5000$ W/m^2 is imposed around the tube. The flow enters the tube fully developed and the Reynolds number is varied from 15000 to 21000. The RNG $k - \epsilon$ with enhanced wall treatment turbulence model is used, followed by the standard $k - \epsilon$ model, the standard $k - \omega$ model and the SST $k - \omega$ model.
Five different mesh sizes were used to perform a mesh independence study at Re = 15000, consisting of 353829 cells, 652646 cells, 1300801 cells, 2454780 cells and 4727988 cells. This corresponds to an average refinement ratio of roughly $r \approx 1.22$. To ensure that the results close to the wall are captured in detail, the $y^+_{\text{average}} \approx 1$ and the boundary layer is directly resolved. To ensure that the results for velocity and temperature are accurate enough, the inflation layer is made up of 15 layers. Fig 4.3 graphs the brute force results for both friction factor and Nusselt number. The relative errors between the final two meshes are $\pm 0.2\%$ for friction factor and $\pm 0.15\%$ for Nusselt number. The GCI is then used, as previously described, with a safety factor of 3. GCI of 0.05%

and 0.15% were achieved for friction factor and Nusselt number respectively. It can hence be concluded that using both the brute force method and GCI, that mesh independence was reached.

The simulation was performed at four different Reynolds numbers using the RNG $k-\epsilon$ with enhanced wall treatment turbulence model. The numerical results were compared to the correlation provided by Manglik and Bergles (1993) which are shown below. The results were within a range of ±9% for friction factor and ±17.5% for Nusselt number.

$$f = \frac{0.316}{\mathrm{Re}^{0.25}} \left(\frac{\pi}{\pi - \frac{4\delta}{D}} \right)^{1.75} \left(\frac{\pi + 2 - \frac{2\delta}{D}}{\pi - \frac{4\delta}{D}} \right)^{1.25} + \left(1 + \frac{2.752}{\frac{W}{y}^{1.29}} \right) \tag{4.6}$$

$$\mathrm{Nu} = 0.023 \mathrm{Re}^{0.8} \mathrm{Pr}^{0.4} \left(1 + \frac{0.769}{\frac{W}{y}} \right) \left(\frac{\pi}{\pi - \frac{4\delta}{D}} \right)^{0.8} \left(\frac{\pi + 2 - \frac{2\delta}{D}}{\pi - \frac{4\delta}{D}} \right)^{0.2} \phi \tag{4.7}$$

with $\phi = \left(\frac{\mu_b}{\mu_\mathrm{w}} \right)^{0.18} \approx 1$ where μ_b is the bulk viscosity of the fluid and μ_w is viscosity of the fluid at the wall.

The graphs for both friction factor and Nusselt number and Nusselt number are shown in Fig 4.4 and agree with the correlations provided by Manglik and Bergles. A maximum error of ±9% and ±17.5% are obtained for friction factor and Nusselt number respectively. Correlations provided by Manglik and Bergles are within ±10% of available literature.

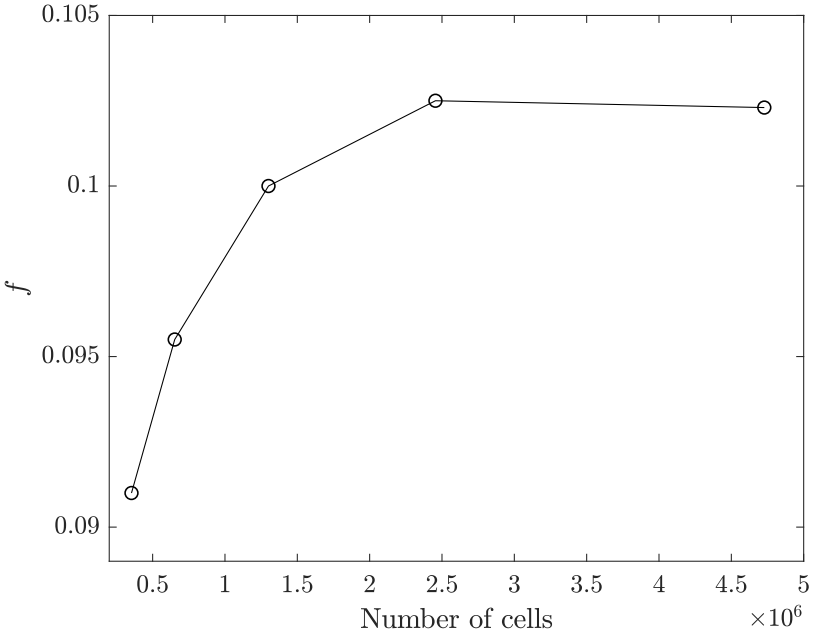

(a) Friction factor

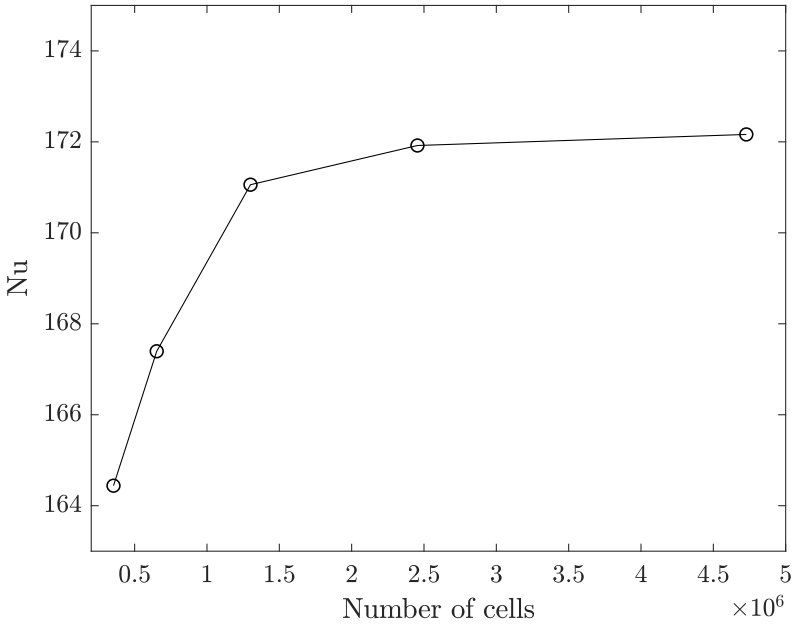

(b) Nusselt number

Figure 4.3: Mesh independence for a single twisted tape at Re = 15000

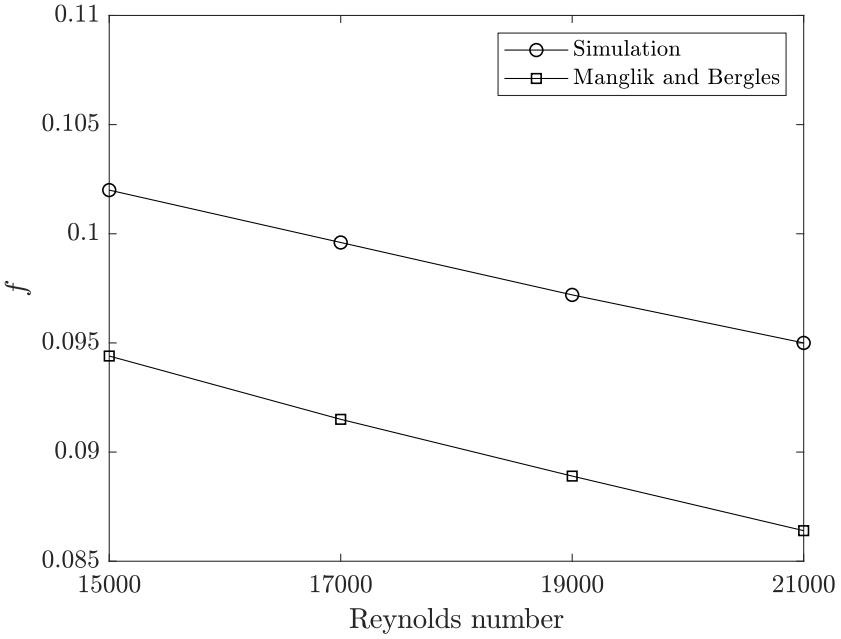

(a) Friction factor

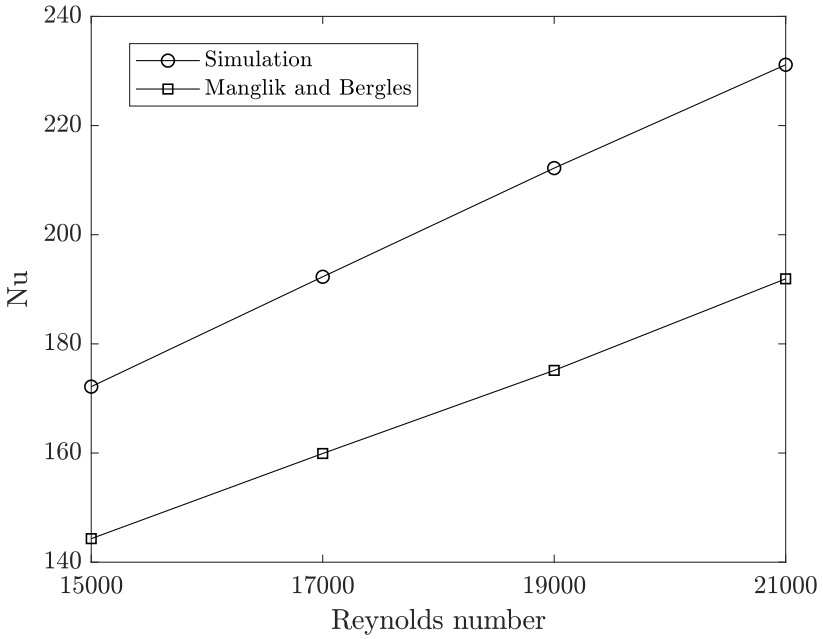

(b) Nusselt number

Figure 4.4: Simulation results for a single twisted tape

It is perhaps prudent at this stage to explore the various turbulence models which can be applied to a single twisted tape. Along with the RNG $k - \epsilon$ with EWT model, three other turbulence models were investigated namely,

the standard $k-\epsilon$ model, the standard $k-\omega$ model and the SST $k-\omega$ model. All four turbulence models are compared to the correlations by Manglik and Bergles and are shown in Fig 4.5. The standard $k-\omega$ model and SST $k-\omega$ model predict the friction factor and Nusselt number extremely well, while the RNG $k-\epsilon$ with EWT model predicts it satisfactorily. The standard $k-\epsilon$ model predicts the friction factor and Nusselt extremely poorly. The maximum errors compared to Manglik and Bergles are shown in Table 4.1.

Table 4.1: Maximum errors for various turbulence models compared to Manglik and Bergles

Turbulence model	**Friction factor error (%)**	**Nusselt number error (%)**
RNG $k-\epsilon$ with EWT	9	17.5
SST $k-\omega$	6.4	2
Standard $k-\omega$	7.5	3
Standard $k-\epsilon$	30	65.5

4.1.3 Discussion of Results

The validation of a plain tube, as well as a tube with a single twisted tape insert, was conducted are compared against existing literature. The RNG $k-\epsilon$ with EWT compared well against correlations by Petukhov and Gnielinski and are within the confidence band provided by Petukhov and Gnielinski. This is due to the fact that the flow in the plain is not rotating/swirling, does not have flow separation, and is a rather simple flow, hence the $k-\epsilon$ model can predict the flow behaviour, such as velocity and temperature, fairly well. The tube with a twisted tape insert was validated against correlations developed by Manglik and Bergles. From the four turbulence models, the SST $k-\omega$ model performed the best while the $k-\epsilon$ model performed rather poorly. This is because the $k-\epsilon$ turbulence model is not a low Reynolds number model, and is not designed to capture near-wall effects such as hydrodynamic and thermal boundary layers. Furthermore, swirling is poorly predicted by $k-\epsilon$ models. This is improved by using an enhanced wall treatment that improves the near-wall modelling of velocity and temperature by the use of blending functions (Versteeg and Malalasekera, 2007*b*). The $k-\omega$ and SST $k-\omega$ perform extremely well, simply due to their nature of being near-wall models and being able to handle curved boundary layers and swirling/rotating and separating flow. In addition, $k-\omega$ models are low Reynolds number models that can handle hydrodynamic and thermal boundary layers. The SST $k-\omega$ model has the lowest error and fits well in the confidence interval provided by Manglik and Bergles. Hence the simulations of both plain tubes and tubes with twisted tape inserts will be simulated by using the SST $k-\omega$ turbulence model.

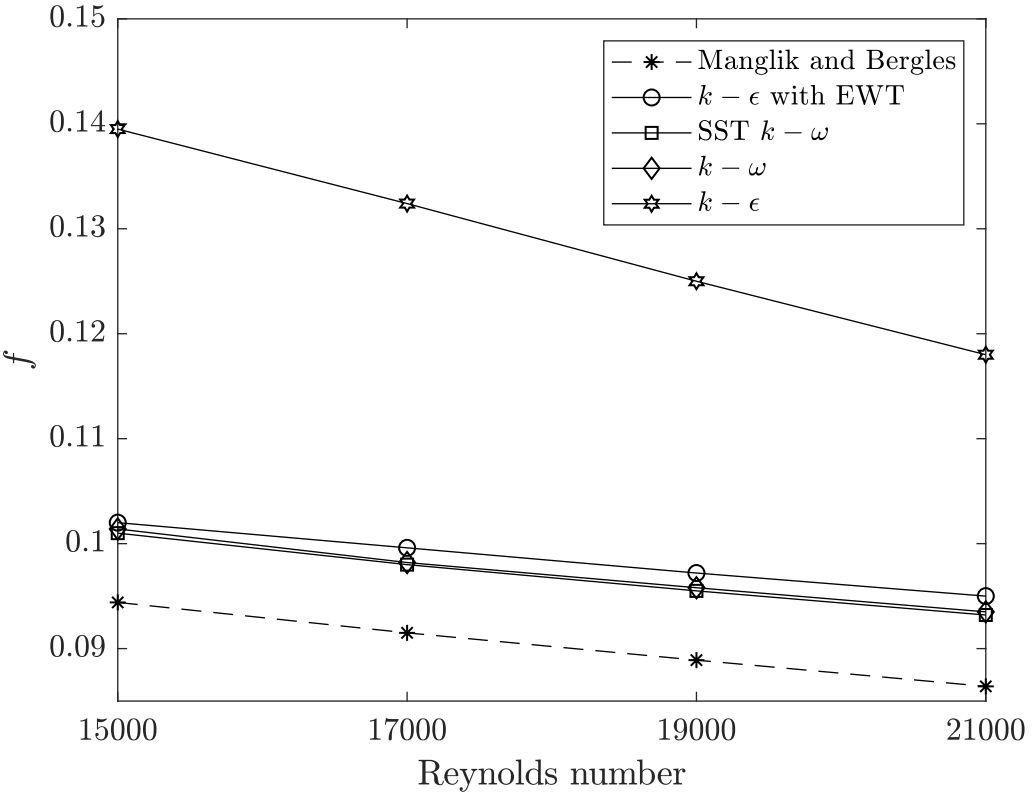

(a) Friction factor

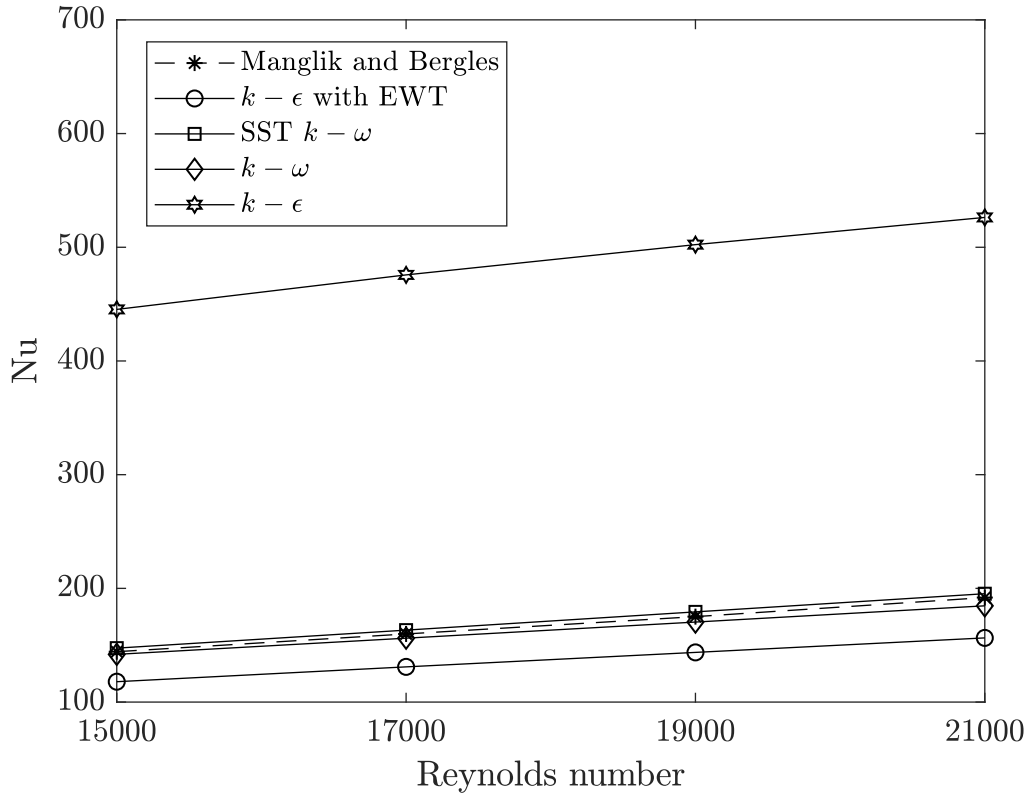

(b) Nusselt number

Figure 4.5: Comparison of various turbulence models

4.2 Multiple twisted tapes

A single twisted tape is advantageous for several reasons, it is simple, easy to install and maintain and is cost-effective. However, in the application of CSP, there are a few disadvantages:

- CSP applications typically involve a non-uniform one-sided heat flux. Therefore there are regions where there is no heat transfer present, but there is a pressure drop. This will decrease the efficiency of the design.
- There is a pressure drop in the core region, where there is very little to no thermal resistance.
- There should be an attempt to break up the hydrodynamic and thermal boundary layer only in the region of the applied heat flux. If the boundary layer is broken up in regions where the heat flux is not applied, it comes with an unnecessary pressure drop.

This means that the use of a single twisted tape is not very useful in CSP applications and could lead to a decrease in efficiency. This led to the design of multiple twisted tapes to be used in CSP applications. Multiple twisted tapes (MTT) are several small twisted tapes clustered in regions of the heat flux specifically designed to interfere and break up the thermal boundary layer. The design process for the multiple twisted tapes was as follows, start with a simple design i.e. two twisted tapes, and build onto that design. This is termed the 'design process'. In the design process, the different designs are compared and evaluated against one another to see if any design was successful.
Before explaining the numerical analysis, a brief description of a generic geometry is described. The tube has a diameter $D = 0.05$ m and a length $L = 0.1$ m. To ensure all the designs are comparable on performance the following are kept constant: all the twisted tapes have a constant twist ratio $W/y = 3$ and a thickness of $\delta = 1$ mm. All the twisted tapes have a clearance of $t = 1$ mm from the tube wall. This is to ensure that the meshing can be easily handled, if $t < 1$ mm then there are very poorly skewed cells close to the wall and the inflation layer cannot be correctly captured. Furthermore as the number of tapes increases, if $t < 1$ mm then cells around the tape could also be of a bad quality. All the twisted tapes have the same twist direction, which is chosen so the designs can be compared and is an arbitrary choice. Furthermore, all the designs are subjected to the same fluid properties, heat flux and Reynolds number. A one-sided heat flux is applied as seen in Fig 4.6. The term 'Twisted Tape Cluster' in Fig 4.6 means that all/majority the twisted tapes are clustered in the regions of the applied one-sided heat flux.

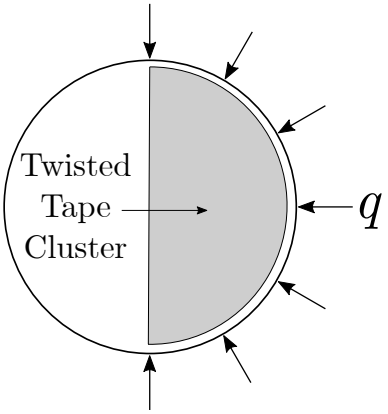

Figure 4.6: One sided heat flux

4.2.1 Numerical method

The simulation conducted is a full 3-D steady turbulent simulation, using the SST $k-\omega$ turbulence model. A pressure based solver is used since the fluid is a low speed and mildly 'compressible'/'incompressible' since the Mach number is less than 0.3 and hence, there is no need for a density based solver. The fluid is incompressible air with thermodynamic properties that are constant and evaluated at 300K. The fluid can be assumed incompressible since the bulk density of fluid remains nearly constant for a short length tube and the Mach number is less than 0.3. Furthermore, accelerating flows tend to resist flow separation better than constant velocity (or nearly constant velocity) flows. This means that there is a larger recirculation region in constant velocity flows, and hence a poorer heat transfer. This ensures that the approach taken is conservative. The thermodynamic properties are: density $\rho = 1.165$ kg/m^3, constant specific heat $C_p = 1006$ J/kgK, thermal conductivity $k = 0.0263$ W/mK and dynamic viscosity $\mu = 1.868 \times 10^5$ Pa.s. The air enters the tube at $T_{\text{inlet}} = 300$ K at a Reynolds number of Re = 20000. A one-sided uniform heat flux of $q = 10000$ W/m^2 is applied as previously mentioned.
The flow configuration is shown in Fig 4.7. The inlet of the flow is a velocity inlet, while the outlet is pressure outlet whose static pressure is set to zero. The heated wall has a constant heat flux condition and all the walls have a no slip condition. The twisted tape walls have a no slip condition, and it is assumed that the twisted tape itself does not transfer/conduct heat i.e. the thermal contact resistance is infinite. This is due to the 1mm air gap between the wall and the tape. The convergence criterion is set to 1×10^{-6} for continuity, momentum, k and ω while energy is set to 1×10^{-8}, and monitors are also ensured to be converged. The velocity magnitude monitors are set at the inlet and outlet which are based on a mass weighted average, there are total pressure monitors at the inlet and outlet which are based on an area weighted average, the total inlet and outlet temperatures are mass weighted averages while the

total wall temperature is an area weighted average of the heated wall i.e. the wall of the applied heat flux. It should be noted that friction factors and Nusselt numbers are evaluated in the heated region of the tube *only* where the twisted tapes lie, and not for the developing and calming sections since the interest lies only in the heated section of the setup. A coupled solver is used for pressure-velocity coupling, and the Green-Gauss node based method is used to discretize the gradient. Second order upwind schemes are used to discretize the remainder of the equations. The simulation uses a hybrid initialization technique, and to prevent divergence in the solution, the V multigrid cycle is used with 3 pre and post sweeps. The solution converges within 1000 iterations.

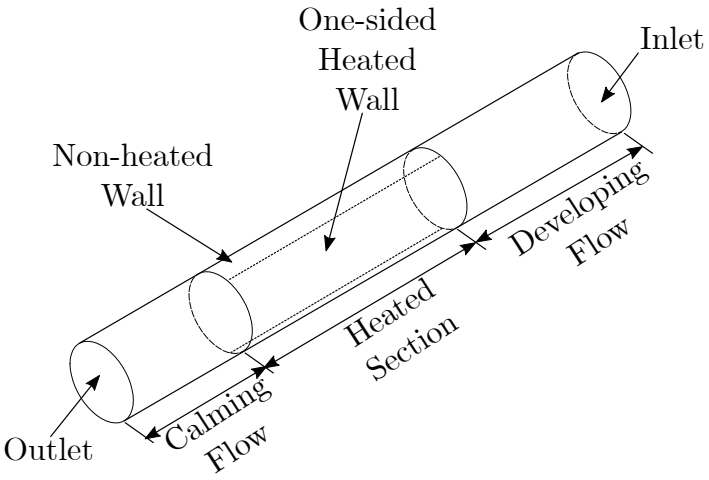

Figure 4.7: Flow configuration

4.2.2 Design description

As mentioned before, there are five different designs that were simulated and are described below. The designs were systematically changed from the initial design to the final design.

4.2.2.1 Two twisted tapes in tandem

The first design consists of two twisted tapes in tandem (on top of each other) as seen in Fig 4.8. Each twisted tape has a height of $y = 23.5$ mm on the same pitch circle diameter (PCD) with the applied heat flux being on the right hand side of the tube.

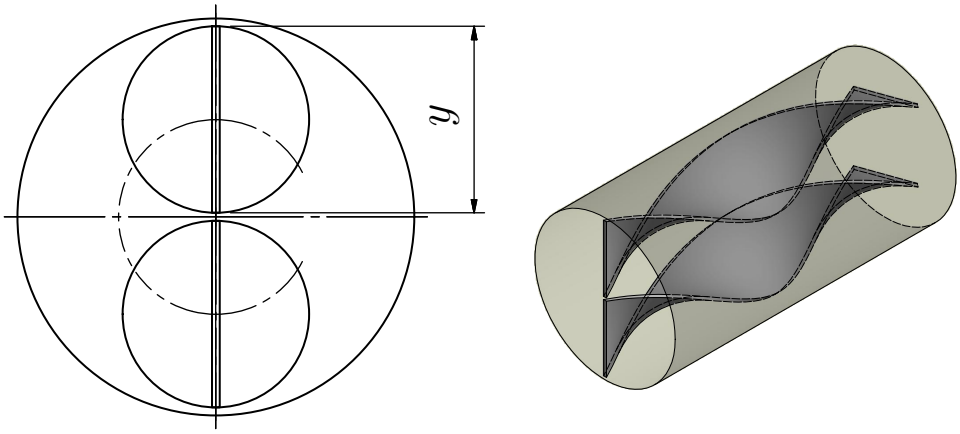

Figure 4.8: Two twisted tapes in tandem

4.2.2.2 Three twisted tapes equispaced

The second design consists of three twisted tapes that are equispaced at an angle of 120° from each other on a PCD as seen in Fig 4.9. The height of each twisted tape is $y = 20$ mm. Two of the three twisted tapes are in the vicinity of the heat flux. The third tape is not in the vicinity of the heat flux and is situated there to potentially mix the fluid.

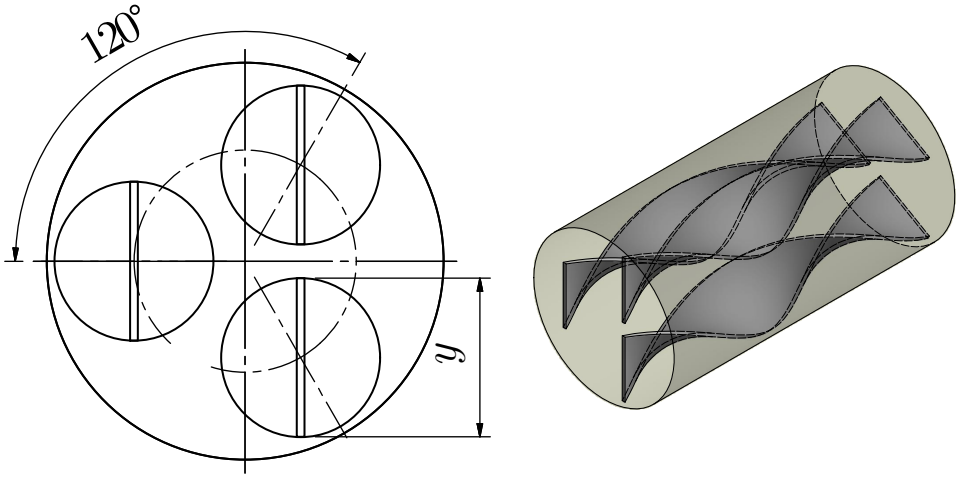

Figure 4.9: Three twisted tapes equispaced

4.2.2.3 Four twisted tapes

The third designs consists of four twisted tapes clustered around the wall of the applied heat flux as seen in Fig 4.10. All the tapes have a height $y = 20$ mm and are situated on a PCD with the first tape having an offset angle of 22.5° from the vertical and each subsequent tape is separated by an angle of 45° from the first tape.

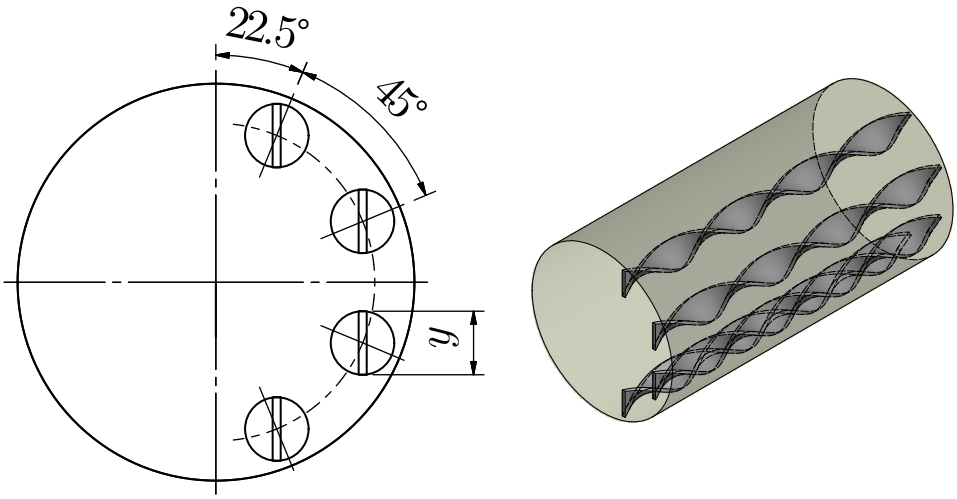

Figure 4.10: Four twisted tapes

4.2.2.4 Five twisted tapes

The fourth designs consists of five twisted tapes, and is an extension of the design with four twisted tapes as seen in Fig 4.11. The fourth design has two types of a tapes, namely a larger tape and four smaller tapes. The large tape has a height $y_1 = 20$ mm while the four small tapes have a height $y_2 = 8$ mm. The larger tape was introduced to potentially mix any of the 'hotter' flow with the 'cold' flow in the core.

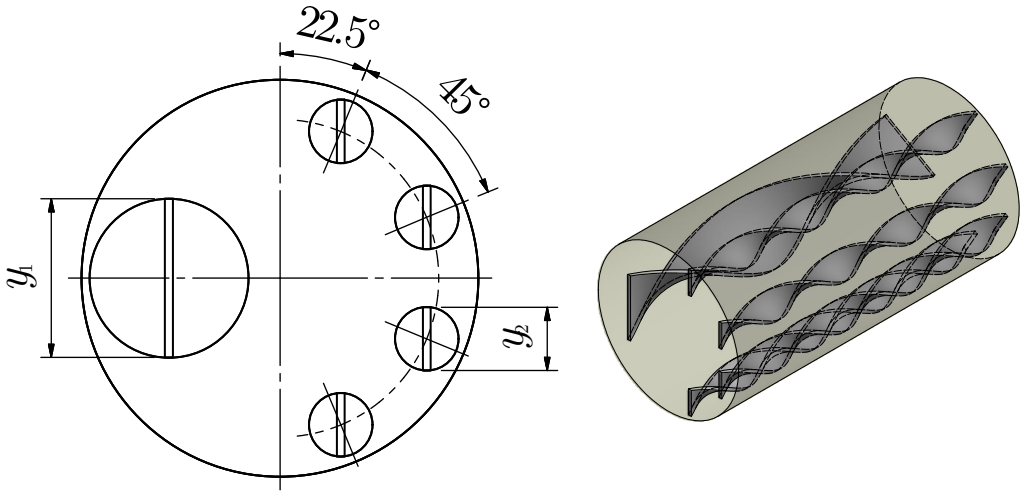

Figure 4.11: Five twisted tapes

4.2.2.5 Eight twisted tapes

The fifth and final design consists of eight twisted tapes all with a height of height of $y = 8$ mm situated on a PCD as seen in Fig 4.12. Each twisted is

separated at an angle 25.71° from each other.

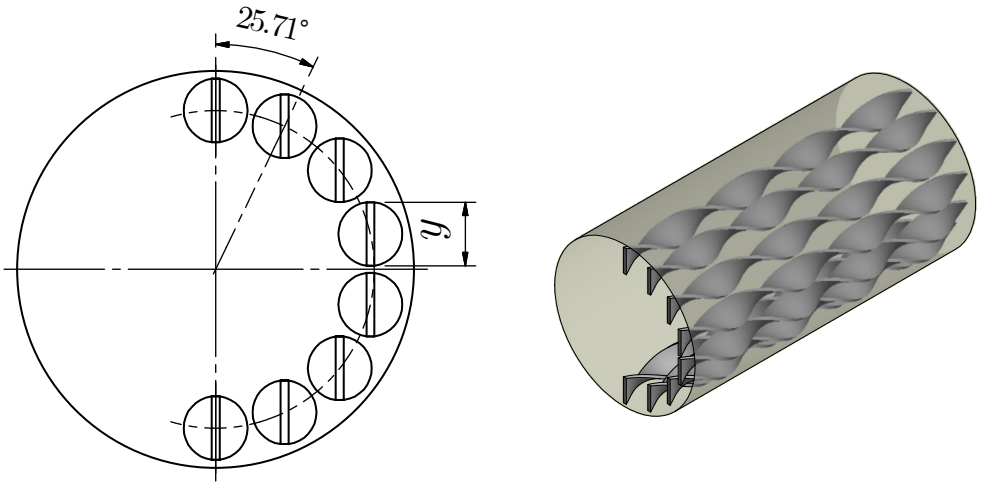

Figure 4.12: Eight twisted tapes

4.2.3 Meshing description

Before describing the meshing strategy, mesh independence is described. Mesh independence was conducted on all five designs individually. There are both advantages and disadvantages to this method. The advantage is that a proper mesh independence study that is done on all the designs, and hence the solution on the final mesh is mesh independent and accurate. The downside to this is that it is time consuming. It is expected that the number of cells would increase as the number of tapes increases, hence one mesh cannot be used for all designs. A possible alternative to this is to perform a full mesh independence study on the first design, and ensure that the relative cell size is the same for all subsequent designs i.e. to adapt the mesh on all subsequent designs. A possible manner in which the relative cell size can be expressed is $\partial x/\partial$tape where 'x' is an appropriate length scale of a cell and '∂tape' is an appropriate length scale of the tape e.g. height of tape. The advantage is that this is less time consuming, however, it is not absolutely certain that mesh independence has been reached, and hence the results could/could not be accurate. Nonetheless, a proper mesh independence study was performed on all five designs.
Each design had a minimum of atleast three meshes, and along with the relative error, the GCI was monitored for both friction factor and Nusselt number. Table 4.2 describes the summary of the mesh independence. The GCI for both friction factor and Nusselt number used a safety factor of 3 ensuring that the solution is a conservative one. A GCI of less than 1% was aimed for, to ensure that the results are comparable.

Table 4.2: Mesh independence for multiple twisted tapes

Number of twisted tapes	**Mesh Size (number of cells)**	**Average refinement ratio r**	**GCI friction factor (%)**	**GCI Nusselt number (%)**
Two	Coarse - 2036576 Medium - 3272079 Fine - 5618323	1.18	0.1	0.85
Three	Coarse - 2266058 Medium - 3681594 Fine - 5628847	1.16	0.03	0.35
Four	Coarse - 2504636 Medium - 3755093 Fine - 5791028	1.15	0.4	0.02
Five	Coarse - 3184346 Medium - 4684598 Fine - 6867261	1.13	0.06	0.5
Eight	Coarse - 1531698 Medium - 4154572 Fine - 6115612	1.4	0.2	0.68

The meshing strategy of five twisted tapes is discussed here, however, it can be extended to all other designs. The mesh is composed of unstructured tet elements since a relatively complex geometry is involved as seen in Fig 4.13. Tet elements are not the best of the available elements, however, they are best suited for complex geometry such as high curvature. The CFD results are only good if the mesh is of acceptable quality. One way of controlling the quality of the mesh is to ensure that the skewness is low and having a well defined smooth mesh. The average skewness of the entire mesh was ensured to be less than 0.3, while the maximum skewness was kept under 0.9. If the skewness exceeds 0.9, temperature/velocity spikes could occur at the highly skewed cells. The mesh was also set up to ensure that there were a large number of cells close to curvature and proximity regions such as between the wall of the tube and the wall of the tape.

One of the important aspects of the meshing procedure was capturing boundary layer effects, and thus inflation layers were added for the walls of the tube and twisted tapes as seen in Fig 4.14. Atleast 35 layers made up the inflation layer and it was ensured that the $y^+_{\text{avg}} = 1$ for all the walls. Very close to the wall, there is a possibility that the inflation layers of the tube and tape could collide. To prevent this, layer compression is preferred over stair stepping.

Stair stepping can create badly skewed cells and does not capture boundary layer effects, leading to numerically unstable and incorrect solutions. Furthermore, there are atleast a total of 3 cells between the gap of the tube and tape (excluding the inflation layer). Both the inflation layer compression and the number of cells across the gap can be seen in Fig 4.15.

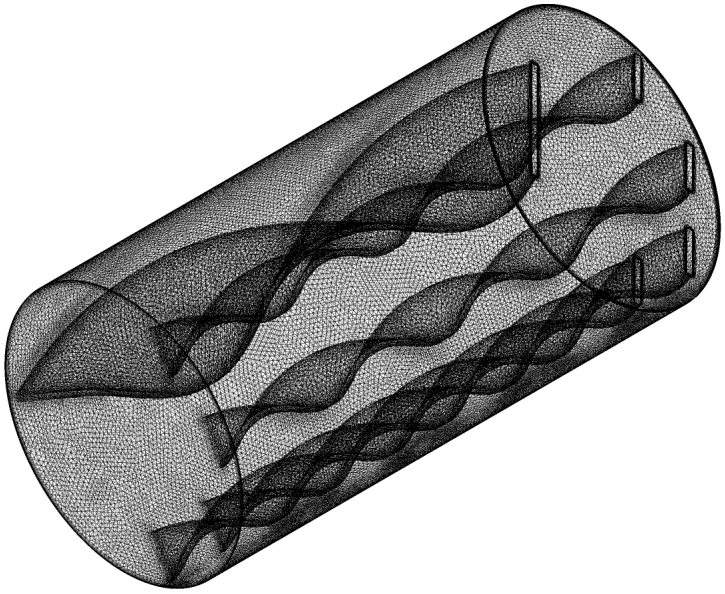

Figure 4.13: Unstructured mesh for five twisted tapes

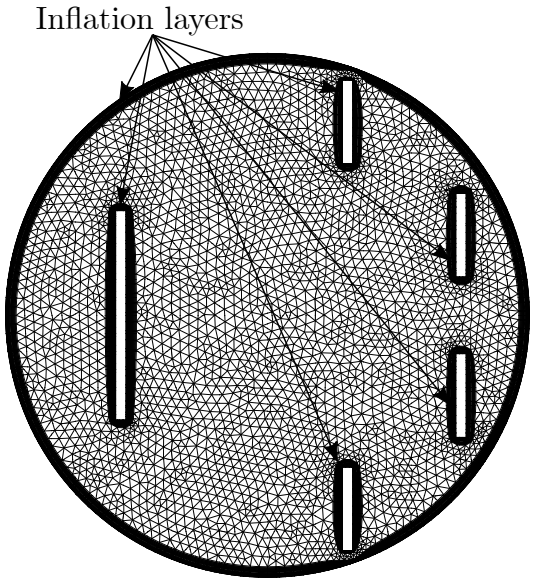

Figure 4.14: Boundary layers on a surface mesh

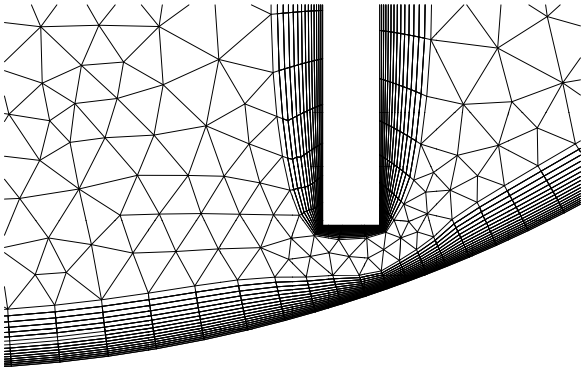

Figure 4.15: Boundary layer compression

4.2.4 Results and discussion

The first design consisted of two twisted tapes and performed satisfactorily. The two twisted tapes removed heat, however, the heat was only removed very close to the tapes which were not situated close to the heated wall, as seen in Fig 4.16a. Thus there still existed a thermal boundary layer which added resistance to heat transfer. The wall temperature contour is shown in Fig 4.16b and shows that the temperature contour is very much undisturbed due to the tapes not being in the vicinity of the heat flux. Since the tapes are at the core/centre of the flow and not close to the wall, it experiences high velocities as seen in Fig 4.21a. This causes a high pressure drop thus leading to a very poor thermal enhancement factor. Furthermore, the hydrodynamic boundary layer close to the heated wall appears to be undisturbed, thus very little turbulence is present leading to low mixing of the heat from the wall to the core i.e. heat is transported poorly.

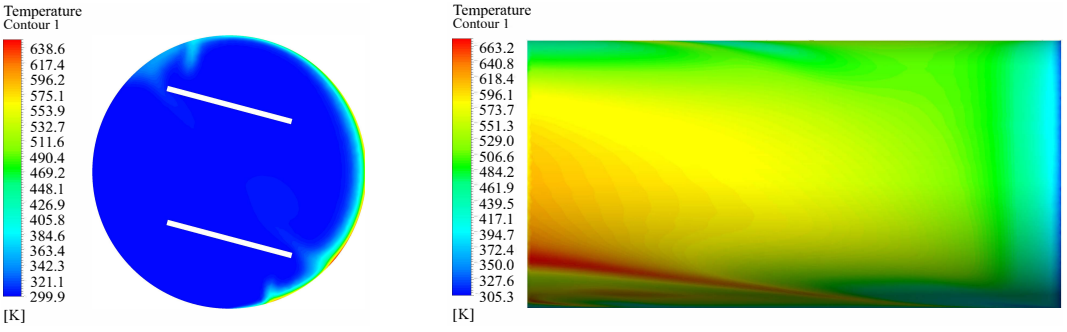

(a) Outlet temperature (b) Wall temperature

Figure 4.16: Two twisted tapes

To ensure a bigger effect of turbulence close to the wall, the second design consisted of three twisted tapes with the two of the twisted tapes being in the region of the applied heat flux. The three twisted tapes performed better than two twisted tapes, interrupting the thermal boundary layer since more tapes are in the vicinity of the heated region as seen in Fig 4.17a. This ensures that the heat is better transported, thereby enhancing the heat transfer lowering the average wall temperature. The contour of the wall temperature is shown in Fig 4.17b and shows that the temperature is disturbed more than that involving two twisted tapes. This is due to there being a greater number of tapes in the vicinity of the applied heat flux. The three twisted tapes are still in the core of the flow, seeing a high velocity and increasing the pressure drop as seen in Fig 4.21b. Nonetheless, the design involving triple twisted tapes performed slightly better than the design involving two twisted tapes.

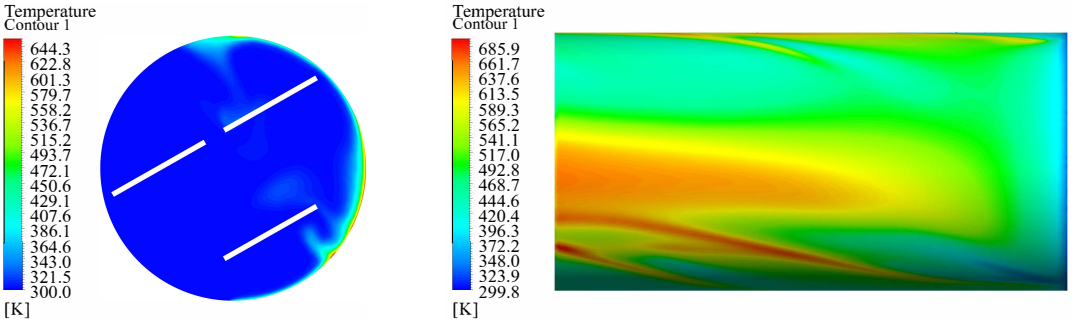

(a) Outlet temperature

(b) Wall temperature

Figure 4.17: Three twisted tapes

To overcome the unnecessary pressure drop from the three twisted tapes, the third design involves four very small tapes situated close to the wall. The four twisted tapes, due to their superior performance, breaks up the thermal boundary layer much better than the previous two designs as seen in Fig 4.18a. This ensures that the heat transfer is enhanced much more effectively. Not only is the thermal boundary layer broken up better, but the wall temperature is better disturbed and thereby lowering the average wall temperature as seen in Fig 4.18b. Since the four twisted tapes are away from the core region of the flow, the velocities experienced is much lower as seen in Fig 4.21c, thereby lowering the friction factor. The hydrodynamic boundary layer is broken up quite effectively in the region of the wall, thereby necessitating better mixing and increasing the turbulence in the region. The design involving four twisted tapes performed much better than the preceding two designs due to its superior heat transfer properties and lower friction factor.

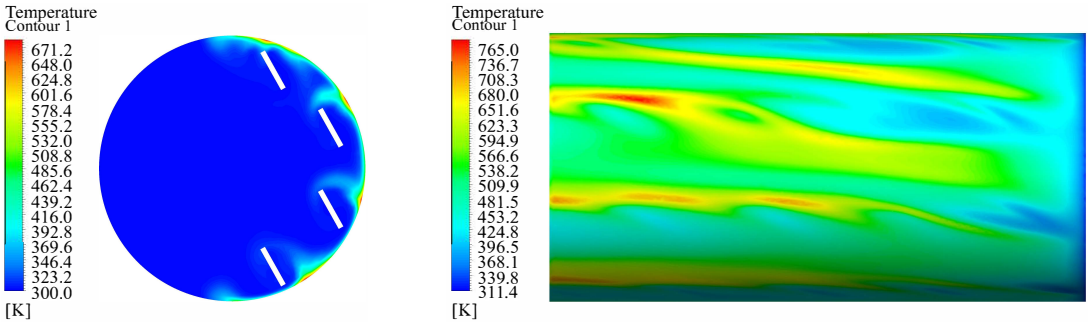

(a) Outlet temperature (b) Wall temperature

Figure 4.18: Four twisted tapes

In an attempt to provide better 'mixing', the fourth design consists of five twisted tapes which is an extension of four twisted tapes as before, with a larger twisted tape added. The design performed rather poorly with the temperature at the wall and outlet behaving very close to that of four twisted tapes (seen in Fig 4.19a and Fig 4.19b). The major downside was the large twisted tape, being in the region of high velocities (see Fig 4.21d) adds to the pressure drop. Thus the design with five twisted tapes performed poorer than four twisted tapes.

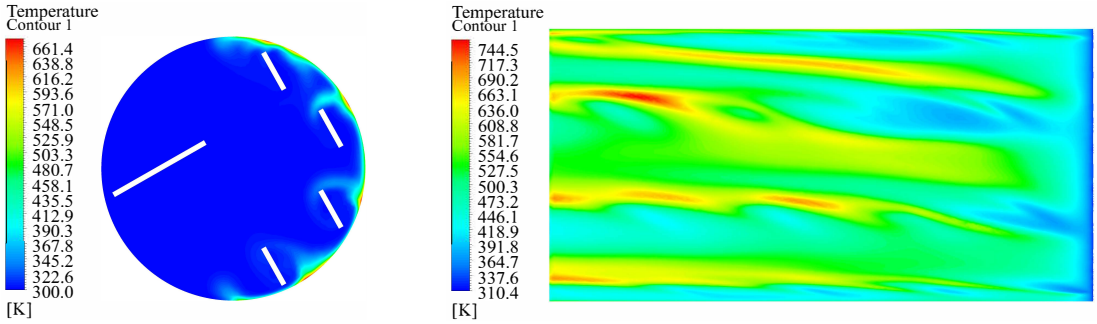

(a) Outlet temperature (b) Wall temperature

Figure 4.19: Five twisted tapes

Since a twisted tape around the core does not affect the heat transfer, the focus is only applied on twisted tapes close to the wall. The fifth and final design (eight twisted tapes) was an extension of the four twisted tapes, however, the tapes were clustered much closer together thereby increasing the turbulence and swirl close to the wall. This affected the hydrodynamic boundary layer quite effectively as seen in Fig 4.21e however due to the added extra surface the pressure drop is higher than four twisted tapes. The heat transfer is superior to that of four twisted tapes, with the thermal boundary layer being broken up much more effectively as seen in Fig 4.20a, hence causing superior mixing. This

leads the average wall temperature to decrease much better than four twisted tapes, and the disturbance of temperature close to the wall leads to a much better temperature contour as seen in Fig 4.20b. Overall, the penalty paid for friction is much higher than the enhancement achieved in heat transfer, causing it to perform poorer than four twisted tapes.

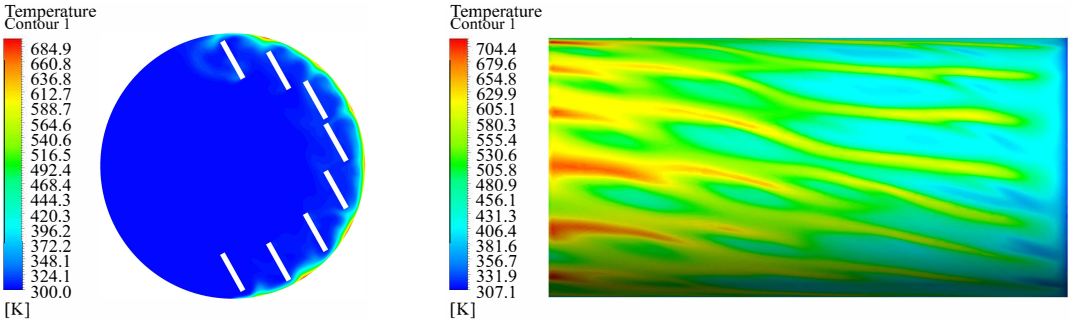

(a) Outlet temperature (b) Wall temperature

Figure 4.20: Eight twisted tapes

The results are summarised in Table 4.3, the designs involving two, three, five and eight twisted tapes performed poorer than the design involving four due to quite a high pressure drop with four twisted tapes performing the best. The high pressure drop is a major contributor to the poor performance which thwarts the success of enhancer. Two important properties were understood in the design involving multiple twisted tapes:

1. A twisted tape at the core of the flow does very little to enhance heat transfer, but rather negatively impacts the pressure drop.

2. Small tapes in close proximity to the wall perform better than larger tapes away from the wall, due to their superior performance in breaking up the thermal and hydrodynamic boundary layers, enhanced mixing and superior swirl properties.

Table 4.3: Multiple twisted tape results

Number of twisted tapes	**Friction factor (f)**	**Nusselt number (Nu)**	**Average wall temperature (K)**	**TEF (η)**
Plain tube	0.032	75.6	554	N/A
Two	0.157	87.2	520.7	0.67
Three	0.187	92.9	507.4	0.68
Four	0.105	92.2	508.8	0.81
Five	0.16	93.2	506.6	0.72
Eight	0.188	95.6	501.1	0.69

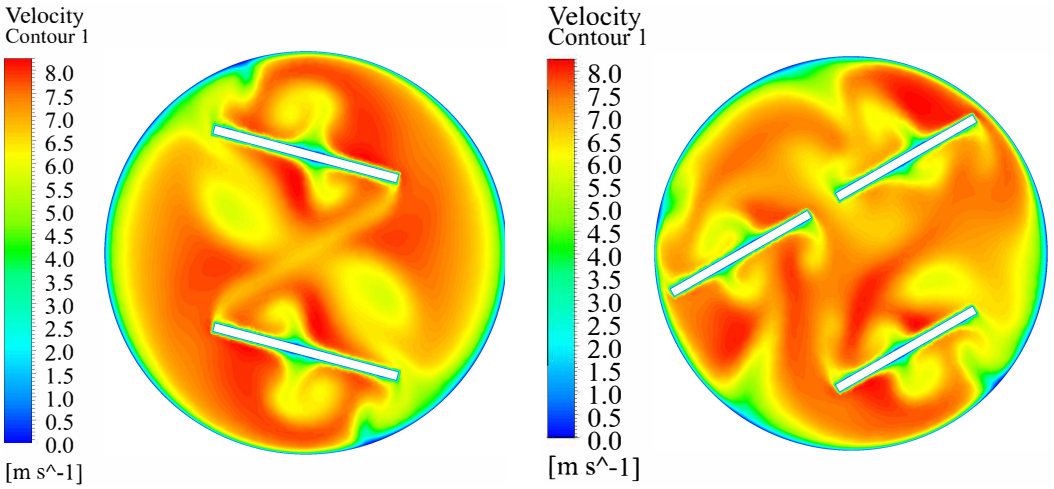

(a) Two twisted tapes

(b) Three twisted tapes

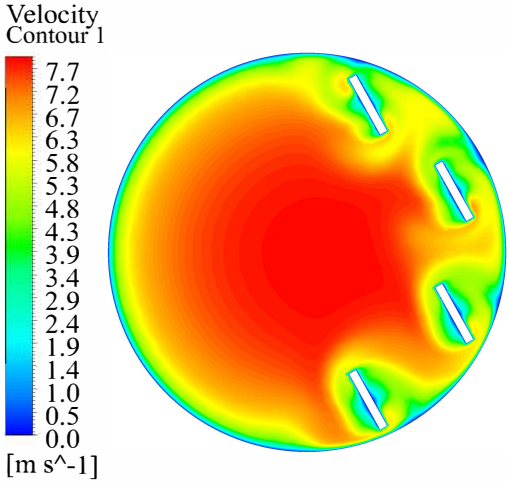

(c) Four twisted tapes

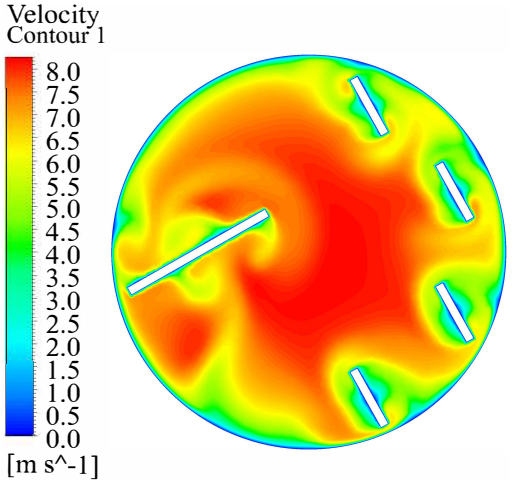

(d) Five twisted tapes

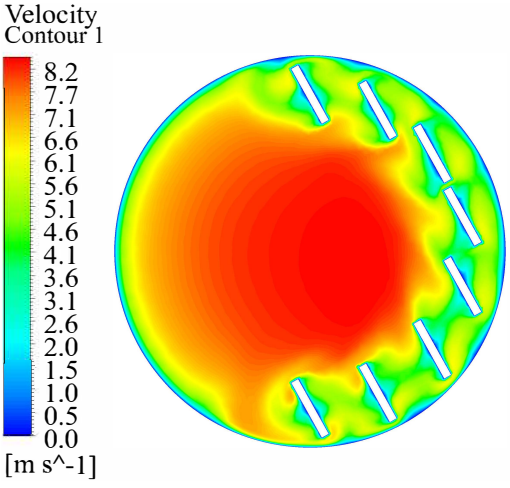

(e) Eight twisted tapes

Figure 4.21: Outlet velocity contours

4.3 Helically twisted tapes

Though multiple twisted tapes are very promising, there exists a major problem. When the number of twisted tapes exceeds two, it becomes increasingly difficult to hold the twisted tapes in place which decreases reliability. One should pursue a design that involves just a single tape. Not only is reliability improved, but it is cost-effective and maintenance and installation becomes relatively easy. This is fulfilled by a variation of twisted tape called the 'Helical Twisted Tape' abbreviated as HTT. A HTT is a thin twisted tape that is wound in coil form and inserted in a tube shown in Fig 4.22.
A HTT is superior to that of ordinary twisted tapes for two reasons. Firstly, the coil shape of the tape causes extra turbulence close to the wall. Secondly, the tape itself causes swirl with the coil. Therefore the HTT offers two forms of turbulence which can be quite advantageous. A HTT is described by a helical pitch P which is the axial distance of one coil revolution and a helical height H as shown in Fig 4.23a. A new parameter called the pitch ratio is defined as helical pitch over the helical height. The tape has a half pitch W and a tape height y as before and seen in Fig 4.23b.

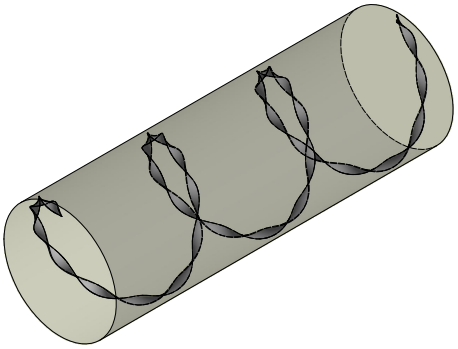

Figure 4.22: Helical twisted tape

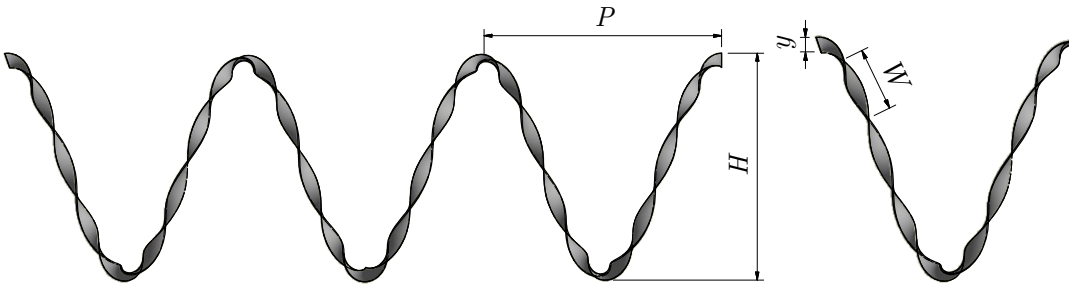

(a) Helical dimensions (b) Twist dimensions

Figure 4.23: Dimensions of HTT

The HTT is inserted in a tube that has a diameter of $D = 0.05$ m and a length of $L = 0.1$ m. The HTT has a helical pitch $P = 0.144$ m and helical height of $H = 0.048$ m corresponding to a clearance of $t = 1$ mm on either side of the tape. This corresponds to a helical pitch ratio $P/H = 3$. Similarly, the twist height is $y = 3$ mm and the twist pitch is $W = 9$ mm corresponding to a twist ratio of 3. The tape has a thickness of $\delta = 1$ mm as before. Everything else such as Reynolds number and the one-sided heat flux is kept the same as before as a basis for comparison against multiple twisted tapes.
A mesh independence study is performed with six different mesh sizes, and the final three meshes are used as a basis for a GCI study. The final three meshes consisted of 3715273, 6264968 and 9622456 cells respectively, corresponding to an average refinement ratio of $r = 1.17$. A GCI of 1.26% and 0.9% was achieved for friction factor and Nusselt number respectively. The meshing strategy for the HTT was similar to multiple twisted tapes as described before and will thus not be described here.
A major downfall of this design is that the coil continuously revolves for 360° which is suitable when there is a uniform heat flux around the tube. However, when a one-sided heat flux is applied, the HTT is in regions where is no heat flux and consequently there is a pressure drop with no heat transfer enhancement in that region leading to a decreased thermal enhancement factor. Therefore a modified version of the HTT is proposed called the *Half-Pitch Helical Twisted Tape* (HPHTT) seen in Fig 4.24a. Similar to the conventional HTT, the HPHTT revolves for 180° and then reverses direction. This ensures that the HPHTT remains in the region of one-sided heat flux as seen in Fig 4.24b.

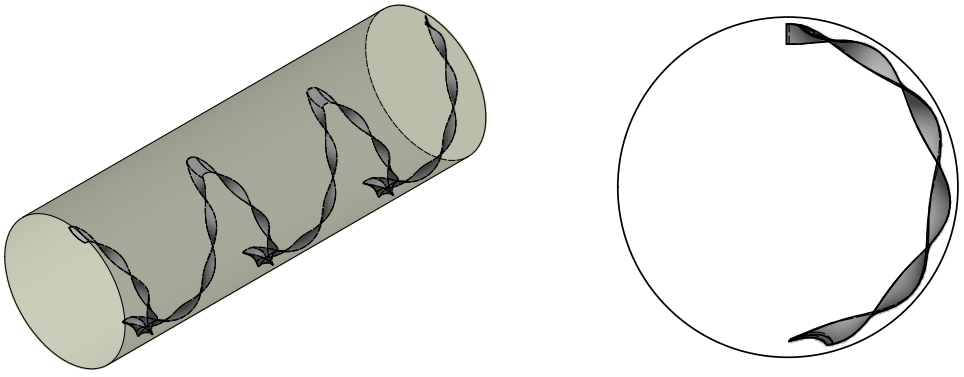

(a) Configuration (b) Front view

Figure 4.24: Half-pitch helical twisted tape

The HPHTT is the same as the HTT in terms of helical and twist ratios and tube geometry. Furthermore, the Reynolds number and heat flux are kept the same as before. Six different mesh sizes are used, with the final three meshes being used as the basis of the GCI study as before. The final three meshes

are composed of 3136665, 5413666 and 9524861 cells which corresponds to an average refinement ratio of $r = 1.2$. A GCI of 0.85% and 0.67% was achieved for friction factor and Nusselt number respectively.

4.3.1 Results and discussion

In general, the HTT performs better than some of the MTT. The temperature and velocity contours of the HTT along the length of the tube are shown in Fig 4.25 and Fig 4.27 respectively. It can be seen that the HTT is quite effective in breaking up the thermal boundary layer. At a length of $L/4$ the thermal boundary layer is not disturbed, however, the thermal boundary layer starts breaking up quite effectively at approximately $L/2$. This implies that separation and reattachment mechanism helps aid heat transfer from vortices formed upstream. At a distance of $3L/4$ the thermal boundary layer is effectively broken up, however, there is a region where there is no interruption in the thermal boundary layer. This is due to the fact that after a revolution of 180° the HTT is not in the region of the heat flux, and the vortices essentially decay and do not affect the boundary layer. This can be seen more prominently at the outlet of the tube where there is quite a large region (approximately an angle spanning 45°) where there is no disturbance in the thermal boundary layer. This is the reason why the wall temperature starts to increase after the tape revolves 180°.
The temperature and velocity contours of the HPHTT are shown in Fig 4.26 and Fig 4.28 respectively. The behaviour of the HPHTT is similar to that of the conventional HTT until the tape revolves 180°. At this point, the HPHTT remains in the region of the heat flux further breaking up the thermal boundary layer unlike the HTT which can be seen in the temperature contours. This ensures that the wall temperature is lower than that of the HTT. The results are tabulated in Table 4.4.

Table 4.4: Helically twisted tape results

	Friction factor (f)	**Nusselt number (Nu)**	**Average wall temperature (K)**	**TEF (η)**
Plain tube	0.032	75.6	554	1
HTT	0.119	91	511.4	0.778
HPHTT	0.125	93	507.1	0.783

The helically twisted tapes perform well in removing the heat from the wall at an acceptable pressure loss. The half-pitch helically twisted tape performs better than the conventional helically twisted tape due to the change in direction and thus causing turbulence in the region of applied flux. The conventional tape has a full twist which means the 'second half of the twist' is not in the region of the applied heat flux, thus not mixing the flow well close to the wall.

Thus the half pitch helically twisted tape outperforms the conventional helically twisted tape.
In the helically twisted tape, some flow leaves the helically twisted tape by the edges forming vortices which mix high momentum fluid into the boundary layer which increases velocity fluctuations and intensity which aids heat transfer. The pressure drop is higher in the half pitch helically twisted tape as compared to the conventional helically twisted tape. This occurs because of the sudden change in direction of the twisted tape which causes the flow to suddenly change direction as compared to following the original path, which causes a slight flow blockage.
The helically twisted tapes do perform similar to the multiple twisted tapes containing four twisted tapes and perform better than all the other multiple twisted tape designs. A major contributor to this is the fact that helically twisted tapes provides two forms of swirl, a swirl from the coil and a swirl close to the wall which is the secondary flow. Furthermore, helically twisted tapes do not offer as much surface area as multiple twisted tapes, thereby offering a lower pressure drop. Overall helically twisted tapes are a better option than multiple twisted tapes and would be the primary choice of heat transfer enhancement in solar thermal receivers.

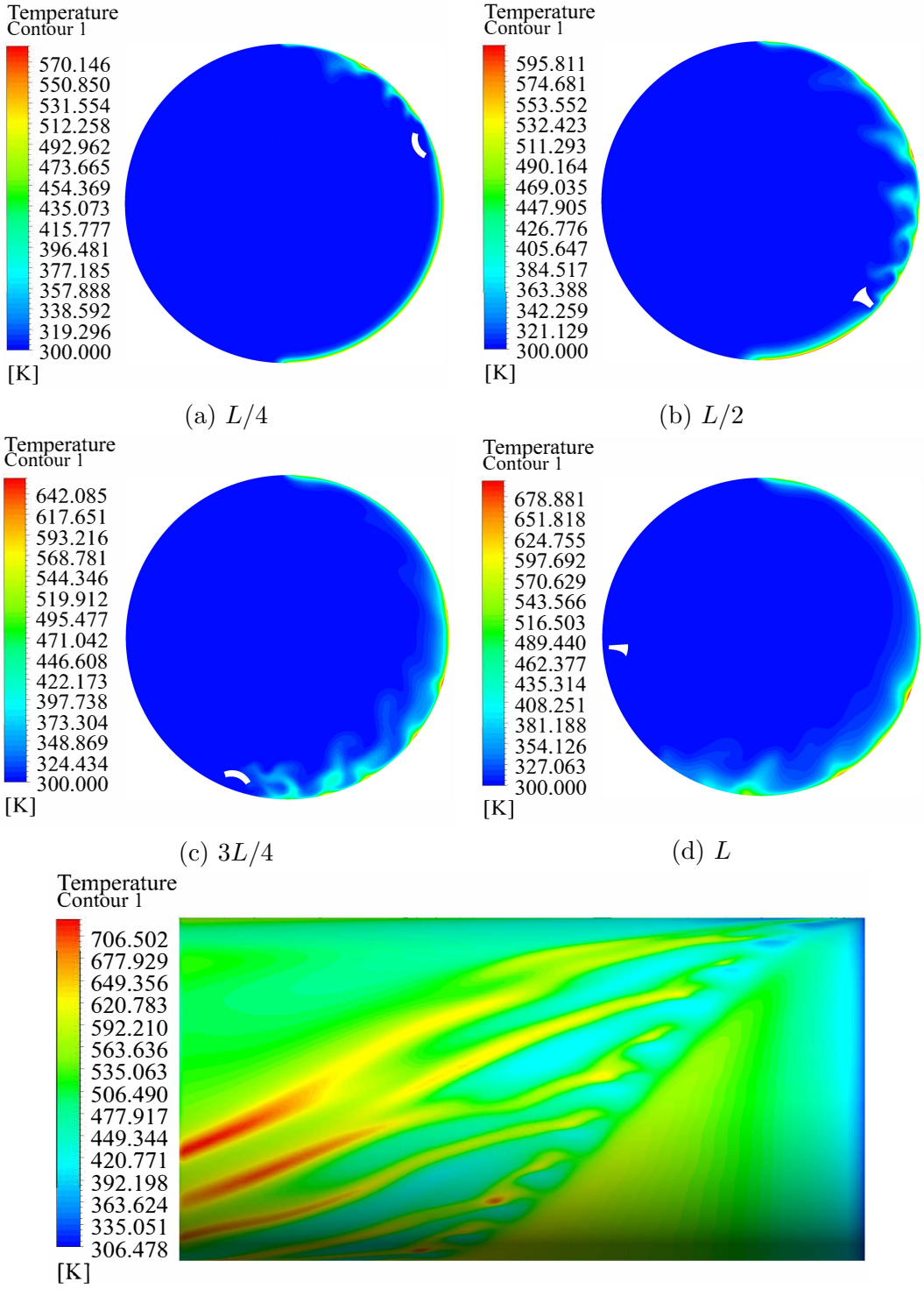

(a) $L/4$ (b) $L/2$

(c) $3L/4$ (d) L

(e) Wall

Figure 4.25: Helically twisted tapes - temperature contours

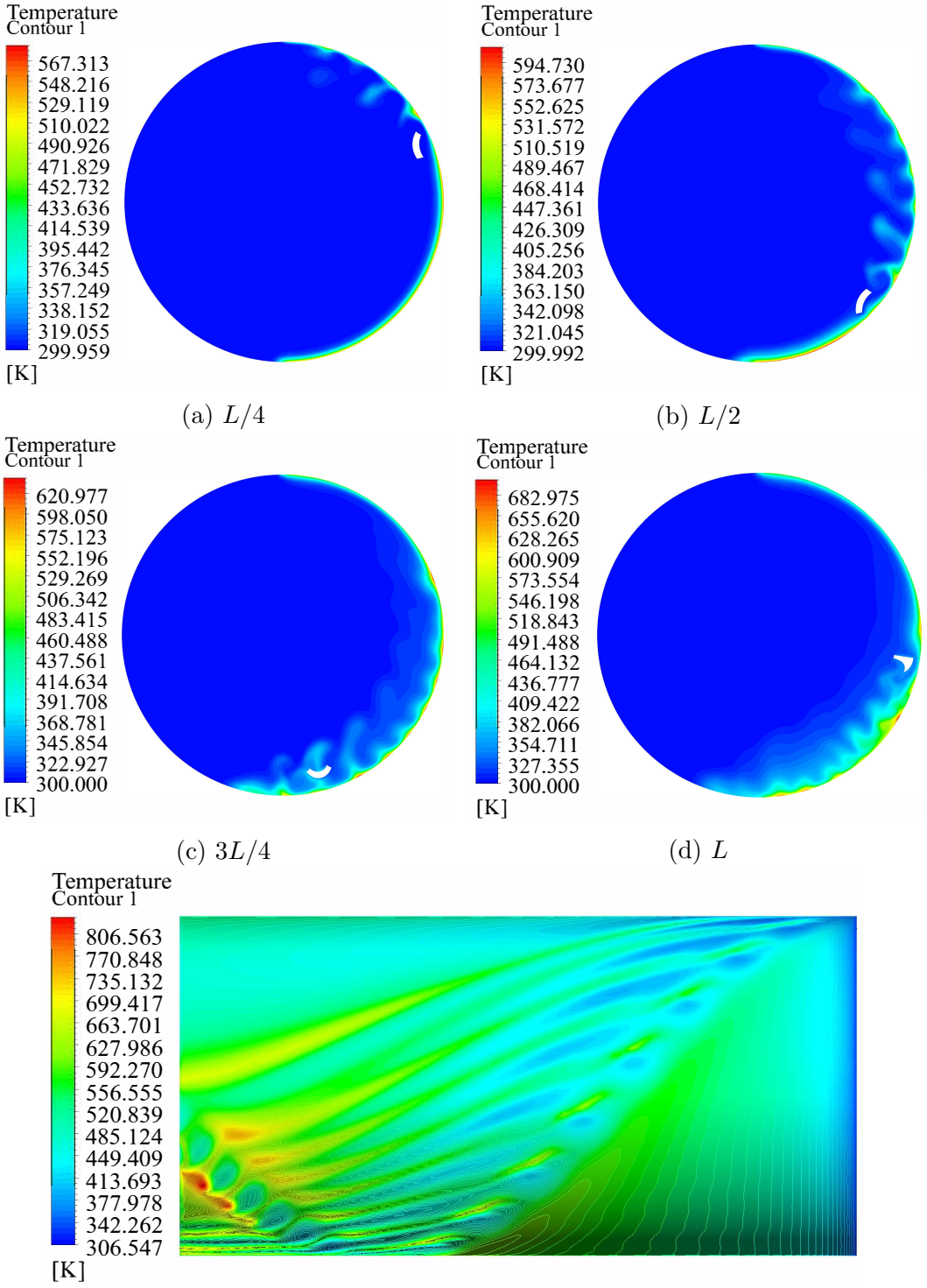

(a) $L/4$ (b) $L/2$

(c) $3L/4$ (d) L

(e) Wall

Figure 4.26: Half-pitch helically twisted tapes - temperature contours

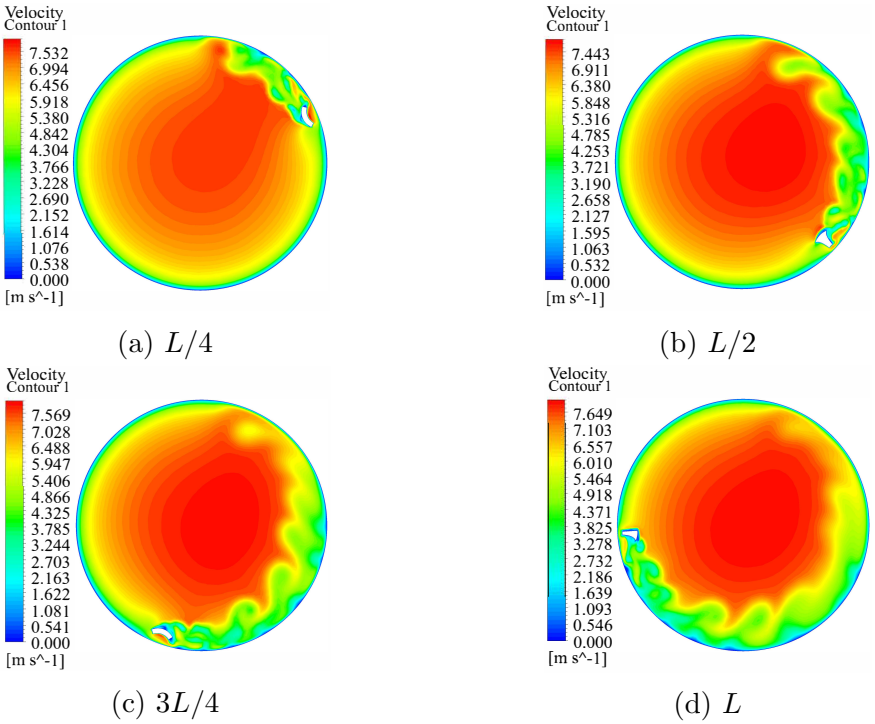

(a) $L/4$ (b) $L/2$

(c) $3L/4$ (d) L

Figure 4.27: Helically twisted tapes - velocity contours

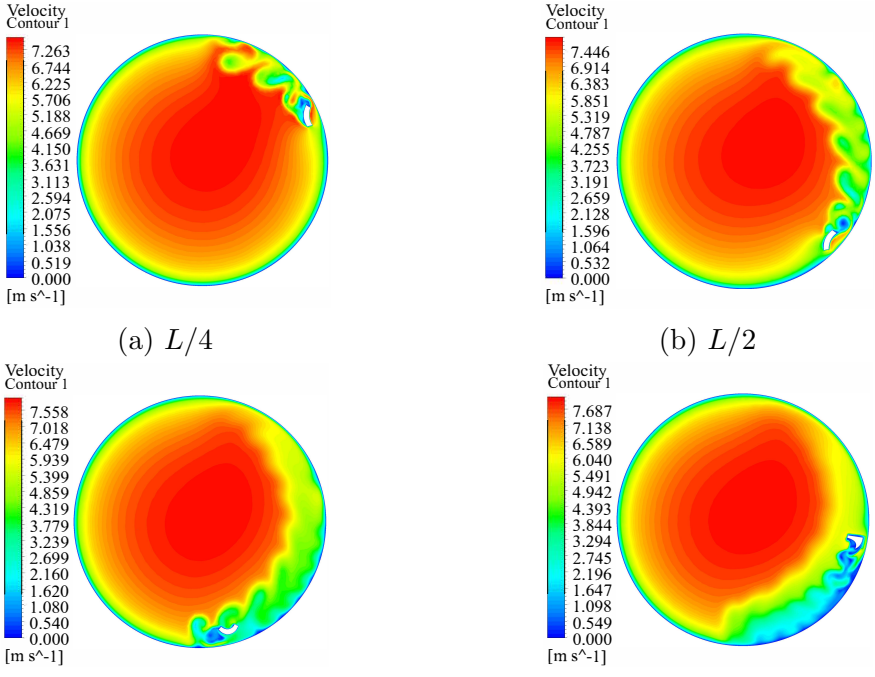

(a) $L/4$ (b) $L/2$

(c) $3L/4$ (d) L

Figure 4.28: Half-pitch helically twisted tapes - velocity contours

4.4 Optimization

This section describes the procedure in optimizing the half-pitch helically twisted tape. The objective is to maximize the heat transfer (or alternatively the heat transfer coefficient/Nusselt number) while minimizing the pressure drop (or friction factor). This would require multiobjective optimization. Alternatively, the thermal enhancement factor can be optimized in which case there is a single objective function. More often than not, there are various constraints that are imposed on a design, due to manufacturing capabilities and cost, and hence this problem becomes a constrained optimization problem.

4.4.1 Optimization procedure

The objective function can be stated as follows:

$$\eta(\mathbf{x}) = f(\mathbf{x}) = f(P, H, W, y, D, \delta) \tag{4.8}$$

where η is the thermal enhancement factor that needs to optimized, which is a function of the design vector $\mathbf{x}$. The design vector $\mathbf{x}$ is a function of six variables as follows.

$$\mathbf{x} = [P, H, W, y, D, \delta]^T \tag{4.9}$$

where P is the helical pitch, H is the helical height, W is the tape pitch, y is the tape height, D is the diameter of the tube and δ is the tape thickness. The optimization problem can then be stated as:

$$\max_{\text{w.r.t } \mathbf{x}} \quad \eta(\mathbf{x}) = \min_{\text{w.r.t } \mathbf{x}} \quad -\eta(\mathbf{x}) \tag{4.10}$$

subject to constraints

$$g_1(\mathbf{x}) = -\frac{P}{H} + 0.75 \leq 0 \tag{4.11}$$
$$g_2(\mathbf{x}) = -\frac{W}{y} + 0.75 \leq 0 \tag{4.12}$$
$$g_3(\mathbf{x}) = -\frac{y}{\delta} + 4 \leq 0 \tag{4.13}$$
$$g_4(\mathbf{x}) = -D + H + 2t \leq 0 \tag{4.14}$$
$$g_5(\mathbf{x}) = -P \leq 0 \tag{4.15}$$
$$g_6(\mathbf{x}) = -H \leq 0 \tag{4.16}$$
$$g_7(\mathbf{x}) = -W \leq 0 \tag{4.17}$$
$$g_8(\mathbf{x}) = -y \leq 0 \tag{4.18}$$
$$g_9(\mathbf{x}) = -D \leq 0 \tag{4.19}$$
$$g_{10}(\mathbf{x}) = -\delta \leq 0 \tag{4.20}$$

for

$$12\,\text{mm} \leq D \leq 60\,\text{mm}$$
$$0.4\,\text{mm} \leq \delta \leq 1.5\,\text{mm}$$
$$t \geq 1\,\text{mm}$$
$$y \geq 3\,\text{mm}$$

Constrains $g_1(\mathbf{x})$ to $g_3(\mathbf{x})$ are applied due to manufacturing constrains. Constraint $g_4(\mathbf{x})$ is to ensure that the model is within bounds while constrains $g_5(\mathbf{x})$ to $g_{10}(\mathbf{x})$ is to ensure no dimensions turn negative. Since all the variables in the design vector are of the same dimension, there is no need to non-dimensionalize the problem.
The constrained optimization problem above can be changed to an unconstrained problem using the penalty function method using a penalty parameter $\mu = 1000$. It is not important to include constraints $g_5(\mathbf{x})$ to $g_{10}(\mathbf{x})$ since the lengths of the different variables cannot be negative under any circumstances. It can be seen that if no constraints are broken, then the entire second term simply vanishes.

$$\begin{aligned} P(\mathbf{x}) = & -\eta(\mathbf{x}) + \mu \left[\max(-P + 0.75H, 0)^2 + \max(-W + 0.75y, 0)^2 \right. \\ & \left. + \max(-y + 4\delta, 0)^2 + \max(-D + H + 2t, 0)^2\right] \end{aligned} \tag{4.21}$$

4.4.2 Optimization algorithm

As stated before, the spherical quadratic steepest descent (SQSD) method is used to optimize the design. Not only is it robust, but it has a self determining step length. Furthermore it performs well for ill-conditioned problems and has a fast convergence rate specifically outperforming the conventional steepest descent method (Snyman and Hay, 2001).
The design vector at iteration $k+1$ can be stated as

$$\mathbf{x^{k+1}} = \mathbf{x^k} - \frac{\nabla f(\mathbf{x^k})}{\mathbf{H^k}}$$

where the Hessian $\mathbf{H^k}$ is replaced with an equivalent curvature of the quadratic function $c^\mathbf{k}$

$$\mathbf{H^k} \simeq c^\mathbf{k} = \frac{2\left[f(\mathbf{x^{k-1}}) - f(\mathbf{x^k}) - \nabla^T f(\mathbf{x^k})(\mathbf{x^{k-1}} - \mathbf{x^k})\right]}{\|\mathbf{x^{k-1}} - \mathbf{x^k}\|^2} \tag{4.22}$$

If the Hessian matrix is used, a total of 13 simulations would be needed for each iteration, whereas if the SQSD method is used a total of 7 simulations since the Hessian involves the calculation of second derivatives while the SQSD method requires only first derivatives.

4.4.3 CFD procedure

The CFD model consisted of a tube of length $L = 100$ mm. A fully developed flow enters the tube. Boundary conditions, fluid properties and turbulence model is kept the same as before. Furthermore, as before it is assumed that the tape itself does not conduct heat. **No attempt is made to conduct a mesh independence study for every simulation** as this is extremely costly. Instead, each simulation was monitored such that the average y^+ value was approximately 0.5 and there was a smooth transition of cells from the wall to the core. Each mesh had approximately 6 000 000 cells which is more than adequate, and hence conservative.

4.4.4 Results and discussion

The process was initialized with the following design vector

$$\mathbf{x}_0 = [P_0, H_0, W_0, y_0, D_0, \delta_0] = [76\,\text{mm}, 38\,\text{mm}, 12\,\text{mm}, 3\,\text{mm}, 40\,\text{mm}, 0.5\,\text{mm}]$$

Since the function values are obtained discretely, the derivative of the function are also obtained discretely, namely in this instance using the forward stepping finite difference method.

$$\left.\frac{\partial P}{\partial x}\right|_x \simeq \frac{P|_{x+\Delta x} - P|_x}{\Delta x} \tag{4.23}$$

The design variable was perturbed by 1% to evaluate local gradients at certain discrete points. To initialize the solution the the curvature is calculated as:

$$c_0 = \frac{\|\nabla P(\mathbf{x}_0)\|}{d} \tag{4.24}$$

where $d = 1$
Close to the optimum the curvature c_k became negative, and this is not allowed per the formulation. If the curvature becomes negative, the algorithm searches for the minimum instead of the maximum in this case. There are two approaches used to counter this problem.

1. In the original formulation, Snyman and Hay (2001) suggested setting $c_k = 10^{-60}$. This would be fine for continuous smooth functions, however for discrete functions this approach does not work close to the optimum and this results in extremely large changes in the design variable.

2. Groenwold *et al.* (2010) proposes the use of convex spherical quadratic approximations whereby $c_k = \max[c_k^*, 0.1]$ where c_k^* is calculated from Equation 4.22. However just as in 1., this also leads to quite large changes in the design variables.

As such, the following approach was used. It should be noted at this point that this is not a verified method and as such, this should be used with caution.

1. If c_k was negative i.e. whilst looking for a minimum, the iteration is close to a maximum, then $c_k = |c_k|$ with $|c_k| < 0.1$, thus taking a bold step away from the maximum.

2. If c_k was small compared to $\nabla P(\mathbf{x})$ i.e. there are no small steps being taken relative to the gradient, then the conservative approach is used as stated in the original formulation of the SQSD algorithm

$$\mathbf{x^{k+1}} = \mathbf{x^k} - d\frac{\nabla P(\mathbf{x^k})}{\|\nabla P(\mathbf{x^k})\|} \tag{4.25}$$

The convergence criteria is set to ensure that the difference between two successive iterations is the following

$$|P_k - P_{k-1}| \leq 1\%$$

The solutions converged within 5 iterations with a difference of 0.7% between the 4^{th} and 5^{th} iterations. Table 4.5 shows the the results of the variable change during the optimization process and Fig 4.29 shows the graphical results of the convergence.

Table 4.5: Convergence of design variables

Iteration	P	H	W	y	D	δ	f	Nu	η
	[mm]	[mm]	[mm]	[mm]	[mm]	[mm]			
0	76	38	12	3	40	0.5	0.12	97.8	0.782
1	89	23	44.5	4	25	1	0.13	98.7	0.819
2	54	54	62.4	3	56	0.4	0.15	91.2	0.652
3	145	58	65	6	60	1.5	0.15	103	0.759
4	340	58	30	3	60	0.4	0.035	82.1	0.984
5	360	58	54	3	60	0.4	0.034	81.5	0.991

It can be seen from Fig 4.29 that the optimization process misbehaves initially and then stabilizes and approaches the maximum. The helical pitch initially increases and then decreases, and finally increasing to its final value. After the 4th iteration, the helical pitch had little to no effect on the results. The diameter hit its upper limit at the third iteration, thereby causing the helical height to also remain constant after the third iteration since it is strictly dependent on the diameter. The tape pitch has no discernible pattern of convergence, while the thickness hits its lower limit at the 4^{th} iteration. The tape thickness has very little influence on the thermal enhancement factor. The tape height

hit its lower limit at the second iteration then returns back to the lower limit at the 4^{th} iteration. The friction factor change has a bigger influence on the thermal enhancement factor than the Nusselt number change. This is in part the reason that the 4^{th} and 5^{th} had a large helical pitch, that contributed to its low friction factor.

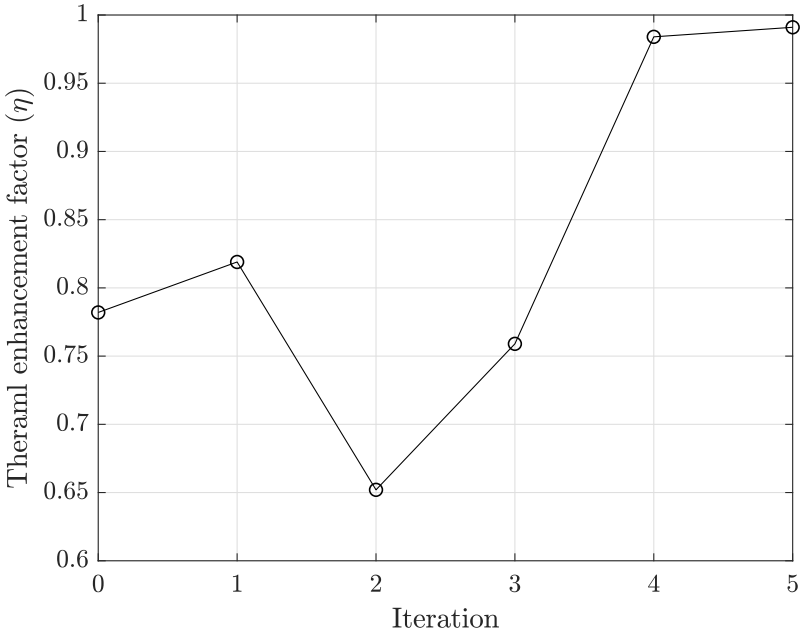

Figure 4.29: Convergence history of the objective function

4.5 Final simulation

This section describes the results of the final optimized design. Various avenues are now considered, which were not considered before, such as multiple Reynolds numbers, temperature dependent properties, higher pressure and temperature fluid and a one-sided varying heat flux. The following assumptions are made for the simulation.

1. Conduction, convective and radiation losses are ignored. This implies that only the *inside* of the tube is simulated i.e. the fluid domain only.

2. No attempt is made to conduct a stress analysis on the tube including determining the tube thickness, as this is outside the scope of this research. The assumption is made that the tube is a *thin walled tube* and by invoking this condition, it is ensured that $q = q_{out} = q_{in}$ i.e. the heat flux is constant throughout the 'thickness' of the tube.

3. Tube roughness is ignored, and it is assumed the tube is perfectly smooth.

4.5.1 Geometry description

The geometry consists of a tube of length $L = 0.7$ m and a diameter $D = 0.06$ m. A HPHTT is inserted in the tube, whose dimensions are described in the optimization section before. The HPHTT has a helical pitch $P = 360$ mm, a helical height $H = 58$ mm, a tape pitch $W = 54$ mm, a tape height $y = 3$ mm and a tape thickness $\delta = 0.4$ mm. The geometry can be created in CAD software such as Autodesk Inventor or CATIA.

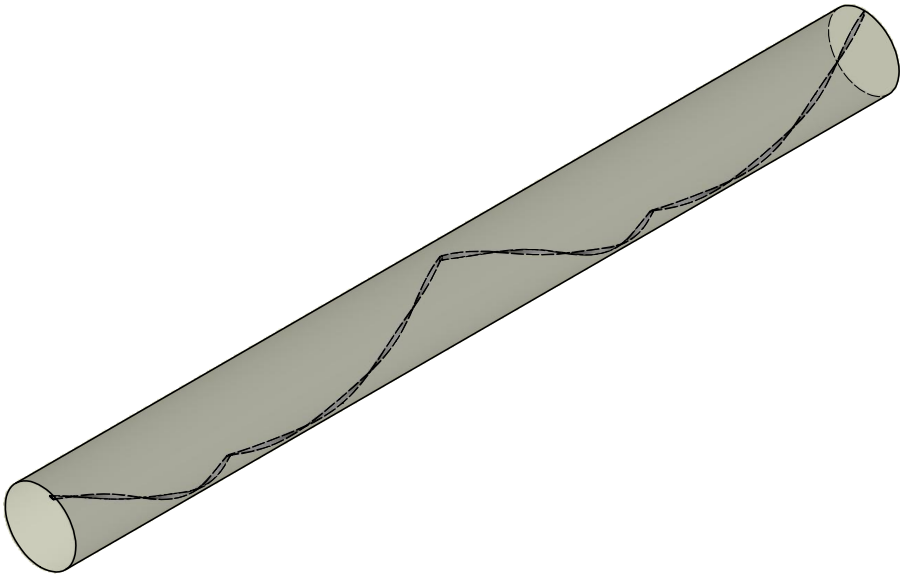

Figure 4.30: HPHTT configuration

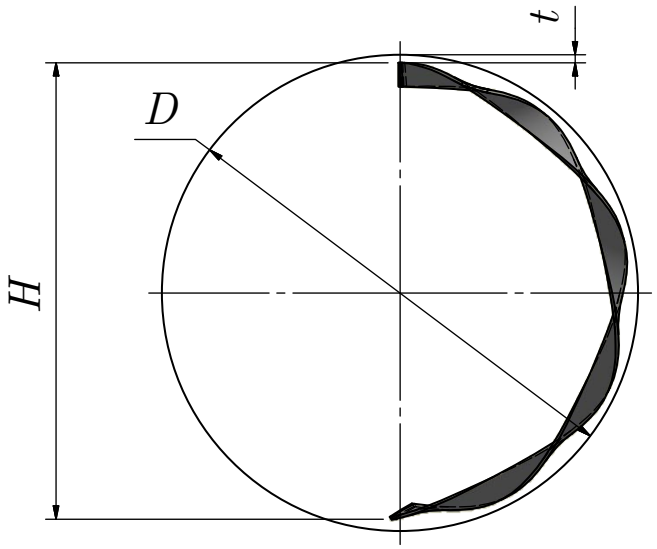

Figure 4.30: HPHTT front view

4.5.2 Meshing strategy

The meshing strategy follows a similar strategy as described in the previous sections. The mesh is composed of an unstructured mesh as seen in Fig 4.31. Inflation layers are applied at the walls of the tube and the HPHTT. Layer compression is the chosen method to avoid collision of inflation layers between the tape and wall of the tube. It can be seen that the mesh gradually grows from the wall to the core. This ensures that the gradients are captured properly and there are no 'sudden shocks' in the gradient.

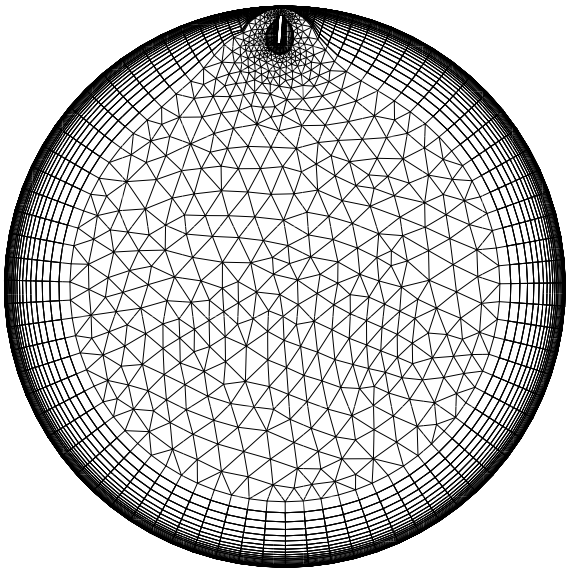

Figure 4.31: Mesh of HPHTT

A close up of the mesh close to the tape is shown in Fig 4.32. There are 6 cells across the gap between the tape and the wall (not including the inflation layers) to ensure the tip effects are captured.

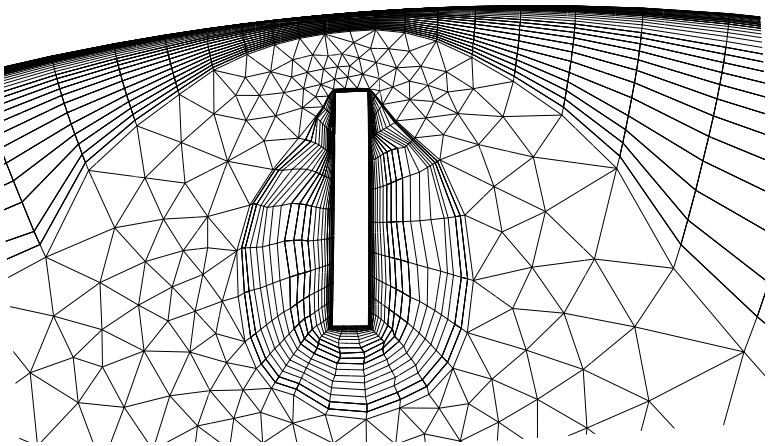

Figure 4.32: Close up of the mesh around the HPHTT

Three mesh sizes are used, the first consisting of 4969288 cells, the second consisting of 8060187 cells and the final mesh consisting of 12480981 cells, which corresponds to an average refinement ratio of $r \simeq 1.17$. Friction factor and Nusselt number are evaluated at Re=10000 and a GCI of 0.05% and 0.04% is achieved for friction factor and Nusselt number respectively. Table 4.6 displays how the y^+ value changes with each mesh refinement. An average y^+ value of 0.5 was aimed for, while the maximum limit was $y^+_{\max} < 4$.

Table 4.6: Progression of y^+ values

	Average y^+ values		
	Heated tube wall	**Non heated tube wall**	**Tape**
Mesh 1	1.15	3.06	1.13
Mesh 2	0.14	0.4	0.35
Mesh 3	0.023	0.03	0.067

4.5.3 Numerical set-up

The simulations are performed on ANSYS Fluent 18.2 with double precision running in parallel, with the aid of a high performance cluster to speed up the simulation. A total of 48 processors were used on two nodes (approximately 250000 cells per processor). If the processors were split among multiple nodes, initialization and convergence did become an issue.

The solver used is a pressure based solver, because the density does not drastically change over the length of the tube and the fluid can be deemed as 'incompressible'. The SST $k-\omega$ turbulence models is used, as described before and the energy equation is enabled, while the simulation is a fully turbulent 3D simulation. As described before, a coupled solver is used for pressure-velocity coupling, and the Green-Gauss node based method is used to discretize the gradient. Second order upwind schemes are used for the remainder of the transport equations. Hybrid initialization is used as a means to get an initial solution. In the case of the processes being split across multiple nodes, the initialization became difficult. As such, V multigrid cycles are used with 3 pre and post sweeps. Other methods such as FMG initialization could have also been used, but using multigrid techniques proved to be adequate. The residuals were set to 1×10^{-7} for continuity, momentum, k and ω while energy was set to 1×10^{-8}. Convergence was reached within 2000 iterations, while various monitors such as pressure and temperature converged within 1400 iterations.

4.5.4 Boundary conditions

Commonly in pressurised air Brayton cycles, a compressor precedes the receiver. Air enters the compressor which has an efficiency of $\eta = 89\%$ at a temperature $T_{\text{in,comp}} = 300\text{K}$ and a pressure of $P_{\text{in,comp}} = 1 \times 10^5$ Pa. The fluid is then compressed to a temperature of $T_{\text{out,comp}} = 614\text{K}$ and a pressure for $P_{\text{out,comp}} = 1 \times 10^6$ Pa (pressure ratio of 10 across the compressor). Thus the temperature at the inlet of the simulation is:

$$T_{\text{inlet}} = 614\text{K}$$

and the operating pressure of the simulation is:

$$P_{\text{operating}} = 1 \times 10^6\,\text{Pa}$$

A developing tube of length $10D$ precedes the heated tube, and the fluid enters at Reynolds numbers of 10000, 15000, 20000, 25000 and 30000. The Reynolds number is based of the tube diameter and *not* the hydraulic diameter. Table 4.7 shows the different velocities and mass flow rates associated with each Reynolds number.

Table 4.7: Flow variables

Reynolds number	**Velocity (m/s)**	**Mass flow rate (kg/s)**
10000	0.92	0.015
15000	1.38	0.022
20000	1.84	0.030
25000	2.30	0.037
30000	2.76	0.044

The applied heat flux is a one sided non uniform heat flux commonly experienced in solar receivers as seen in Fig 4.33. A cosine distribution is chosen as it is the approximate flux profile for a collimated beam hitting a circular tube at right angles from the side. It can be expressed as a cosine function of the maximum heat flux such that when θ is $\pm 90°$, then the heat flux is zero since $\cos\left(\pm\frac{\pi}{2}\right) = 0$, and when θ is $0°$, the heat flux is a maximum since $\cos(0) = 1$. If $\theta \neq \pm 90°$ or $0°$, then the applied heat flux is some fraction of the maximum heat flux. The heat flux can be applied as a user defined function (UDF) in Fluent. Instead of writing the heat flux as a function of θ, it can also be written as a function of the ratio $y/y_{\max}$, where $y_{\max}$ is the radius of the tube. The heat flux can then be expressed as follows

$$q(y) = q_{\max} \cos\left(\frac{\pi y}{2y_{\max}}\right) \tag{4.26}$$

It can be seen that the argument inside the cosine function is equivalent to the angle from the horizontal. The contour of the applied heat flux can be seen in Fig 4.34.

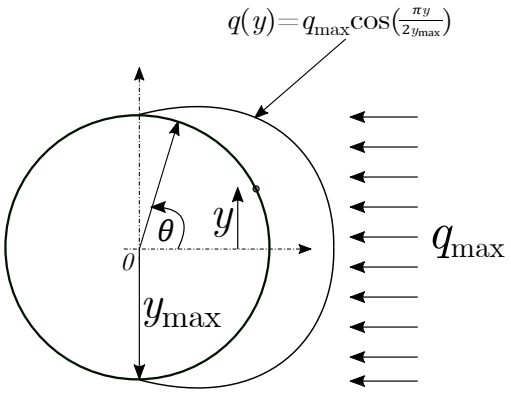

Figure 4.33: One sided non uniform heat flux

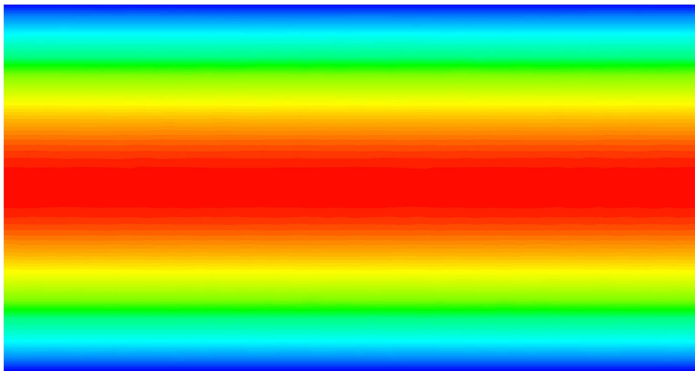

Figure 4.34: Visualization of the applied heat flux

At Stellenbosch University, the solar research roof facilities can accommodate a maximum heat flux of approximately 10 'suns' with approximately 60% efficiency, hence the maximum heat flux a receiver would receive is approximately 6 'suns' or 6000 W/m^2. The UDF heat flux that is used in Fluent can be written as

$$q(y) = 6000 \cos\left(\frac{\pi y}{2(0.03)}\right) \tag{4.27}$$

The C code of the UDF can be seen below. When applying the UDF, it can be interpreted instead of compiled since its relatively small and straightforward. The term '`x[1]`' is the y value that is extracted from the 3D position vector '`real x[ND_ND] = {x[0],x[1],x[2]}`' on a face '`face_t f`'.

```
#include "udf.h"

DEFINE_PROFILE(cos_profile, thread, position)
{
real x[ND_ND];
real y;
face_t f;

begin_f_loop(f, thread)
        {
        F_CENTROID(x, f, thread);
        y = x[1];
        F_PROFILE(f,thread,position) = 6000*cos((3.1415*y)/(2*0.03));
        }
end_f_loop(f, thread)
}
```

4.5.5 Fluid properties

4.5.5.1 Density

The fluid used is air. It is modelled as a compressible ideal gas. Since the range of temperatures that we expect is 300K $\leq T \leq$ 1000K at a pressure of 1 MPa, the coefficient of compressibility is in the range of $0.997 \leq Z \leq 1.003$ indicating the behaviour of the gas does not deviate from the ideal gas behaviour. This can be confirmed by using the principle of corresponding states, which utilizes reduced pressures and temperatures (Çengel and Boles, 2015*b*). At 300K (which is the worst case scenario), the reduced temperature and pressure is 2.26 and 0.26 respectively, indicating the behaviour of air is that of an ideal gas. The governing equation for density can be expressed as:

$$\rho = \frac{P_{\text{operating}} + P_{\text{gauge}}}{\frac{R_u}{M_w}T} \tag{4.28}$$

where $P_{\text{operating}}$ is the operating pressure, P_{gauge} is the gauge pressure, T is the absolute temperature, $R_u = 8.314\,\text{J/mol}\cdot\text{K}$ is the universal gas constant and $M_w = 28.97$ g/mol is the molecular weight for dry air.

4.5.5.2 Specific heat

For specific heat at constant pressure, two polynomials are fitted in the correlations provided by Mueller Jr. and Abu-Mulaweh (2005) and are shown below. In general for an ideal gas, specific heats at constant pressures are functions of mainly temperature and not pressure (Çengel and Boles, 2015*c*). The R^2 variation is 0.99 for 300K $\leq T \leq$ 1000K and 1 for 1000K $\leq T \leq$ 1500K. The units for the polynomials is {J/kg·K}.

$$C_p(T) = \begin{cases} -3.6585 \times 10^{-7}T^3 + 7.9287 \times 10^{-4}T^2 & \\ -3.2874 \times 10^{-1}T + 1041.4788 & \text{for } 300\text{K} \leq T \leq 1000\text{K} \\ \ldots\ldots\ldots\ldots\ldots\ldots\ldots\ldots\ldots\ldots\ldots\ldots & \\ -9.0592 \times 10^{-5}T^2 & \\ +3.65 \times 10^{-1}T + 866.7682 & \text{for } 1000\text{K} \leq T \leq 1500\text{K} \end{cases}$$

4.5.5.3 Thermal conductivity

For the thermal conductivity, a single polynomial is fitted in the correlations provided by Kadoya *et al.* (1985). The thermal conductivity is a function of temperature, and the role of pressure is minimal at pressure above atmospheric pressure (Wu *et al.*, 2009). Nonetheless pressure (1MPa) is still taken into consideration , and the polynomial is shown below. The R^2 variation is 0.99 and the units for the polynomial is {W/m·K}.

$$k(T,P) = \begin{cases} -7.0926 \times 10^{-9}T^2 + 6.7087 \times 10^{-5}T & \\ +0.00791326 & \text{for } 300\text{K} \leq T \leq 1500\text{K} \end{cases}$$

4.5.5.4 Dynamic viscosity

For viscosity, a single polynomial is fitted in the correlations provided by Kadoya *et al.* (1985). Viscosity is a strong function of temperature, with the influence of pressure being negligible, similar to thermal conductivity. Nonetheless pressure (1 MPa) is still taken into consideration and is shown below. The R^2 variation is 0.99 and the units for the polynomial is {Pa·s}.

$$\mu(T,P) = \begin{cases} -7.9857 \times 10^{-12}T^2 + 4.5103 \times 10^{-8}T & \\ +6.4649 \times 10^{-6} & \text{for } 300\text{K} \leq T \leq 1500\text{K} \end{cases}$$

4.5.6 Analysis of results

When dealing with compressible flow, the analysis of the results is more complicated than dealing with incompressible flow. The total pressure drop in a tube with compressible flow can be expressed as:

$$\Delta P_{\text{total}} = \Delta P_{\text{friction}} + \Delta P_{\text{acceleration}} \tag{4.29}$$

The question arises on how to define *incompressible* flow in tubes:

1. Darby (2001) states that incompressible equations can be applied if the density does not change by more than 30%.

2. Crane Co. (1982) states that incompressible equations can be used if the pressure drop is less than 40% of the inlet pressure.

Conditions 1 and 2 were well met when analysing the results obtained from the simulations. It should be noted here that by *incompressible*, it is implied that on a *global* scale the density is nearly *constant*, however there are density fluctuations on a *local* scale. For pipe flow compressibility effects are important when $\text{Re} = \mathcal{O}(10^5)$ i.e. when the Mach number starts exceeding 0.3. With conditions 1 and 2 met, the second term of equation 4.29 is zero. Thus the friction factor can be calculated using bulk/mean properties

$$f = \frac{\Delta P}{\frac{L}{D}\rho_b \frac{v_b^2}{2}} \tag{4.30}$$

where ρ_b is the average density and v_b is the average velocity.
The Nusselt number is calculated just as before

$$\text{Nu} = \frac{hD}{k_b} \tag{4.31}$$

where k_b is the average thermal conductivity. When evaluating the heat transfer coefficient h, the following equation is used

$$h = \frac{q}{T_{\mathbf{wall}} - T_b} \tag{4.32}$$

where q is the heat flux, $T_{\mathbf{wall}}$ is the average wall temperature and T_b is the bulk temperature. A single value for heat flux is obtained by *averaging* out the applied heat flux on the wall. This is a reasonable way to evaluate the heat flux since the relationship between temperature and heat transfer rate is linear. If the heat transfer rate did not have a linear relationship with temperature (such as the heat transfer due to radiation which is of the fourth order), the averaging of the heat flux would perhaps not be an accurate method to use.

4.5.7 Results and discussion

Simulations were performed at four different Reynolds numbers, 10000, 15000, 20000, 25000 and 30000. The summary of the results are tabulated in Table 4.8 and Table 4.9. As the Reynolds number increases, the Nusselt number increases and the friction factor decreases as expected. The reduction of wall temperature also remains nearly constant at approximately $\Delta T_{\text{wall}} \simeq 3$ K. The outlet temperature is similar for both the plain tube and HPHTT, and decreases with increasing Reynolds number. It can also be seen that the thermal enhancement factor remains constant at around $\eta \simeq 0.95$. The results are graphed in Fig 4.35. As the Reynolds number increases the difference between the Nusselt number of the plain tube and HPHTT also increases. Since the thermal enhancement factor is nearly constant, any increase in Reynolds number would make a negligible change in the thermal enhancement factor. Furthermore, as the Reynolds number (and approaches 10^5) the pressure drop would increase exponentially, and would cause a significant decrease in efficiency of the Brayton cycle. An increase in Reynolds number would also see a small change in the outlet temperature since the outlet temperature is reaching its asymptotic convergence. Therefore any increase in Reynolds number beyond this point would practically infeasible.

Table 4.8: Summary of results for the HPHTT

	Plain tube		**HPHTT**		η
Re	**f**	**Nu**	**f**	**Nu**	
10000	0.028	32.42	0.036	33.21	0.942
15000	0.024	44	0.033	45.82	0.944
20000	0.022	54.78	0.031	57.78	0.948
25000	0.021	64.95	0.03	69.27	0.951
30000	0.02	74.67	0.029	79.55	0.956

Table 4.9: Summary of results: temperature

	Outlet temperature (K)		**Wall temperature (K)**		ΔT_{wall}
Re	**Plain tube**	**HPHTT**	**Plain tube**	**HPHTT**	
10000	625.9	625.9	732.1	729.4	2.7
15000	621.9	621.9	700.8	697.5	3.3
20000	619.9	619.9	683.6	680.1	3.5
25000	618.8	618.8	672.6	669.1	3.5
30000	618	618	664.9	661.9	3

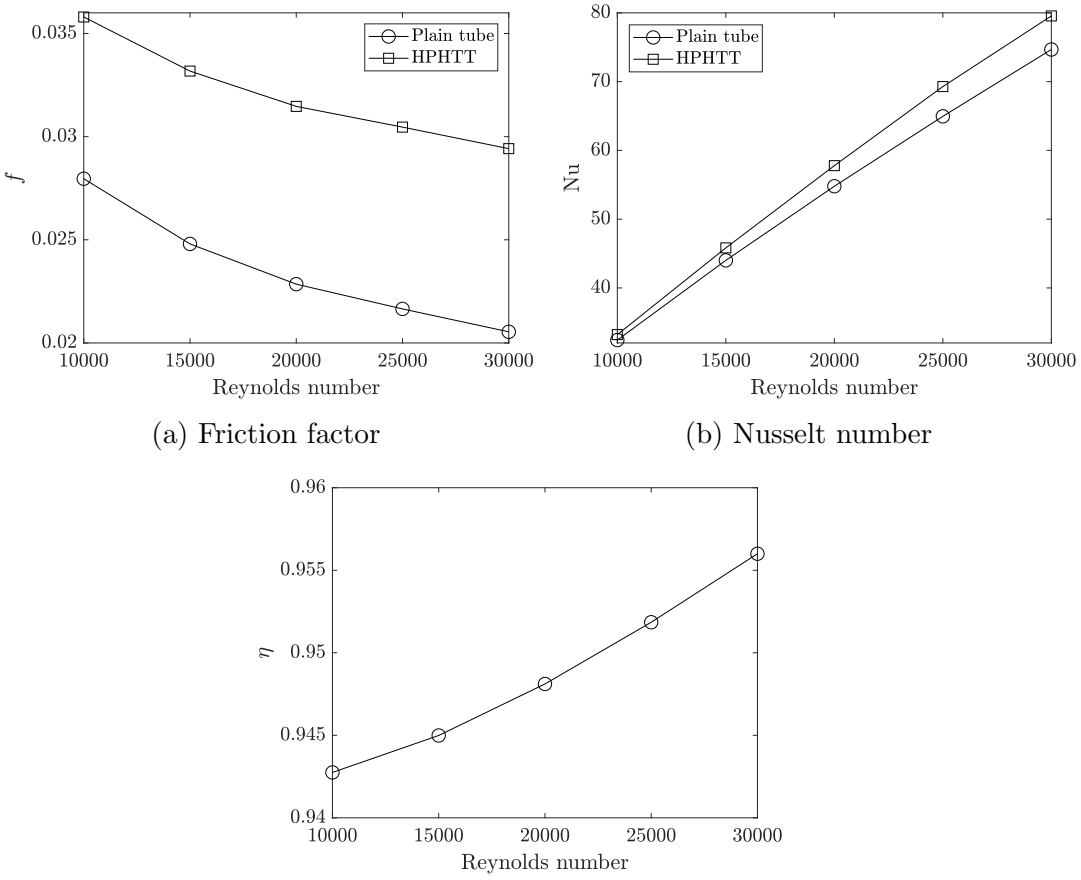

(a) Friction factor

(b) Nusselt number

(c) Thermal enhancement factor

Figure 4.35: Graphical results of the final simulation

Before going into detail about the explanation of the performance of the HPHTT, the temperature and velocity profiles are explained in some detail. Figure 4.36 and Figure 4.37 show the wall temperature and outlet temperature of the HPHTT, while Fig 4.38 shows the outlet velocity. The wall temperature (both average and peak) decrease with increasing Reynolds number. This is because the boundary layer thickness decreases with increasing Reynolds number. Due to an increase in the chaotic nature with increasing Reynolds number, this causes more mixing, resulting in a lower wall temperature. The profile of the wall temperature remains nearly the same regardless of the Reynolds number. This implies that even with increasing Reynolds, there is very little turbulence to alter the flow which is evident in the outlet temperature profile which remains *nearly* unchanged regardless of the Reynolds number. At Re = 10000, the thermal boundary layer is the thickest and decreases as the Reynolds number increases. Hence the outlet temperature is the highest for the lowest Reynolds number. But since the flow is moving slowly, the wall temperature is also the highest for the lowest Reynolds number as the fluid is

not moving fast enough to remove the heat. The velocity contours show that the flow velocity replicates that of a plain tube indicating two things. Firstly, there is very little turbulence close to the wall, and secondly, turbulence is not carried downstream that could aide heat transfer. Vortices with high intensity occurs very close to the tape resulting in a temperature profile change in the region of the tape. Areas where the tape is not present or areas far away from the tape do not receive any enhancement.

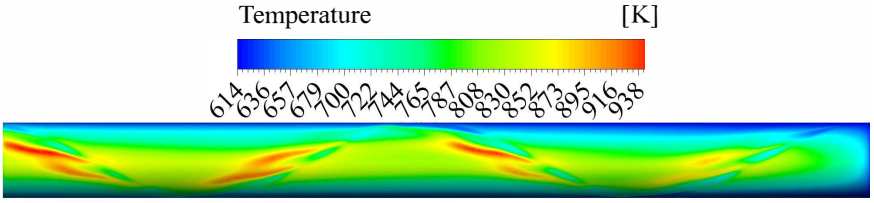

(a) Re = 10000

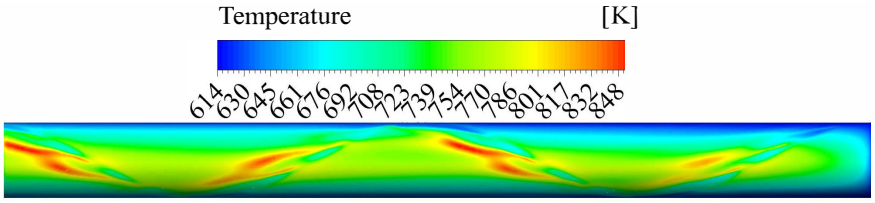

(b) Re = 15000

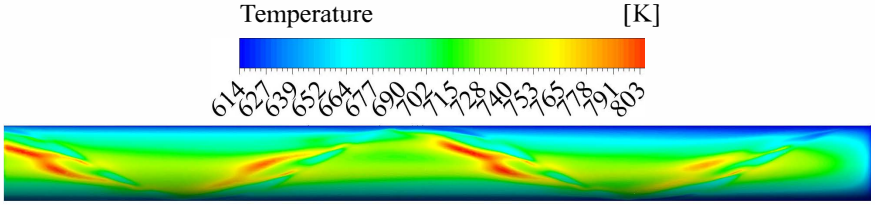

(c) Re = 20000

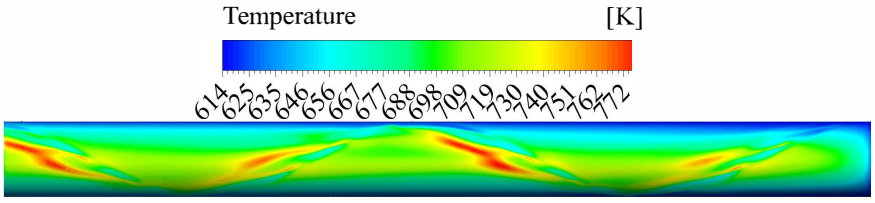

(d) Re = 25000

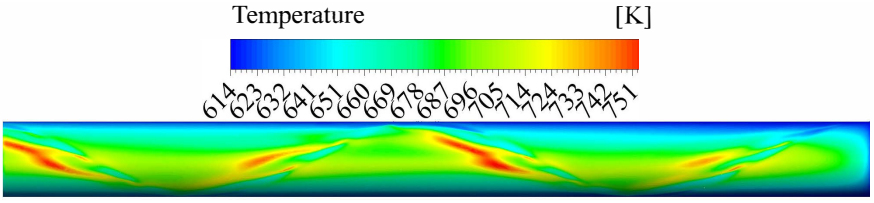

(e) Re = 30000

Figure 4.36: Contours of wall temperature

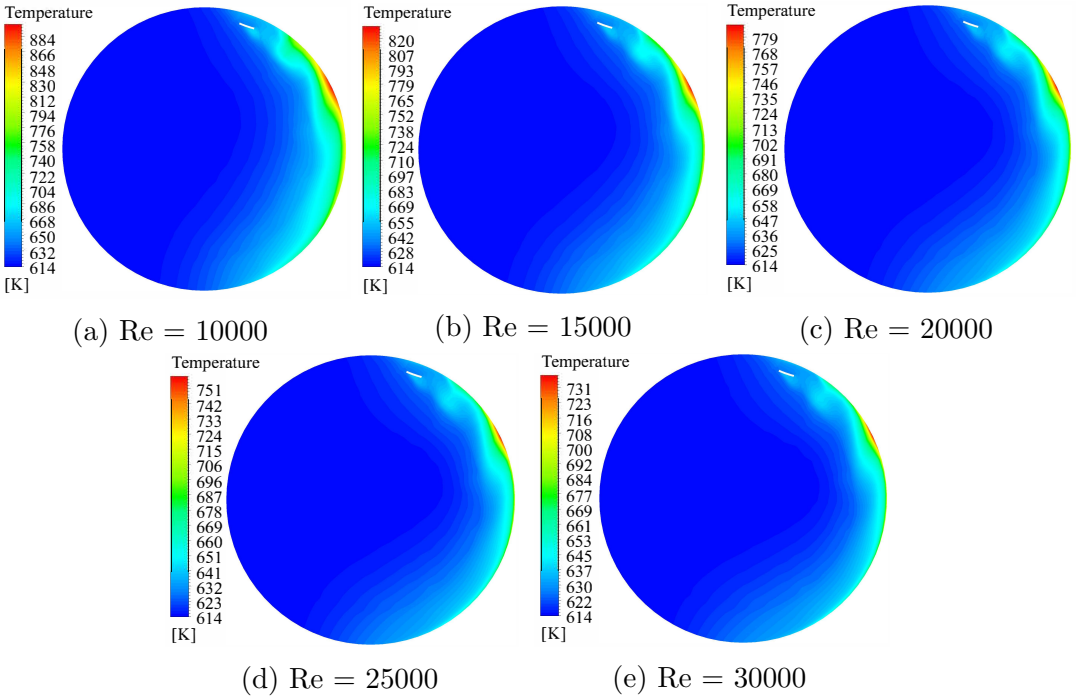

(a) Re = 10000 (b) Re = 15000 (c) Re = 20000

(d) Re = 25000 (e) Re = 30000

Figure 4.37: Contours of outlet temperature

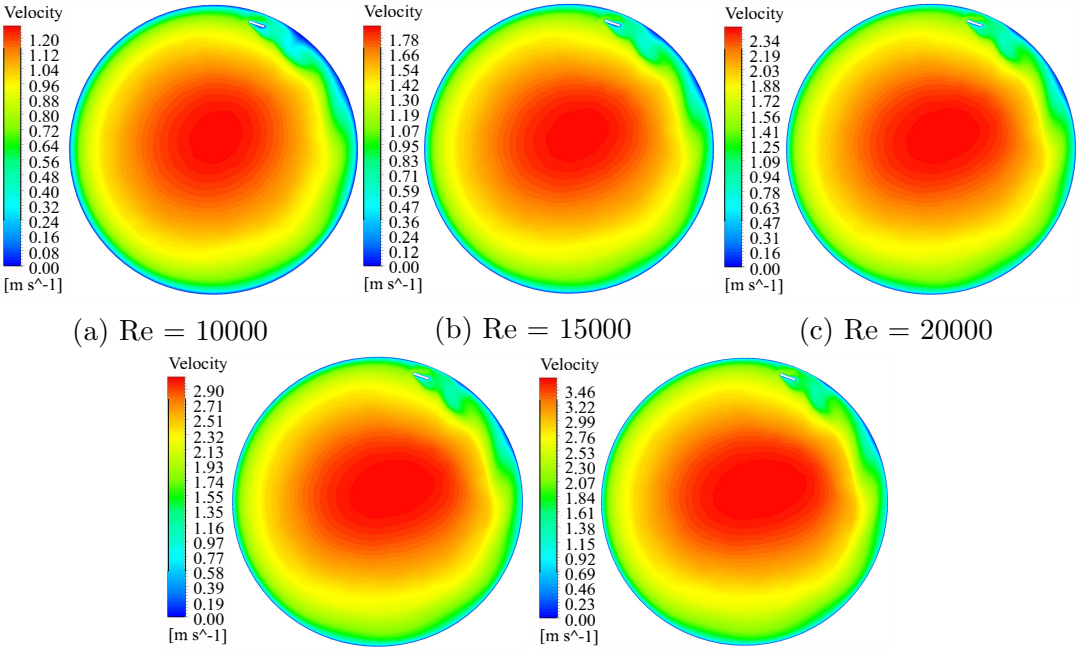

(a) Re = 10000 (b) Re = 15000 (c) Re = 20000

(d) Re = 25000 (e) Re = 30000

Figure 4.38: Contours of outlet velocity

The results obtained show that the HPHTT performed satisfactorily with a very low temperature drop of the wall between the plain tube and the HPHTT. There are two main reasons for this:

1. Optimization
2. Recirculation and reheating

There are six variables of interest in the optimization procedure. They are explained below as to how they affect the flow behaviour.

1. Helical pitch - An increase in the helical pitch causes an increase in the friction factor and Nusselt number. If the pitch is small, then 'coils' are clustered together resulting in higher turbulence and better heat transfer. However, there is also an increase in friction factor due to the larger area that the fluid is in contact with, as well as an increase in flow blockage.

2. Helical height - An increase in the helical height will results in an increase in the friction factor and Nusselt number. The larger the helical height (preferably very close to the wall) the more it affects the thermal boundary layer. However, an increase in the helical height means more surface area that increases the friction factor. As seen in chapter 4.2 with multiple twisted tapes, it is not advantageous to have a tape further away from the wall due to a very thin thermal boundary layer that needs to be interrupted.

3. Twist pitch - An increase in twist pitch pitch leads to an increase in friction factor and Nusselt number. As the twist pitch increase, the intensity and frequency of the swirl pattern increases, resulting in greater break up of the thermal boundary layer. But an increase in twist pitch also implies that an increase in surface area and potential flow blockage that increases friction factor.

4. Twist height - An increase in twist height leads to an increase in friction factor and Nusselt number. As the height increases, the vortices that are created from the tape are larger, and hence turbulence intensity increases due to an increase in the velocity fluctuations which leads to efficient mixing. As before an increase in the height implies a larger surface area leading to a greater pressure drop.

5. Diameter - An increase in the diameter of the tube leads to a decrease in pressure drop and heat transfer coefficient. As the diameter increases, the velocity decreases (assuming Reynolds number stays constant) and since the pressure drop is proportional to the square of the velocity, a decrease in velocity would lead to a decrease in pressure drop. An increase in the diameter also leads to a larger wall temperature leading

to a poorer heat transfer coefficient (assuming the outlet temperature of the fluid did not increase significantly). In the case of a friction factor and Nusselt number, the combined effects of both the flow speed and diameter have to be considered since the Reynolds number is a function of both speed and diameter.

6. Tape thickness - An increase in the tape thickness leads to an increase in friction factor and Nusselt number. However, as explained section 4.4 in optimization, the tape thickness has very little effect on the final results and can be ignored. In a practical sense, the tape thickness is important as a thicker tape implies greater stiffness.

The optimization procedure sought to maximize the thermal enhancement factor. In the turbulent regime, the friction factor is more pronounced than the Nusselt number. Hence the algorithm sought to minimize friction factor more than maximizing Nusselt number since the friction factor was a major reason for the poor thermal enhancement factor in the intermediate iterations. This is why the helical pitch, helical height, tape pitch and diameter increases while the tape height decreases, as these things contribute to a lower friction factor. The results for both friction factor and Nusselt number are very close to that of a plain tube and results in a thermal enhancement factor very close to one.

The second and more important reason for the low wall temperature drop is due to recirculation and reheating. There are regions in the flow where the flow separates and reattaches, however between the separation and reattachment points there exists a recirculation 'bubble'. Though flow separation and reattachment is promoted as a method of heat transfer enhancement, recirculation is an unintended consequence. Firstly, it causes a pressure loss due to flow blockage. Secondly, in the recirculation zone air continues to swirl around (or recirculate). This continues swirling bubble absorbs heat with every circulation, hence creating hot and cold spots as seen in Fig 4.39. Though the cold spots are not of concern, the hot spots pose a threat as they affect material temperature limits.

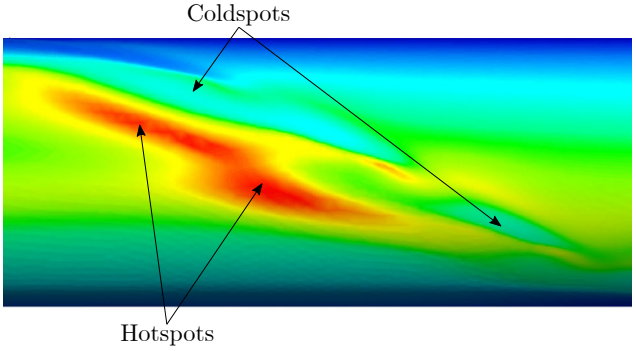

Figure 4.39: Hot and cold spots

Consider Fig 4.40 that shows the cross-section at A-A (located at $x = 0.31$m) and the streamlines at Re = 30000. Two recirculation zones are shown by arrows in the figure. The larger the recirculation zone (bottom of the two recirculation bubbles in this case) the larger the hotspot. There is also a very large recirculation bubble at the bottom of the tube, but since the heat flux at that region is essentially zero, there is no hotspot. Apart from the hotspots, the boundary layer separation and reattachment can also be seen in Fig 4.40b which is the cause for the cold spot. The small recirculation bubble does not cause any hotspots since it is further from the tube wall than the larger recirculation bubble. Furthermore, it is next to the separated boundary layer which is not in contact with the tube wall thus not creating any hot spots.

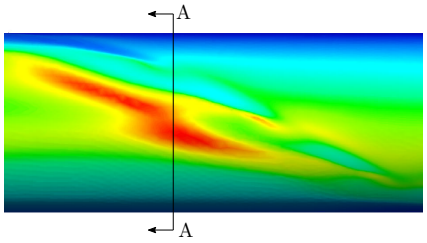

(a) Cross section A-A

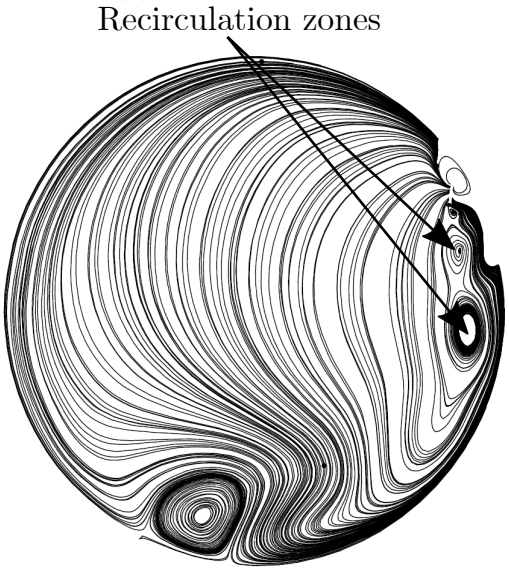

(b) Streamlines at A-A

Figure 4.40: Recirculation zones at cross section A-A

Since it is now known that hotspots effectively increase the average temperature of a wall, the effect of these hotspots are considered at various Reynolds number. Consider two Reynolds number at 10000 and 30000. The hotspot on the wall is shown in Fig 4.41. It can be seen that the effect of the hotspot is

more 'pronounced' at Re = 30000 than at Re = 10000. By 'pronounced' it is meant that the hotspot is larger, darker and more distinct.

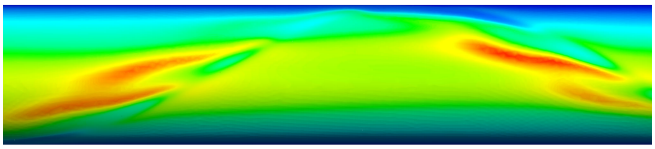

(a) Re = 10000

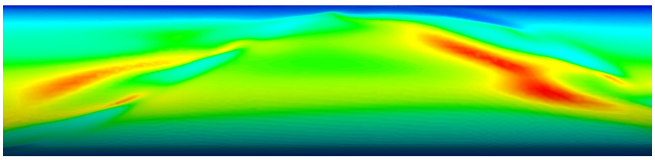

(b) Re = 30000

Figure 4.41: Hotspots at different Reynolds numbers

As stated before, the hotspots are a function of the recirculation zones/bubbles. Consider Fig 4.42 which shows the streamlines of the flow at a length of $x = 0.31$m which is where the first hotspot occurs for all Reynolds numbers. At Re = 10000 the recirculation zone is quite large but has a low recirculation strength. As the Reynolds number increases to 15000, the recirculation zone now comprises of two recirculation bubbles, with the strength of the lower recirculation bubble increasing. As the Reynolds number increases the recirculation bubble continues to gain strength till Re = 30000. The intensity of the recirculation bubble dictates the effect of the hotspot in terms of size. At low Reynolds numbers (10000 and 15000) there is a large recirculation bubble but with low intensity, thus having a less pronounced effect than at higher Reynolds number (20000, 25000 and 30000) which has a much higher strength in its recirculation zone.

In general, the HPHTT performs satisfactorily due to the presence of hotspots which increase the average wall temperature and causes temperature peaks and due to the optimized design which aimed to minimize friction factor since it had more of an effect on the thermal enhancement factor than the Nusselt number. The hotspots can be controlled by increasing the Reynolds number at the expense of pressure drop, or by lowering the heat flux. The former adds to the pumping cost, while the latter increases the material required to construct a receiver.

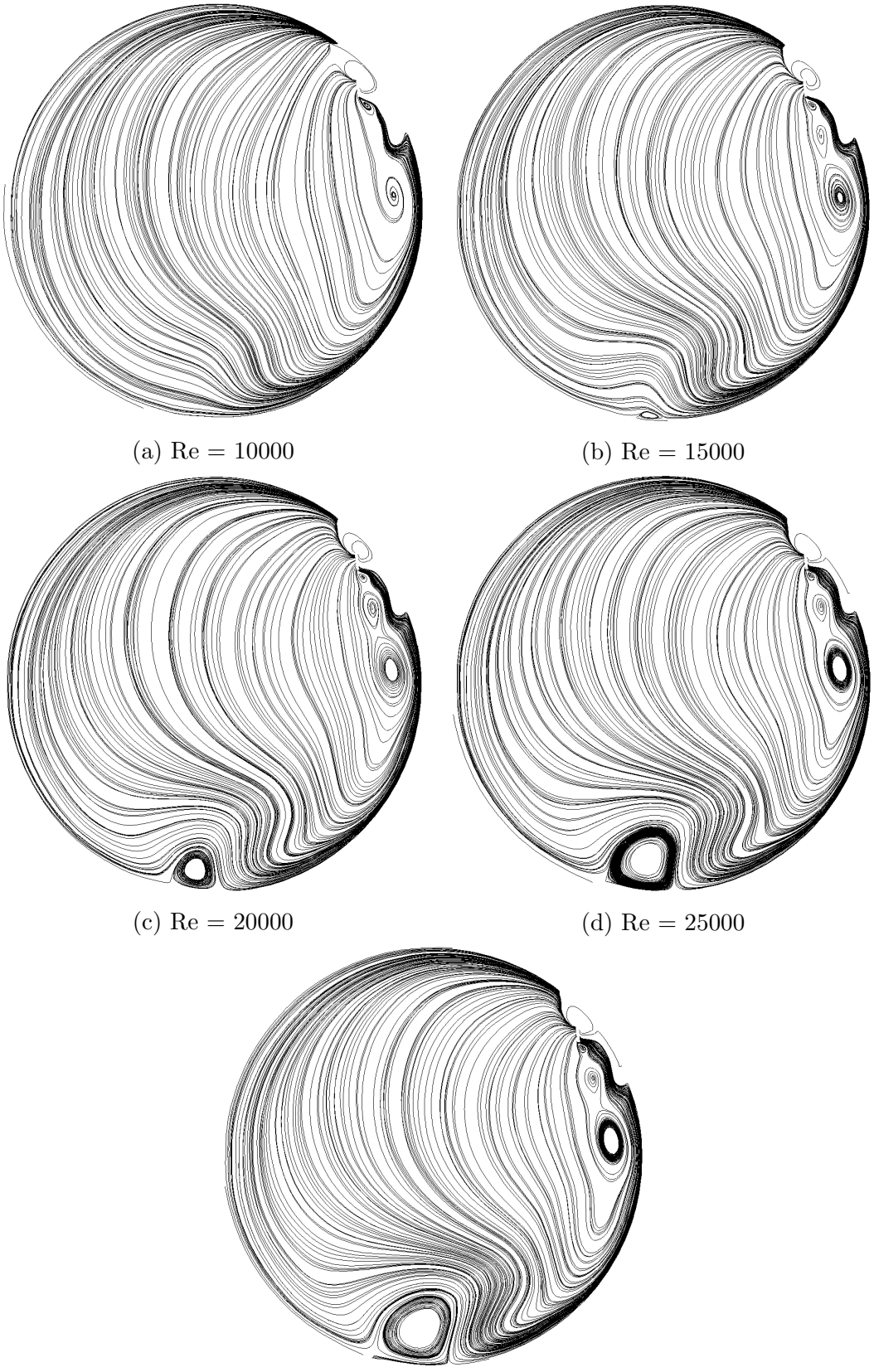

(a) Re = 10000

(b) Re = 15000

(c) Re = 20000

(d) Re = 25000

(e) Re = 30000

Figure 4.42: Recirculation zones at various Reynolds numbers

Chapter 5

Concluding Chapter

5.1 Summary

A classical twisted tape was validated against existing literature and various turbulence models were investigated. This was followed by exploring the avenue of multiple twisted tapes. Due to the satisfactory performance of multiple twisted tapes, helically twisted tapes was investigated. A modified version of the helically twisted tape named the half-pitch helically twisted tape was investigated. Optimization was performed on the half-pitch helical twisted tape and finally, a full thorough simulation was conducted on the optimized design and various Reynolds numbers.

5.2 Conclusion

With the rise in the need for energy on a global scale, CSP technology needs to be optimized to reduce the cost of electricity. CSP plants utilizing air as a heat transfer fluid do not perform well due to the poor heat transfer characteristics of air. This research attempted to devise a method aimed at enhancing the heat transfer in solar receiver tubes while also minimizing the additional pressure loss, thereby increasing the efficiency of the plant.
A classical twisted tape is validated against correlations in literature with various turbulence models. The SST $k-\omega$ turbulence models performs extremely well, due to its ability to predict near-wall effects particularly well as well as being robust in the core of the flow. Due to the high pressure loss in a single twisted tape, multiple twisted tapes are investigated. Five different designs are simulated, with four twisted tapes performing the best of them all. Though it is promising, it was difficult to hold the four twisted tapes in place especially tubes with long lengths. It was determined that having a tape in the core of the flow does not alter heat transfer but simply increases the pressure loss due to a very thin boundary layer. To have the same effect, a helically twisted tape was investigated. It consisted of a simple twisted tape that was wound

in coil form placed close to the wall, thereby breaking up the boundary layer. Since the helically twisted tape makes a full 360° turn, there are regions where there is no heat transfer augmentation but there is a subsequent pressure drop due to a one-sided heat flux. This led to the modification of a helically twisted tape called a *half-pitch helically twisted tape* which is only in the region of the heat flux. The half-pitch helically twisted tape performed well and was optimized using the spherical quadratic steepest descent method. The solution converged within 5 iterations. A final simulation was then conducted at high pressures and temperatures with a one-sided non-uniform heat flux. The reduction in wall temperature was quite low due to recirculation and reheating which caused hotspots, thereby increasing the average wall temperature.

5.3 Recommendation

There were two main reasons for the satisfactory performance of the helically twisted tape as mentioned before, the optimization and the recirculation and reheating. The half-pitch helically twisted tape looks promising, and can be successful with the following recommendations:

- Instead of optimizing the thermal enhancement factor, the reduction in wall temperature can be optimized with a constraint on the pressure drop. This can be done by specifying a limit that the pressure drop cannot exceed. This could decrease the average wall temperature of the enhanced design.
- An investigation can be carried out into the thermohydraulic performance at various helical pitch ratios and twist ratio. If the helical pitch and twist ratio is small i.e. the coils are clustered close together and there are many twists in the tape, it is almost guaranteed that the wall temperature will be reduced. This however, will come with a high pressure drop. This can be minimized by selecting the 'best' combination of helical pitch and twist ratio with an acceptable reduction in wall temperature.
- To counter the effect of recirculation and reheating, the half-pitch helical twisted tape can be further modified by punching small holes along the length, thereby increasing the turbulent kinetic energy and getting a similar effect of 'jet impingement'. It is not guaranteed that this method would work, however, it can be investigated.
- If none of the above methods work, the hotspots can be alleviated by increasing the Reynolds number or by decreasing the heat flux experienced. This should however be the last resort.

5.4 Future work

The half-pitch helically twisted tape looks promising if further research can be conducted. If any of the methods described in the recommendation is successful, a full simulation including taking into account conductive, convective and radiative losses can be simulated. This will help in the research of a finite element analysis to determine the structural integrity of the design in operation. Furthermore, simulations can be conducted at various Reynolds numbers and various heat flux points. This will help in establishing a critical heat flux for various Reynolds numbers.

List of References

Amsbeck, L., Helsch, G., Röger, M. and Uhlig, R. (2009). Development of a Broadband Antireflection Coated Transparent Silica Window for a Solar-Hybrid Driven Microturbine System. In: *Proceedings of SolarPACES 2009*, pp. 1–10.

Arman, B. and Rabas, T. (1992). Influence of Prandtl number and effects of disruption shape on the performance of enhanced tubes with the separation and reattachment mechanism.

Awais, M. and Bhuiyan, A. (2018). Heat transfer enhancement using different types of vortex generators (VGs): A review on experimental and numerical activities. *Thermal Science and Engineering Progress*, vol. 5, pp. 524–545.

Bas, H. and Ozceyhan, V. (2012). Heat transfer enhancement in a tube with twisted tape inserts placed separately from the tube wall. *Experimental Thermal and Fluid Science*, vol. 41, pp. 51 – 58.

Bergles, A.E. (1997). Heat transfer enhancement?the maturing of second-generation heat transfer technology. *Heat Transfer Engineering*, vol. 18, no. 1, pp. 47–55.

Boonloi, A. and Jedsadaratanachai, W. (2016). Turbulent Forced Convection and Heat Transfer Characteristic in a Circular Tube with Modified-Twisted Tapes. *Journal of Thermodynamics*, vol. 2016, pp. 1–16.

Bryan, K. and Shibberu, Y. (2015). Penalty Functions and Constrained Optimization.

Chang, S.W., Jan, Y.J. and Liou, J.S. (2007). Turbulent heat transfer and pressure drop in tube fitted with serrated twisted tape. *International Journal of Thermal Sciences*, vol. 46, no. 5, pp. 506 – 518.

Coetzee, N. (2015 May). *Heat Transfer Coeffecients of Smooth Tubes in the Turbulent Flow Regime*. Master of Engineering, University of Pretoria.

Crane Co. (1982). Flow of Fluids Through Valves, Fittings and Pipe. Technical paper No 410M, Crane Co., New York.

Darby, R. (2001). *Chemical Engineering Fluid Mechanics*, chap. 15, pp. 443–473. 2nd edn. Marcel Dekker AG, Basel.

Eiamsa-ard, S. and Promvonge, P. (2010). Thermal charecteristics in round tube fitted with serrated twisted tape. *Applied Thermal Engineering*, vol. 30, no. 13, pp. 1673–1682.

Eiamsa-ard, S., Thianpong, C., Eiamsa-ard, P. and Promvonge, P. (2010). Thermal characteristics in a heat exchanger tube fitted with dual twisted tape elements in tandem. *International Communications in Heat and Mass Transfer*, vol. 37, no. 1, pp. 39 – 46.

Eiamsa-ard, S., Wongcharee, K. and Sripattanapipat, S. (2009). 3-d numerical simulation of swirling flow and convective heat transfer in a circular tube induced by means of loose-fit twisted tapes. *International Communications in Heat and Mass Transfer*, vol. 36, no. 9, pp. 947 – 955.

Eiamsa-ard, S., Yongsiri, K., Nanan, K. and Thianpong, C. (2012). Heat transfer augmentation by helically twisted tapes as swirl and turbulence promoters. *Chemical Engineering and Processing: Process Intensification*, vol. 60, pp. 42 – 48.

Çengel, Y. and Boles, M. (2015*a*). *Thermodynamics: An Engineering Approach*, chap. 9, pp. 506–512. 8th edn. McGraw-Hill Education, New York.

Çengel, Y. and Boles, M. (2015*b*). *Thermodynamics: An Engineering Approach*, chap. 3, pp. 112–144. 8th edn. McGraw-Hill Education, New York.

Çengel, Y. and Boles, M. (2015*c*). *Thermodynamics: An Engineering Approach*, chap. 7, pp. 330–385. 8th edn. McGraw-Hill Education, New York.

Çengel, Y. and Ghajar, A. (2015*a*). *Heat and Mass Transfer*, chap. 6, pp. 378–407. 5th edn. McGraw-Hill Education, New York.

Çengel, Y. and Ghajar, A. (2015*b*). *Heat and Mass Transfer*, chap. 8, pp. 472–494. 5th edn. McGraw-Hill Education, New York.

Garcia, A., Vicente, P. and Viedma, A. (2005). Experimental study of heat transfer enhancement with wire coil inserts in laminar-transition-turbulent regimes at different prandtl numbers. *International Journal of Heat and Mass Transfer*, vol. 48, no. 21, pp. 4640–4651.

Ghadirijafarbeigloo, S., Zamzamian, A. and Yaghoubi, M. (2014). 3-d Numerical Simulation of Heat Transfer and Turbulent Flow in a Receiver Tube of Solar Parabolic Trough Concentrator with Louvered Twisted-tape Inserts. *Energy Procedia*, vol. 49, pp. 373 – 380.

Groenwold, A., Etman, L. and Wood, D. (2010). Approximated approximations for SAO. *Structural and Multidisciplinary Optimization*, vol. 41, no. 1, pp. 39–56.

Hasanpour, A., Farhadi, M. and Sedighi, K. (2014). A review study on twisted tape inserts on turbulent flow heat exchangers: The overall enhancement ratio criteria. *International Communications in Heat and Mass Transfer*, vol. 55, pp. 53–62.

Kadoya, K., Matsunaga, N. and Nagashima, A. (1985). Viscosity and Thermal Conductivity of Dry Air in the Gaseous Phase. *Journal of Physical and Chemical Reference Data*, vol. 14, no. 4, pp. 947–970.

Kahan, A. (2013 September). EIA projects nearly 50% increase in world energy usage by 2050, led by growth in asia. `https://www.eia.gov/todayinenergy/detail.php?id=41433`.

Kareem, Z., Mohd Jaafar, M., Lazim, T., Abdullah, S. and Abdul Wahid, A. (2015). Heat transfer enhancement in two-start spirally corrugated tube. *Alexandria Engineering Journal*, vol. 54, no. 3, pp. 415–422.

Kretzschmar, H. and Gauché, P. (2012). Hybrid Pressurized Air Cycle for the SUNSPOT Cycle. In: *Southern African Solar Energy Conference*, pp. 1–9.

Lei, Y.G., Zhao, C.H. and Song, C.F. (2012). Enhancement of Turbulent Flow Heat Transfer in a Tube with Modified Twisted Tapes. *Chemical Engineering & Technology*, vol. 35, no. 12, pp. 2133–2139.

Li, P., Liu, Z., Liu, W. and Chen, G. (2015). Numerical study on heat transfer enhancement characteristics of tube inserted with centrally hollow narrow twisted tapes. *International Journal of Heat and Mass Transfer*, vol. 88, pp. 481 – 491.

Lim, K., Hung, Y. and Tan, B. (2017). Performance evaluation of twisted tape insert induced swirl flow in a laminar thermally developing heat exchanger. *Applied Thermal Engineering*, vol. 121, pp. 652–661.

Liu, S. and Sakr, M. (2013). A comprehensive review on passive heat transfer enhancements in pipe exchangers. *Renewable and Sustainable Energy Reviews*, vol. 19, pp. 64–81.

Manglik, R.M. and Bergles, A.E. (1993). Heat Transfer and Pressure Drop Correlations for Twisted-Tape Inserts in Isothermal Tubes: Part II - Transition and Turbulent Flows. *Journal of Heat Transfer*, vol. 115, no. 4, pp. 890–896.

Menter, F. (1994). Two-equation eddy-viscosity turbulence models for engineering applications. *AIAA Journal*, vol. 32, no. 8, pp. 1598–1605.

Mills, A. and Ganesan, V. (2009). *Heat Transfer*, chap. 5, pp. 347–421. 2nd edn. Pearson India Education Services, Noida.

Mueller Jr., D. and Abu-Mulaweh, H. (2005 June). Compression of an Ideal Gas With Temperature Dependent Specific Heat Capacities. In: *2005 Annual Conference*. ASEE Conferences, Portland, Oregon.

Nanan, K., Yongsiri, K., Wongcharee, K., Thianpong, C. and Eiamsa-ard, S. (2013). Heat transfer enhancement by helically twisted tapes inducing co- and counter-swirl flows. *International Communications in Heat and Mass Transfer*, vol. 46, pp. 67 – 73.

Naphon, P. (2006). Heat transfer and pressure drop in the horizontal double pipes with and without twisted tape insert. *International Communications in Heat and Mass Transfer*, vol. 33, no. 2, pp. 166 – 175.

Piriyarungrod, N., Kumar, M., Thianpong, C., Pimsarn, M., Chuwattanakul, V. and Eiamsa-ard, S. (2018). Intensification of thermo-hydraulic performance in heat exchanger tube inserted with multiple twisted-tapes. *Applied Thermal Engineering*, vol. 136, pp. 516 – 530.

Promvonge, P., Pethkool, S., Pimsarn, M. and Thianpong, C. (2012). Heat transfer augmentation in a helical-ribbed tube with double twisted tape inserts. *International Communications in Heat and Mass Transfer*, vol. 39, no. 7, pp. 953 – 959.

Rahimi, M., Shabanian, S.R. and Alsairafi, A.A. (2009). Experimental and CFD studies on heat transfer and friction factor characteristics of a tube equipped with modified twisted tape inserts. *Chemical Engineering and Processing: Process Intensification*, vol. 48, no. 3, pp. 762 – 770.

Roache, P.J. (1994). Perspective: A Method for Uniform Reporting of Grid Refinement Studies. *Journal of Fluids Engineering*, vol. 116, no. 3, pp. 405–413.

Roache, P.J. (1997). Quantification of Uncertainty in Computational Fluid Dynamics. *Annual Review of Fluid Mechanics*, vol. 29, no. 1, pp. 123–160.

Roy, C. (2003). Grid Convergence Error Analysis for Mixed-Order Numerical Schemes. *AIAA Journal*, vol. 41, no. 4, pp. 595–604.

Samruaisin, P., Changcharoen, W., Thianpong, C., Chuwattanakul, V., Pimsarn, M. and Eiamsa-ard, S. (2018). Influence of regularly spaced quadruple twisted tape elements on thermal enhancement characteristics. *Chemical Engineering and Processing - Process Intensification*, vol. 128, pp. 114 – 123.

Saysroy, A. and Eiamsa-ard, S. (2017). Periodically fully-developed heat and fluid flow behaviors in a turbulent tube flow with square-cut twisted tape inserts. *Applied Thermal Engineering*, vol. 112, pp. 895 – 910.

Schobeiri, M. (2010). *Fluid Mechanics for Engineers: A Graduate Textbook*, chap. 11, pp. 357–417. 1st edn. Springer-Verlag Berlin Heidelberg, Heidelberg.

Schwer, L.E. (2008). Is Your Mesh Refined Enough ? Estimating Discretization Error using GCI.

Siddique, M., Khaled, A., Abdulhafiz, N. and Boukhary, A. (2010). Recent Advances in Heat Transfer Enhancement: A Review Report. *International Journal of Chemical Engineering*, vol. 20, pp. 1–28.

Smyth, R. (1974). Heat Transfer in Turbulent Separated Flow. *Journal of Nuclear Science and Technology*, vol. 11, no. 12, pp. 545–553.

Snyman, J. and Hay, A. (2001). The spherical quadratic steepest descent (SQSD) method for unconstrained minimization with no explicit line searches. *Computers and Mathematics with Applications*, vol. 42, no. 1, pp. 169 – 178.

Snyman, J. and Wilke, D. (2018). *Practical Mathematical Optimization*. 2. Springer International Publishing.

Syrakos, A., Varchanis, S., Dimakopoulos, Y., Goulas, A. and Tsamopoulos, J. (2017). On the order of accuracy of the divergence theorem (Green-Gauss) method for calculating the gradient in finite volume methods.

Taslim, M. (2005). Rib fin effects on overall equivalent heat transfer coefficient in a rib-roughened cooling channel. *International Journal of Heat Exchangers*, vol. 6, pp. 25–41.

Versteeg, H. and Malalasekera, W. (2007*a*). *An Introduction to Computational Fluid Dynamics: The Finite Volume Method*, chap. 2, pp. 9–38. 2nd edn. Pearson Education Limited, London.

Versteeg, H. and Malalasekera, W. (2007*b*). *An Introduction to Computational Fluid Dynamics: The Finite Volume Method*, chap. 3, pp. 40–113. 2nd edn. Pearson Education Limited, London.

Versteeg, H. and Malalasekera, W. (2007*c*). *An Introduction to Computational Fluid Dynamics: The Finite Volume Method*, chap. 5, pp. 134–176. 2nd edn. Pearson Education Limited, London.

Ávila Marín, A. (2011). Volumetric Receivers in Solar Thermal Power Plants with Central Receiver System Technology: A Review. *Solar Energy*, vol. 85, no. 5, pp. 891–910.

Wu, H., Grabarnik, S., Emadi, A., de Graaf, G. and Wolffenbuttel, R. (2009). Characterization of thermal cross-talk in a MEMS-based thermopile detector array. *Journal of Micromechanics and Microengineering*, vol. 19, no. 7, pp. 1–7.

Xiao, C., Denner, F. and van Wachem, B.G. (2017). Fully-coupled pressure-based finite-volume framework for the simulation of fluid flows at all speeds in complex geometries. *Journal of Computational Physics*, vol. 346, pp. 91 – 130.

Xuan, Y. and Li, Q. (2000). Heat transfer enhancement of nanofluid. *International Journal of Heat and Fluid Flow*, vol. 21, no. 1, pp. 58–64.

Yongsiri, K., Thianpong, C., Nanan, K. and Eiamsa-ard, S. (2016). Thermal performance enhancement in tubes using helically twisted tape with alternate axis inserts. *Thermophysics and Aeromechanics*, vol. 23, no. 1, pp. 69–81.